Experimental Study of Tailwater Level and Asymmetry Ratio Effects on Three-Dimensional Offset Jets

by

Zacharie Michel Joseph Durand

A thesis submitted to the Faculty of Graduate Studies of
the University of Manitoba
in partial fulfillment of the requirements for the degree of

Master of Science

Department of Civil Engineering
University of Manitoba
Winnipeg, Manitoba, Canada

Abstract

Supercritical fluid jets provide a complex flow pattern and are present in many engineering applications. To date, studies have focused on wall jets, free jets, and two-dimensional offset jets. As a result, our understanding of three-dimensional offset jets is lacking. A deeper understanding of three-dimensional offset jets is important as they are seen in many engineering applications. Understanding the flow patterns of three-dimensional offset jets will aid hydraulic engineers to reduce anthropogenic effects when designing new and rehabilitating older hydraulic structures. The purpose of this study was to evaluate the effects of tailwater level and asymmetry ratio on three-dimensional offset jets.

A physical model was constructed and three sets of experiments were conducted. Each set of experiments evaluated the effects of the Reynolds number, tailwater level, or asymmetry ratio. Velocity measurements were taken with an acoustic Doppler velocimeter. The acoustic Doppler velocimeter measured all three components of

velocity which allowed the calculation of all six components of Reynolds shear stresses and ten components of triple velocity correlation.

The effects of Reynolds number, tailwater level, and asymmetry ratio on streamwise flow development, distributions of mean velocities, and distribution of turbulence statistics were evaluated. Reynolds number effects were found to be insignificant at Reynolds number greater than 53,000. Two different trends were observed in the behavior of three-dimensional offset jets at different tailwater levels. At low tailwater levels the jet will not reattach to the channel bottom as it does at higher tailwater levels. Increasing the asymmetry ratio of an offset jet will make the jet curve towards the channel wall and bottom faster. Once reattached to the wall the velocity decay rate is greatly reduced.

The results found in this study will be useful to a hydraulic engineer designing new or rehabilitating older hydraulic structures which have flow characteristics similar to that of three-dimensional offset jets. The data acquired during this study adds to the available data usable for calibration and validation of turbulence models. All three components of velocity were measured simultaneously which allowed to calculation of the six Reynolds shear stresses and ten triple velocity correlation terms. All velocities and turbulence statistics in this study were measured simultaneously which provides a data set that has rarely been seen before.

Acknowledgements

I would like to thank my co-advisors Dr. Shawn Clark and Dr. Mark Tachie for their support and guidance throughout this project.

Thank you also to the employees of the University of Manitoba and Nortek for their help.

I greatly acknowledge the financial contributions from Manitoba Hydro and the Natural Science and Engineering Research Council of Canada which made this research project possible.

Finally, thank you to my family and friends for supporting and encouraging me through my studies.

Table of Contents

List of Tables

List of Figures

Nomenclature

Symbol	Units	Description
x	[mm]	Streamwise distance from the orifice
y	[mm]	Vertical distance from the channel bottom
z	[mm]	Lateral distance from the channel centerline
Q	[l/s]	Discharge
B	[mm]	Channel width
b	[mm]	Orifice width
b_o	[mm]	Orifice height
b'	[mm]	Lateral location of orifice centerline
h	[mm]	Vertical distance between orifice and channel bottom
y_t	[mm]	Tailwater level

AR	[-]	Asymmetry ratio
U	[m/s]	Streamwise mean velocity
V	[m/s]	Vertical mean velocity
W	[m/s]	Lateral mean velocity
U_b	[m/s]	Bulk velocity at orifice
U_j	[m/s]	Maximum streamwise mean velocity at orifice
U_m	[m/s]	Local maximum streamwise mean velocity
L_e	[mm]	Reattachment length
y_m	[mm]	Vertical location of local maximum streamwise mean velocity
$y_{0.5}^{-}$	[mm]	local jet half width in inner shear layer (vertical plane)
$y_{0.5}^{+}$	[mm]	local jet half width in outer shear layer (vertical plane)
$z_{0.5}^{-}$	[mm]	local jet half width in negative shear layer (horizontal plane)
$z_{0.5}^{+}$	[mm]	local jet half width in positive shear layer (horizontal plane)
m	[-]	Vertical spread rate
x_o	[-]	Virtual origin of vertical spreading
l_1	[-]	Coefficient of lateral vena contracta
l_2	[-]	Coefficient of lateral spreading
x_{vc}	[mm]	Inflection point of lateral spreading

n_l,	[-]	Linear decay rate
n_p,	[-]	Power fit decay rate
U_v	[-]	Virtual velocity of linear decay rate
Re	[-]	Reynolds number
Fr	[-]	Froude number
u_{rms}	[m/s]	Streamwise component of turbulence intensity
v_{rms}	[m/s]	Vertical component of turbulence intensity
w_{rms}	[m/s]	Lateral component of turbulence intensity
k	[m^2/s^2]	Turbulent kinetic energy
uv	[m^2/s^2]	Reynolds shear stress in *xy*-plane
uw	[m^2/s^2]	Reynolds shear stress in *xz*-plane
vw	[m^2/s^2]	Reynolds shear stress in *yz*-plane
uvw	[m^3/s^3]	Triple velocity correlation

CHAPTER 1: INTRODUCTION

1.1 *Motivation and Objectives*

A stream of fluid issuing from an orifice into a larger body of the same fluid presents a complex flow pattern known as a jet. Turbulent jets are present in many engineering applications such as wastewater disposal, modulated mixing, discharge from hydraulic structures, and hydraulic jump stabilization. The energy of a jet discharging from hydraulic structures must be dissipated in order to minimize the anthropogenic effects on aquatic habitat and sediment transport downstream. To date, three-dimensional offset jets are not well understood as studies have focused on two-dimensional jets, and three-dimensional wall and free jets. These jets provide a simpler flow pattern when compared to three-dimensional offset jets.

Current methods of predicting flow characteristics and energy dissipation downstream of hydraulic structures include physical model construction and testing or through the use of commercially available, advanced three-dimensional numerical models. Both of these methods come with disadvantages. Physical models are typically much more expensive

than numerical models, they only provide analysis for one individual design, and it is difficult to accommodate design changes. As for numerical models, they rely on turbulence models that have been developed and validated for particular flow conditions. Current turbulence models cannot be expected to be valid for three-dimensional offset jets as our understanding of their complex flow patterns is incomplete.

Variable such as Reynolds number, orifice shape, expansion ratio, offset height, tailwater level, asymmetry ratio, and surface roughness are thought to have a significant effect on flow characteristics of three-dimensional offset jets. A deeper understanding of three-dimensional offset jets and their complex flow patterns would be beneficial to an engineer when designing a hydraulic structure as well as during the assessment of possible rehabilitation of existing structures. The data acquired during this research will advance the development and validation of turbulence models for use in predicting three-dimensional offset jets.

The objective of this experimental study is to evaluate the effect of two variables on three-dimensional offset jets. The first set of experiments will determine the effects of tailwater level and the second will focus on the effects of asymmetry ratio. Both experiments will quantify the effects on decay and spread rates as well as the distribution of mean velocity and higher order turbulence statistics.

CHAPTER 2: LITERATURE REVIEW

2.1 *Features of an Offset Jet*

A jet is defined as a stream of fluid flowing from an orifice into a larger body of fluid. There exists several types of jets and they are classified by their characteristics. The outlet Reynolds number is used to classify jets as laminar or turbulent. Jets are classified as two-dimensional, or planar, when the expansion ratio $b/B = 1$ and as three-dimensional when the expansion ratio $b/B < 1$. The variables b and B represent the orifice width and channel width, respectively. Jets are also classified as free, offset, or wall jets based on the distance separating the orifice from a solid boundary, denoted by h in Figure 2-1. In a free jet, the distance between the jet and the boundary, h, is large and the boundary has no effect on the jet. In a wall jet, the orifice is adjacent to the boundary, $h = 0$, and the jet remains attached to the boundary. These are the two limiting cases of a jet (Bhuiyan et al. 2011). A jet is classified as an offset jet when it lies between the two limiting cases. As a jet flows from an orifice it will entrain the surrounding fluid. For an offset jet, this will create a low pressure region between the jet and the boundary. The reduced pressure will

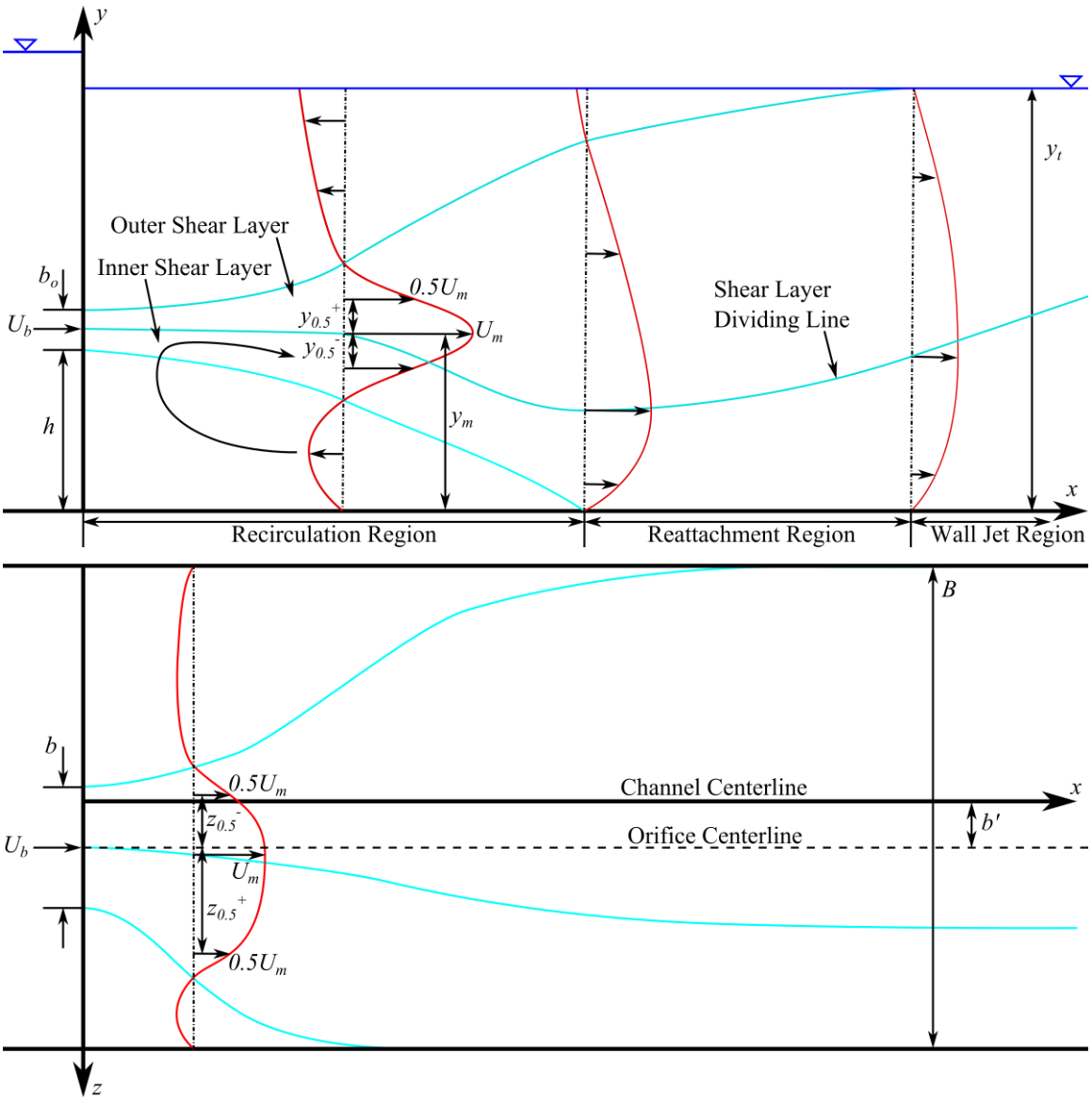

Figure 2-1 Features of an offset jet

cause the jet to curve and reattach itself to the boundary. The curving of a jet towards a solid boundary is known as the Coanda effect.

Figure 2-1 depicts the vertical and horizontal plane of an offset jet. The origin of the coordinate system is centered on the channel bottom with *x*, *y*, and *z*, denoting the streamwise, vertical, and lateral directions, respectively. The symbols U_b and U_m represent the jet bulk velocity at the orifice and the local maximum streamwise mean velocity, respectively. The jet bulk velocity is defined as $U_b = Q/(b \times b_o)$ where Q and b_o

represent the discharge and orifice height, respectively. The vertical location of the local maximum streamwise mean velocity is denoted by y_m and divides the inner and outer shear layers. The inner and outer shear layers outline the regions with a high velocity gradient and positive streamwise velocity below and above y_m, respectively. The symbols $y_{0.5}^-$ and $y_{0.5}^+$ represent the local vertical jet half width in the inner and outer shear layers, respectively. The vertical local jet half width is defined as the vertical distance between the local maximum streamwise mean velocity and the location where $U = 0.5U_m$ within a vertical profile. The symbols $z_{0.5}^-$ and $z_{0.5}^+$ represent the negative and positive local lateral jet half width, respectively, within a lateral profile. The local lateral jet half width is defined as the horizontal distance between the orifice centerline and the location where $U = 0.5U_m$ in a lateral profile. The symbol b' denotes the lateral location of the orifice centerline. The asymmetry ratio, AR, of the channel is defined as $2b'/B$ and the symbol y_t represents the tailwater level. Offset jets are separated in the recirculation, reattachment and wall jet regions as shown in Figure 2-1.

2.2 *Previous Studies*

This section will review previous studies performed on turbulent wall and offset jets. The flow development, decay and spread rates, and turbulence statistics of turbulent wall jets will first be presented as offset jets evolve into wall jets after reattachment. The flow development of offset jets, including the recirculation, reattachment, and wall-jet region will then be reviewed followed by the turbulence statistics.

2.2.1 *Wall Jet*

A wall jet consists of a stream of fluid issuing from an orifice adjacent to a solid boundary. As the stream is constantly attached to the solid boundary two distinct regions

develop, an inner layer and an outer layer. The inner layer is similar to a boundary layer while the outer layer is similar to that of a free jet where there is no boundary interaction. A considerable amount of research has been undertaken to characterize the flow development of wall jets. Experiments characterizing the wall jets performed before 1980 have been reviewed by Launder and Rodi (1981, 1983). A more recent study performed by Eriksson et al. (1998) further increases our understanding of flow development. They found mean velocity and turbulence quantity profiles to be self-similar for a streamwise extent of $40 \leq x/b_o \leq 150$. Further studies found the vertical spread rate to be nearly independent of surface roughness (Tachie et al. 2004), while Ead and Rajaratnam (2004) found the spread rate to increase with roughness. While studying the fully developed zone of fully rough turbulent wall jets Dey et al. (2010) found the streamwise mean velocity profiles to attain similarity when scaled with the jet half width. The turbulence intensity and Reynolds shear stress profiles attained similarity when scaled by the half width of Reynolds shear stress.

Table 2-1 summarizes the most relevant two and three-dimensional wall jet experiments. The Reynolds number is calculated based on the jet bulk velocity, U_b, or the maximum streamwise velocity at the orifice, U_j, and orifice height, b_o. The previous studies utilized many different measurement techniques over a wide range of Reynolds number and a streamwise extent ranging from $0 \leq x/b_o \leq 200$. The decay and spread rates reported throughout the various studies are inconsistent.

Table 2-1 Literature review of wall jets

Author	Technique	Jet type	Reynolds number *Re* [-]	Streamwise extent x/b_o [-]	Decay rate n_p [-]	Spread rate Vertical $dy_{0.5}/dx$ [-]	Spread rate Lateral $dz_{0.5}/dx$ [-]
(Rostamy et al. 2011)	LDA	2D	7,500	20-80	-	0.0791-0.0806	-
(Dey et al. 2010)	ADV	2D	25,500	0-40	-	-	-
(Ahlman et al. 2007)	DNS	2D	2,000	0-40	-	0.068	-
(Wang and Tan 2007)	PIV	2D	10,000	0-30	0.47	-	-
(Ead and Rajaratnam 2004)	Prandtl Tube	2D	76,000-144,000	0-70	0.5	0.076-0.125	-
(Tachie et al. 2004)	LDA	2D	5,900-12,500	0-120	-	0.085-0.090	-
(Eriksson et al. 1998)	LDA	2D	9,600	5-200	1.08	0.078	-
(Nyantekyi-Kwakye et al. 2014 In Press)	PIV	3D	6,000-12,080	0-60	0.996	0.066	0.116
(Agelin-Chaab and Tachie 2011a)	PIV	3D	5,000-20,000	0-120	1.15	0.054	0.255
(Hall and Ewing 2007)	HWA	3D	89,600	3-60	-	0.051	0.281
(Venas et al. 1999)	PHWA	3D	53,000	80	-	-	-
(Abrahamsson et al. 1997)	HWA	3D	53,000-105,000	50-90	1.29	0.065	0.32
(Padmanabham and Gowda 1991a)	PT and HWA	3D	95,400	0-120	1.12-1.16	0.040-0.049	0.22-0.25

LDA: Laser Doppler Anemometer
ADV: Acoustic Doppler Velocimeter
DNS: Direct Numerical Simulation
PIV: Particle Image Velocimetry
HWA: Hot Wire Anemometry
PHWA: Pulsed Hot Wire Anemometry
PT: Pitot Tube

2.2.1.1 Flow Development

Three regions are used to describe the flow development of a wall jet, the potential core region, the developing region, and the self-similar region. The potential core is the region near the orifice where the velocity remains constant to the orifice velocity (Ashforth-Frost and Jambunathan 1996). The developing region extends from the potential core to the start of the self-similar region. The self-similar region is characterized by the collapse of profiles of streamwise mean velocities and turbulence intensities when they are normalized by the appropriate length and velocity scale. Eriksson et al. (1998) and Tachie et al. (2004) found the mean velocity profiles of wall jets to achieve similarity for a streamwise extent of $40 \leq x/b_o \leq 150$ when scaled by the local maximum velocity and the local jet half width. However, the onset of self-similar region may vary depending on initial conditions such as Reynolds number, turbulence level and specific geometry of the nozzle.

2.2.1.2 Decay Rate

The decay rate characterizes the rate at which the local maximum velocity, U_m, reduces with streamwise distance in the self-similar region. In the self-similar region the decay of the local maximum velocity, U_m, follows the power law of the form $U_m \propto x^{-n_p}$, where n_p is the decay rate. As seen in Table 2-1, with the exception of Eriksson et al. (1998), the decay rate, n_p, varies from 0.47-0.50 and 0.996-1.29 for two-dimensional and three-dimensional jets, respectively. The decay rate of three-dimensional wall jets is generally higher than two-dimensional wall jets.

An investigation of Reynolds number and exit geometry effects on decay rate, n_p, was performed by Sun and Ewing (2002). Their results showed that within the self-similar

region, Reynolds number had no significant effect on the decay rate. Agelin-Chaab and Tachie (2011a) studied the effect of three Reynolds numbers, 5,000, 10,000, and 20,000 on decay rate, n_p. Their reported decay rate, n_p, is in good agreement with previous experiments with Reynolds numbers above 70,000 and similar inlet conditions (Padmanabham and Gowda 1991a, Swamy and Bandyopadhyay 1975). They concluded that the decay rate, n_p, within the self-similar region was independent of Reynolds number. Within Reynolds numbers of 5,500 to 13,700, Law and Herlina (2002) found no Reynolds number effects on the decay rate of three-dimensional circular wall jets. A study completed by Rajaratnam and Pani (1974) using several nozzle shapes and Reynolds numbers in the range of 60,700-102,000 attained different decay rates. The differences in decay rates have been mostly attributed to the orifice geometry.

2.2.1.3 Spread Rate

The spread rate, $dy_{0.5}/dx$ and $dz_{0.5}/dx$, is defined as the variation of the jet half width, $y_{0.5}$ and $z_{0.5}$ with streamwise distance, x. By reviewing previous studies, Launder and Rodi (1981, 1983) determined that, within the self-similar region, the vertical spread rates of two and three-dimensional wall jets are linear and follow Equation 2-1 and Equation 2-2, respectively. The lateral spread rate of three-dimensional wall jets follows Equation 2-3.

$$\frac{dy_{0.5}}{dx} = 0.073 \pm 0.002 \qquad \textbf{Equation 2-1}$$

$$\frac{dy_{0.5}}{dx} = 0.048 \pm 0.003 \qquad \textbf{Equation 2-2}$$

$$\frac{dz_{0.5}}{dx} = 0.26 \pm 0.002 \qquad \textbf{Equation 2-3}$$

The vertical spread rate of a three-dimensional wall jet is approximately 2/3 of that of a two-dimensional wall jet. The vertical spreading is reduced because of the simultaneous lateral spreading. From Equation 2-2 and Equation 2-3 spreading in the lateral direction is about 5.4 times higher than the vertical direction which indicates anisotropic spread of the three-dimensional wall jet. The reason for the higher lateral spread rate is not well understood. It has been attributed to the creation of streamwise vorticity, the presence of secondary flow (Launder and Rodi 1983), and the enhanced turbulent diffusion parallel to the wall (Davis and Winarto 1980).

The values of vertical spread rate reported in Table 2-1 vary between 0.068-0.125 for two-dimensional wall jets. The reported spread rates of three-dimensional wall jets are smaller ranging from 0.040-0.066. It appears the spread rate is affected by the initial conditions and Reynolds number, however, it is not affected by surface roughness (Rostamy et al. 2011, Tachie et al. 2004). The lateral spread rates in Table 2-1 range from 0.116-0.32. The initial conditions and Reynolds number were investigated as possible sources of the discrepancies in these results. Padmanabham and Gowda (1991a) showed lateral and vertical spread rates of jets exiting segments of circles to increase by approximately 8% and 12%, respectively, when compared to circular nozzles. Both vertical and lateral spread rates were found to be independent of Reynolds number in the range of 5,500-13,700 (Law and Herlina 2002), and 65,000-108,000 (Sun and Ewing 2002).

2.2.1.4 Turbulence Intensities and Reynolds Stresses

Plots of turbulence intensities, u_{rms}, v_{rms}, and w_{rms}, will show similarity when they are normalized by U_m, and the coordinate y or z are normalized by $y_{0.5}$ and $z_{0.5}$, respectively.

Unlike a single boundary layer that shows a single peak, the turbulence intensity profiles of a wall jet in the symmetry plane will exhibit a double peak, one in the inner and one in the outer shear layer. Peak values of the streamwise turbulence intensity u_{rms} of boundary layers have been reported at 16% while results of two and three-dimensional wall jets from Venas et al. (1999) revealed typical peak values of 20% and 27%, respectively. Self-similarity of turbulence intensity profiles have been observed to begin at a streamwise distance of x/b_o = 60, 40, and 40 for Reynolds number of 5,000, 10,000, and 20,000, respectively, by Agelin-Chaab and Tachie (2011a). Unlike boundary layer flows, the turbulence intensities u_{rms} and v_{rms} are positively correlated which leads to a positive Reynolds shear stress, uv. However, near the boundary the Reynolds shear stress, uv, is negative, which is attributed to the strong interaction between the inner and outer layers (Swamy and Bandyopadhyay 1981, Padmanabham and Gowda 1991b, Abrahamsson et al. 1997).

2.2.2 *Offset Jets*

Relevant studies on offset jets have been listed in Table 2-2. It can be seen that the two-dimensional offset jet has attracted more attention than its three-dimensional counterpart. This section will provide a review of the flow development, decay and spread rate, and turbulence statistics of two and three-dimensional offset jets.

Table 2-2 Literature review of offset jets

Author	Technique	Jet type	Reynolds number Re [-]	Offset height ratio h/b_o [-]	Decay rate n_p [-]	Spread rate Vertical $dy_{0.5}/dx$ [-]	Spread rate Lateral $dz_{0.5}/dx$ [-]
(Bhuiyan et al. 2011)	Prandtl Tube	2D	63,880-272,895	0-4	0.52	0.172	-
(Gao and Ewing 2007)	HWA	2D	44,000	0-1	-	-	-
(Ead and Rajaratnam 2001)	Prandtl Tube	2D	5,000-43,000	5-100	0.5	0.065	-
(Nasr and Lai 1997)	LDA	2D	11,000	2.125	-	-	-
(Nasr and Lai 1998)	LDA	2D	11,000	2.125	-	-	-
(Yoon et al. 1993)	HWA	2D	39,000	2.5-5	0.5	0.076	-
(Pelfrey and Liburdy 1986a)	LDA	2D	15,000	7	-	-	-
(Hoch and Jiji 1981)	HWA, Ptap	2D	1,300-28,000	3-8.7	-	-	-
(Nyantekyi-Kwakye et al. 2014 In Press)	PIV	3D	6,000-12,080	0-8	0.011-0.017*	0.016	0.096-0.114
(Agelin-Chaab and Tachie 2011b)	PIV	3D	5,000-20,000	0-3.5	1.14-1.20	0.054-0.056	0.0245-0.0255
(Davis and Winarto 1980)	HWA	3D	170,000	0-3.5	1.15	0.036-0.046	0.23-0.33
(Nozaki et al. 1979)	HWA	3D	10,000-70,000	0.5-15	-	-	-

LDA: Laser Doppler Anemometer
PIV: Particle Image Velocimetry
HWA: Hot Wire Anemometry
Ptap: Pressure Tap

*Linear decay rate, n_l

2.2.2.1 Recirculation Region

An important feature of an offset jet is the recirculation region. As the jet issues from the orifice it starts to entrain the surrounding fluid creating a low pressure region between the jet and a boundary. This causes the jet to curve and attach itself to the boundary, enclosing the recirculation region. Several techniques such as flow visualization with dye injection, pressure measurements, iso-contours of the mean velocities, and forward-flow fraction technique have been used to measure the reattachment point. Using pressure measurements, the reattachment point is defined as the location of maximum pressure within the jets flow field. The iso-contour technique defines the reattachment point as the location where the zero contour line intersects the solid boundary. In the forward-flow fraction technique the location where the streamwise velocity is positive 50% of the time and negative 50% of the time is defined as the reattachment point.

The reattachment length, L_e, is thought to depend on jet initial condition such as Froude and Reynolds number, and the nozzle shape, aspect ratio and offset height ratio. Dimensional analysis shows the reattachment length, L_e, to be mostly affected by the nozzle offset height ratio and the exit Reynolds number as seen in Equation 2-4. For sufficiently large Reynolds number it was found that viscous effects were negligible (Bourque and Newman 1960). Bhuiyan et al. (2011) confirmed those finding. The reattachment length, L_e, is therefore only a function of offset height ratio as shown in Equation 2-5. For offset height ratios less than 20 Nasr and Lai (1998) have shown the reattachment length of two-dimensional offset jets to follow the power law form seen in Equation 2-6.

$$\frac{L_e}{b_o} = f\left(\frac{h}{b_o}, \frac{U_b b_o}{\nu}\right)$$ **Equation 2-4**

$$\frac{L_e}{b_o} = f\left(\frac{h}{b_o}\right)$$ **Equation 2-5**

$$\frac{L_e}{b_o} = 2.630\ (h/b_o)^{0.855}$$ **Equation 2-6**

Reynolds numbers of 5,000, 10,000, and 20,000 and offset height ratio of 0, 0.5, 1.5, and 3.5 were used by Agelin-Chaab and Tachie (2011b) to study the effect of Reynolds number and offset height ratio on reattachment length of three-dimensional offset jets. Reattachment length was found to be equal to $1.5b_o$, $3.2b_o$, and $6.4b_o$ for offset heights of 0.1, 1.5, and 3.5, respectively. It was concluded that Reynolds number had no significant effect on reattachment length. Comparable reattachment lengths of $4.4b_o$, $6.2b_o$, and $16.3b_o$ for offset heights h/b_o = 2, 4, and 8, respectively, were obtained for three-dimensional offset jets by Nyantekyi-Kwakye et al. (2014 In Press).

The reverse flow within the recirculation region is caused by an adverse pressure gradient. The maximum reverse velocity within the recirculation region of two-dimensional offset jets has been measured at 27% and 37% of orifice maximum exit velocity, U_j, for offset heights of 2.125 and 5, respectively (Nasr and Lai 1998, Yoon et al. 1993). Ead and Rajaratnam (2001) reported contrary results in which the maximum reverse velocity decreases with increasing offset height ratio. For three-dimensional offset jets Agelin-Chaab and Tachie (2011b) reported maximum reverse flow velocities of 0.17%, 0.59%, and 0.38% of maximum exit velocity, U_j, at offset height ratios, h/b_o, of 0.5, 1.5, and 3.5, respectively. Nyantekyi-Kwakye et al. (2014 In Press) measured maximum reverse flow velocities of 5%, 6%, and 4%, of the jet bulk velocity, U_b, at

offset heights ratios, h/b_o, of 2, 4, and 8, respectively. These values are much smaller than what has been reported for two-dimensional offset jets, which is attributed to the higher momentum transport of two-dimensional jets compared to three-dimensional jets. Both two and three-dimensional offset jets experience the highest decay rate within the recirculation region.

2.2.2.2 Reattachment Region

After a jet reattaches to a boundary, it starts to develop into a wall jet. This intermediate region, called the reattachment region, extends from the reattachment point to the streamwise distance where the jet has fully developed into a wall jet. Within this region, the change in local maximum streamwise velocity, U_m, and half width, $y_{0.5}$ and $z_{0.5}$, with streamwise distance, x/b_o, are used to study the development of the flow. A rapid decrease of maximum streamwise velocity, U_m, and increase in jet half width, $y_{0.5}$, is observed in the reattachment region. This characterizes the transition of the flow from an offset jet into a wall jet (Gao and Ewing 2007). Decay rate of maximum streamwise velocity within this region has been observed to be lower than free jets and higher than wall jets (Nasr and Lai 1998, Rajaratnam and Subramanya 1968).

2.2.2.3 Wall Jet Region

Beyond the reattachment region is the wall jet region. In this region the jet has fully developed into a wall jet and the decay of local maximum streamwise velocity is the same as that of a classical wall jet (Rajaratnam and Subramanya 1968). Agelin-Chaab and Tachie (2011b) reported maximum streamwise velocity decay rates of 1.15, 1.16, 1.17, and 1.20 for offset height ratios of 0.0, 0.5, 1.5, and 3.5 indicating that offset height ratio, h/b_o, has a slight effect on decay rate.

Agelin-Chaab and Tachie (2011b) have shown that the use of a mixed scaling will perform better to establish similarity in streamwise velocities, *U*. The streamwise velocities, *U*, should be scaled by the local maximum, U_m, while the vertical distance, *y*, should be centered about the vertical location of maximum velocity, y_m, and scaled by the outer jet half width, $y_{0.5}^{+}$. By using this mixed scaling Agelin-Chaab and Tachie (2011b) observed the streamwise mean velocity profiles to collapse in the outer shear region for streamwise distance of $2 \leq (x\text{-}L_e)/b_o \leq 80$. In the inner shear region the profiles collapsed at streamwise distance $x/b_o \geq 40$ and 60 for offset jets with offset height ratios, h/b_o, of 2 and 4 respectively.

The most detailed studies within the wall jet region of offset jets have been performed by Davis and Winarto (1980) and Agelin-chaab and Tachie (2011b). In the wall jet region, Davis and Winarto (1980) reported vertical spread rates, $dy_{0.5}/dx$, of 0.037, 0.036, 0.039, and 0.046 for offset heights ratios, h/b_o, of 0.0, 0.5, 1.5, and 3.5 respectively. This revealed that the vertical spread rate, $dy_{0.5}/dx$, does not differ significantly from the value of their generic wall jet and is independent of offset height ratios, h/b_o, for offset height ratios, $h/b_o \leq 2$. The vertical spread rate, $dy_{0.5}/dx$, was shown to increase at higher offset height ratios, h/b_o (Davis and Winarto 1980). Agelin-Chaab and Tachie (2011b) reported vertical spread rates, $dy_{0.5}/dx$, of 0.054, 0.054, and 0.056 for offset height ratios, h/b_o, of 0.0, 0.5 and 1.5. The vertical spread rates, $dy_{0.5}/dx$, reported by Agelin-Chaab and Tachie (2011b) are consistent with previously reported values for wall jets while the values reported by Davis and Winarto (1980) are smaller.

Lateral spread rates, $dz_{0.5}/dx$, for offset height ratios of 0.0, 0.5, 1.5, and 3.5 were reported as 0.255, 0.254, 0.25, and 0.245 by Agelin-Chaab and Tachie (2011b) and 0.32, 0.33,

0.29, and 0.23 by Davis and Winarto (1980) respectively. Both studies show a decrease in lateral spread rate, $dz_{0.5}/dx$, with increase offset height ratio, h/b_o, and larger lateral than vertical spread rates. Agelin-Chaab and Tachie (2011b) reported ratios of lateral to vertical spread rates $(dz_{0.5}/dx)/(dy_{0.5}/dx)$ of 4.7, 4.7, and 4.5 for offset heights ratios, h/b_o, of 0.0, 0.5, and 1.5, respectively. These values are comparable to the value of 5.4 that has been reported for generic wall jets (Launder and Rodi 1983).

2.2.2.4 Turbulence Statistics

Only relatively recent studies have reported turbulence statistics of two-dimensional offset jets (Gao and Ewing 2007, 2008, Nasr and Lai 1997, 1998, Pelfrey and Liburdy 1986a, 1986b) and three-dimensional offset jets (Davis and Winarto 1980, Agelin-Chaab and Tachie 2011b). Reported values were limited to a streamwise extent of $x/b_o = 20$ for two-dimensional offset jets while they extended to 80 for three-dimensional offset jets. Davis and Winarto (1980) reported the turbulence intensities and Reynolds shear stresses while Agelin-Chaab and Tachie (2011b) also reported the triple velocity correlations in the streamwise-vertical plane.

Three-dimensional wall jet profiles of the streamwise turbulence intensity, u_{rms}, have been observed to have a double peak at streamwise distance of $(x\text{-}L_e)/b_o = 2$ that disappears by the streamwise distance of $(x\text{-}L_e)/b_o = 6$ (Agelin-Chaab and Tachie 2011b). The double peak of streamwise turbulence intensity, u_{rms}, is not present in three-dimensional offset jets at a streamwise distance range of $2 \leq (x\text{-}L_e)/b_o \leq 80$ (Agelin-Chaab and Tachie 2011b). Profiles of turbulence intensities become self-similar at a streamwise distance of $(x\text{-}L_e)/b_o \geq 40$ and 60 for offset heights of 1.5 and 3.5 (Agelin-Chaab and Tachie 2011b). The turbulence intensity profiles reported by Davis and Winarto (1980)

did not achieve similarity by the streamwise distance of $x/b_o = 32$. The location of maximum turbulence intensity and maximum Reynolds shear stress within the inner shear layer has been reported by Nasr and Lai (1998) to be near the dividing streamline and immediately upstream of the reattachment point. This indicates that the recirculation zone and inner shear layer have a strong interaction near the reattachment point. An offset solid boundary has a significant suppression effect on the turbulence field within the recirculation and reattachment regions as indicated by the streamwise development of the turbulence intensities and Reynolds shear stresses (Nasr and Lai 1997).

The triple velocity correlations are required to calculate the turbulence diffusion term, which is one of the terms in the transport equations that must be modelled. However, the only reported triple velocity correlation terms for three-dimensional offset jets were u^3, v^3, u^2v, uv^2 (Agelin-Chaab and Tachie 2011b). The reported triple velocity correlation terms are predominantly positive except near the boundary where they are mostly negative. The sign change of the triple velocity correlation was observed to occur at a closer vertical location to the wall for three-dimensional wall jets than for two-dimensional wall jets. This was attributed to the outer region having a stronger effect in a three-dimensional wall jet compared to two-dimensional wall jets (Agelin-Chaab and Tachie 2011b). The results obtained by Agelin-Chaab and Tachie (2011b) indicate that the turbulent kinetic energy and Reynolds shear stress are transported from the outer region towards the wall and outer edge of the jet.

2.3 *Summary of Literature*

From the literature review it can be seen that there has been many experimental studies on two-dimensional offset jets. Experimental equipment such as Pitot tubes, hot wire

anemometers (HWA), laser Doppler anemometer (LDA), and particle image velocimeter (PIV) were used to investigate the flow development including streamwise mean velocity decay, vertical and lateral spread rates, and reattachment length. Still, there exist some discrepancies in the results of wall and offset jets. Pertaining to the flow development, there are inconsistencies in the maximum mean velocity decay and both lateral and vertical spread rates. The mechanism involved for the larger lateral spread rate is not well understood. Agelin-Chaab and Tachie (2011b) and Davis and Winarto (1980) performed the most detailed experiments on three-dimensional offset jets. Both provided mean flow, turbulence intensities, and Reynolds shear stress values, however only Agelin-Chaab and Tachie (2011b) provided values for some triple velocity correlation terms.

To date, no study has simultaneously measured the three components of velocity in three-dimensional offset jets. Consequently, all six Reynolds stress terms and all ten triple velocity correlations term have not been reported. The equipment used in this study will allow for a complete analysis of the six Reynolds stress terms and ten triple velocity correlations. The effects of tailwater level and asymmetry have not been thoroughly explored in the past. Further research on their effects may prove these industry relevant variables to be important in three-dimensional offset jets.

CHAPTER 3: EXPERIMENTAL SETTINGS

The Hydraulic Research & Testing Facility at the University of Manitoba housed the experimental equipment used in this research. The experimental facility consisted of a channel with interchangeable nozzles where discharge and water level could be regulated. Velocity was measured with a Vectrino Profiler, an acoustic Doppler velocimeter (ADV) developed by Nortek.

3.1 *Experimental Facility*

The experiments were performed in a rectangular channel 8,000 mm long, 1,500 mm wide, and 950 mm deep. The channel bottom and sides were built out of clear acrylic and painted plywood sheets to minimize acoustic interference. The discharge originated at a constant head tank and was adjusted with a butterfly valve. A wicket gate at the downstream end of the channel was used to control the tailwater level. A schematic of the facility can be seen in Figure 3-1. The upstream wall of the channel was made of 0.5 inch steel plate with cutouts acting as different nozzles. Acrylic blocks were used to obstruct unneeded nozzles and leave only one orifice of the desired dimension and placement. The

upstream wall with cutouts can be seen in Figure 3-2. The nozzles used in this study are classified as sharp nozzles due to the small thickness of the plate compared to the orifice height, b_o.

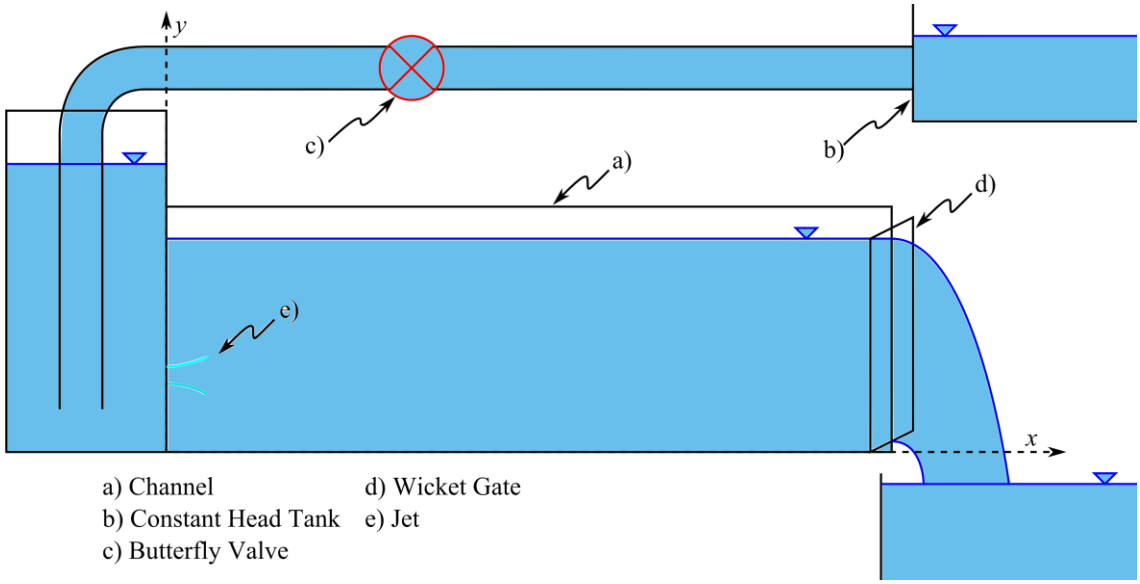

Figure 3-1 Experimental facility

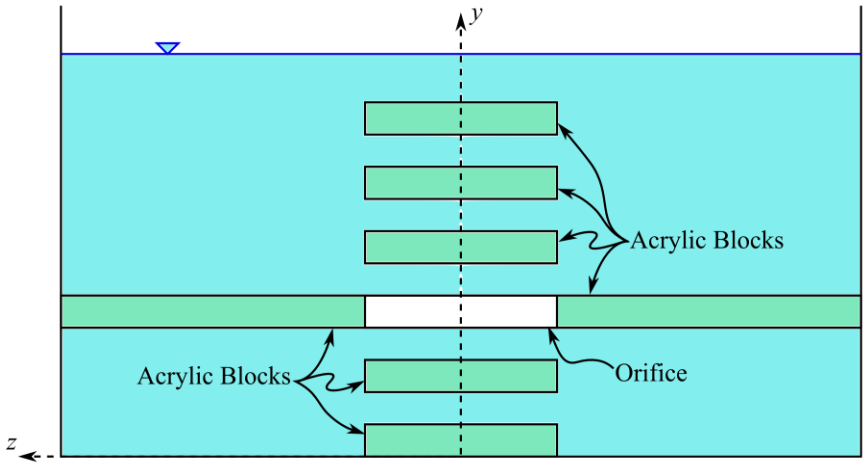

Figure 3-2 Upstream wall

3.2 *Instrumentation*

Velocity measurements were performed with a Vectrino Profiler. The ADV can simultaneously measure the three components of velocities, *U*, *V*, and *W*. Velocities in the range of ±3 m/s can be measured at a sampling frequency of 100 Hz and spatial

resolution of 1 mm. A total of 21 cells arranged in a vertical profile, as seen in Figure 3-3, were sampled simultaneously. The cells distance to the probe head ranged from 40 to 60 mm. Since the probe head needs to be submerged it was not possible to sample points within approximately 50 mm of the water surface. Additional information on the ADV such as an overview of the principles of operation, data quality, and an analysis of sample duration and measurement uncertainty are presented in Appendix A.

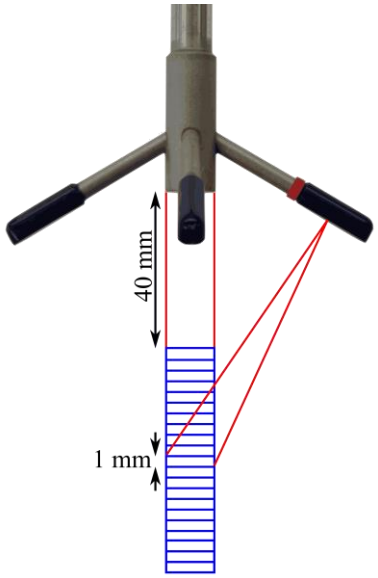

Figure 3-3 ADV probe head and cell profile

The ADV was evaluated to have a total uncertainty of ±3%, ±3%, and ±5% of the local maximum streamwise mean velocity for the streamwise, vertical, and lateral velocities, respectively. The total uncertainty of the turbulent kinetic energy, turbulence intensities, and Reynolds shear stresses were evaluated as ±5%, ±6%, and ±15% of their respective local maximum.

The ADV is mounted on a three-dimension Parker IPS traversing mechanism that is electronically controlled in two axes by a Galil controller and two servo motors. The movements along the *y* and *z* axes are automated while the *x* axis is moved manually. The

traversing mechanism can be aligned to an accuracy of ±2 mm, ±0.5 mm, and ±2.2 mm in the *x*, *y*, and *z* directions respectively. A cable was connected between the controller and the ADV sync port. Through this port the controller was able to communicate with the ADV during the sampling process. The ADV was connected to a personal computer that was used to set the ADV parameters. The recorded data was saved directly onto the computer.

3.3 *Methods*

To begin an experiment the discharge through the channel was adjusted with the butterfly valve and the downstream tailwater level was regulated with the wicket gate. Once the flow had reached steady state, the ADV was positioned at the appropriate *x* coordinate and was configured with the appropriate parameters and sampling time. A preselected grid of *y* and *z* coordinates and sampling time were inputted into the controller. Once the sampling procedure was started the controller positioned the ADV at the first inputted coordinates and sent a sync pulse to the ADV to start sampling. After the predefined sampling time, the controller would move the ADV to the next point and send a sync pulse to the ADV. This was repeated, without user interaction, until all coordinates had been sampled. This procedure was repeated for all selected streamwise locations. During sampling, the discharge and tailwater level were monitored to ensure they remained constant. The recorded data was then processed to eliminate data that did not meet minimum quality requirements using MATLAB. Additional details on data quality and data processing can be found in Appendix A.

3.4 *Experimental Conditions*

The orifice used in this study had a height, b_o = 60 mm and width, b = 360 mm. The orifice was positioned 240 mm from the channel bottom giving an offset ratio of 4. The offset ratio is calculated as h/b_o where h is the distance between the channel bottom and the orifice.

Preliminary experiments were conducted to explore the effects of Reynolds number. The experimental conditions can be found in Table 3-1. From these experiments it was concluded that a Reynolds number of 53,000 and matching discharge of 19.0 l/s would be appropriate while performing the experiments investigating tailwater level and asymmetry ratio effects. A summary of these findings are presented in Chapter 4 while a complete analysis can be found in Durand et al. (2014).

Table 3-1 Experimental conditions of Reynolds number experiments

Reynolds number *Re* [-]	Discharge *Q* [l/s]
34,000	12.2
53,000	19.0
86,000	31.0

The discharge, Q, was set to 19.0 l/s for the tailwater level and asymmetry ratio experiments. This resulted in a jet bulk velocity, U_b, Reynolds Number, Re, and Froude number, Fr, at the orifice of 0.880 m/s, 53,000, and 1.147, respectively.

The experimental conditions of the tailwater experiment can be seen in Table 3-2. Only the tailwater level, y_t, was changed while all other variables remained constant. The orifice was located in the center of the channel for an asymmetry ratio, AR, of zero.

Table 3-3 shows the experimental conditions of the asymmetry experiment. All variables other than the asymmetry ratio, AR, were kept constant with the tailwater level, y_t, set to

750 mm. The asymmetry ratio is defined as the $2b'/B$ where b' [mm] is the z coordinate at the center of the orifice and B [mm] is the channel width. An asymmetry ratio, AR, of 0.76 positioned the orifice directly adjacent to the channel wall.

Table 3-2 Experimental conditions of tailwater level experiments

Tailwater level y_t [mm]	Asymmetry ratio AR [-]	Discharge Q [l/s]
750	0.00	19.0
650	0.00	19.0
550	0.00	19.0
350	0.00	19.0

Table 3-3 Experimental conditions of asymmetry ratio experiments

Asymmetry ratio AR [-]	Tailwater level y_t [mm]	Discharge Q [l/s]
0.00	750	19.0
0.20	750	19.0
0.40	750	19.0
0.60	750	19.0
0.76	750	19.0

CHAPTER 4: REYNOLDS NUMBER EXPERIMENTS

Preliminary tests were conducted at the three Reynolds numbers listed in Table 3-1. The information and experience obtained from these experiments helped in selecting the Reynolds number used in subsequent experiments. The effects of Reynolds number on flow characteristics of three-dimensional offset jets such as decay rate, jet spread, and distribution of mean velocity and higher order turbulence statistics were explored. This chapter will provide a summary of the pertinent findings. A full analysis is available in Durand et al. (2014)

4.1 *Streamwise Flow Development*

The maximum streamwise mean velocity, U_m, of an offset jet is known to decay with increasing streamwise distance. Figure 4-1 shows the dimensionless maximum streamwise mean velocity, U_m/U_b, for all three experiments. A power law of the form $U_m \propto x^{-n_p}$ was used to evaluate the decay rate of the jet within the fully developed wall jet region. Curves were fitted to points within the streamwise extent of $20 \leq x/b_o \leq 50$ and can be seen in Figure 4-1 (a). The decay rates, n_p, and adjusted R-squared values can be

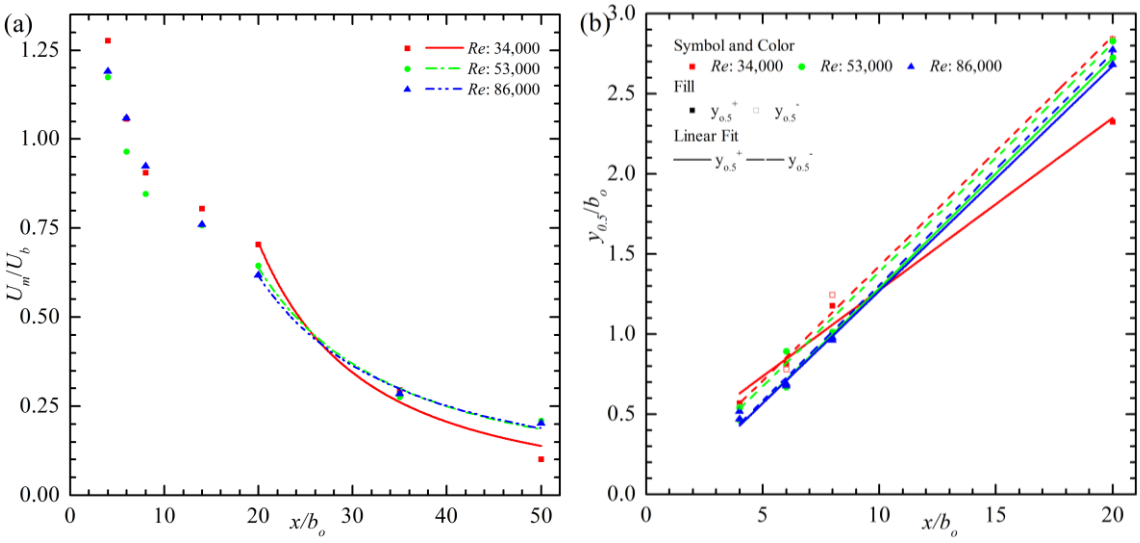

Figure 4-1 (a) Decay and (b) spread of Reynolds number experiments

seen in Table 4-1 for all three experiments. The decay rate, n_p, is highest at the lowest Reynolds number of 34,000 and decreases with increasing Reynolds number. The difference in decay rate between the two lowest Reynolds numbers is significant which shows the jet to be Reynolds number dependent. At the two highest Reynolds number the decay rates are similar. This indicates that the jet becomes independent of Reynolds number at this higher range, $53{,}000 \leq \mathrm{Re} \leq 86{,}000$. The decay rates in this study are higher than previously reported for three-dimensional offset jets. For example, Agelin-Chaab and Tachie (2011b) and Davis and Winarto (1980) reported decay rate, n_p, of 1.17 ± 0.03 and 1.15, respectively. Differences in decay rates have been attributed to initial conditions such as the nozzle geometry, exit Reynolds number, and turbulence levels in the channel. The present study utilized a sharp-edged nozzle while previously reported studies made use of long pipe and contoured nozzles. The channel in this study was highly turbulent, in contrast, previous studies were performed in wind tunnels which typically have low turbulence levels. These varied conditions likely lead to different decay rates.

Table 4-1 Power law decay rates within the wall jet region of Reynolds number experiments

Reynolds number Re [-]	Decay rate n_p [-]	Adjusted R-squared
34,000	1.782	0.973
53,000	1.356	0.978
86,000	1.292	0.992

A jet spreads in both the vertical and lateral directions as it entrains the surrounding fluid. The vertical spread was examined in both the inner and outer shear layer. It was expected that the channel bottom would limit the spread in the inner shear layer. The spread of the jets at different Reynolds numbers can be seen in Figure 4-1 (b). A linear equation, $y_{o.5}/b_o = m(x/b_o - x_o)$, where m is the spread rate and x_o is the dimensionless virtual origin, was fitted to the spread in order to measure the spread rate. The spread rate, m, virtual origin, x_o, and adjusted R-squared values are shown in Table 4-2. The spread rates, m, are evaluated with high confidence as for all cases the R-squared value is high. With the exception of the lowest Reynolds number, the spread rates are nearly identical in both inner and outer shear layers suggesting the wall has minimal impact in the streamwise extent of $4 \leq x/b_o \leq 20$. For the two highest Reynolds numbers the spread rate is equivalent and independent of Reynolds number.

Table 4-2 Vertical spread rate of Reynolds number experiments

	Reynolds number Re [-]	Spread rate m [-]	Virtual origin x_o [-]	Adjusted R-squared
$y_{0.5}^{+}$	34,000	0.107	-1.864	0.984
	53,000	0.143	1.020	0.998
	86,000	0.140	0.948	0.999
$y_{0.5}^{-}$	34,000	0.143	0.041	0.992
	53,000	0.142	0.255	0.993
	86,000	0.145	0.968	0.995

For the exception of the outer shear layer of the lowest Reynolds number, the virtual origins, x_o, are all positive. The virtual origin, x_o, can give insight into the jet constriction due to the vena contracta effect and the length of the potential core. It is difficult to make significant conclusions from the virtual origin, x_o, in this study as no vena contracta or potential core are observed at the most upstream sampled streamwise distance, $x/b_o = 4$. Within the inner shear layer the virtual origin increases with Reynolds number. This alludes that the vena contracta has a stronger effect or the jet may have a longer potential core with increasing Reynolds number.

4.2 *Mean Velocities*

Figure 4-2 shows the streamwise, vertical, and lateral dimensional mean velocity profiles for the Reynolds number of 53,000. The velocities were normalized by the local maximum velocity, U_m. The y coordinates are centered on y_m and normalized by the local jet half width, $y_{0.5}$. The local jet half width, $y_{0.5}$, represents the jet half width in the inner and outer shear layer, $y_{0.5}^-$ and $y_{0.5}^+$, respectively. This normalizing convention is used throughout this study.

For the streamwise extent of $4 \leq x/b_o \leq 20$ the streamwise mean velocity profiles, shown in Figure 4-2 (a), collapse onto each other reasonably well indicating that the jet has achieved self-similarity. A negative velocity can be seen in the regions beyond $y/y_{0.5} = \pm 2$ of streamwise locations $4 \leq x/b_o \leq 8$. This indicates a recirculation zone in both the inner and outer region of the jet. Similar characteristics can be observed in Figure 4-3 for Reynolds numbers of 34,000 and 86,000.

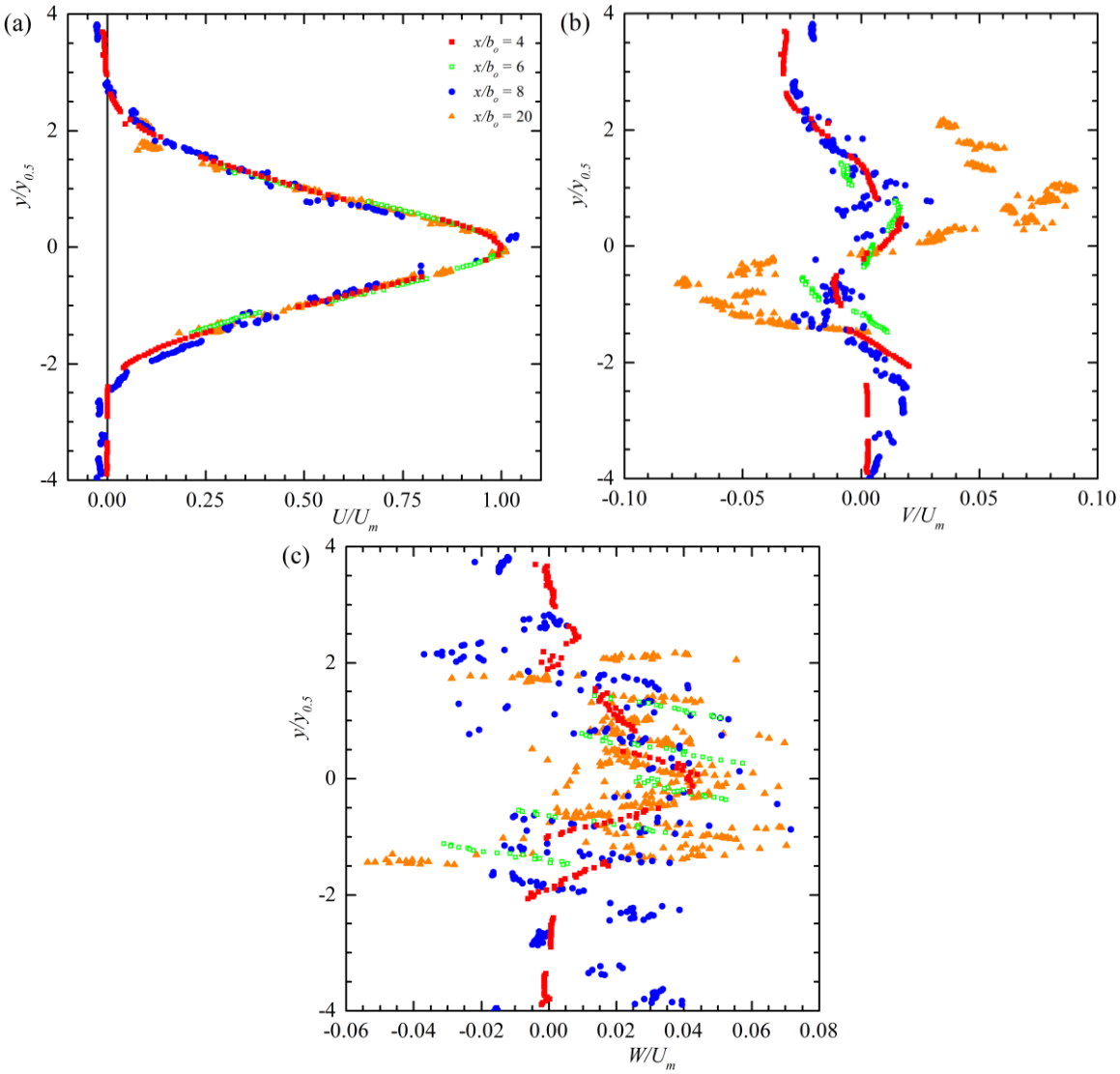

Figure 4-2 Profiles of (a) streamwise, (b) vertical, and (c) lateral mean velocities for *Re* 53,000

The vertical mean velocities, shown in Figure 4-2 (b), display an antisymmetric profile. The positive velocities in the outer shear layer and negative velocities in the inner shear layer indicate outward spreading of the jet. Beyond the two shear layers the velocities reverse direction and orient themselves towards the center of the jet. This is an indication of entrainment. The magnitude of vertical velocities, V/U_m, increases with streamwise distance, indicating that the vertical velocity, V, is not decaying with the streamwise velocity, U. In fact the profiles of the vertical velocity, V, were observed to increase in

magnitude with streamwise distance, an indication of intensifying entrainment. This was observed at all three Reynolds numbers.

Profiles of lateral velocity are shown in Figure 4-2 (c). Unlike the streamwise and vertical mean velocities the lateral mean velocity does not follow an obvious trend. There exists a small bias towards positive values and this may indicate a slight misalignment of the ADV with the symmetry plane or a rotational misalignment with the coordinate system. At all three Reynolds numbers the reported velocities are essentially zero throughout the profiles. This was expected as the sampling was performed within the symmetry plane.

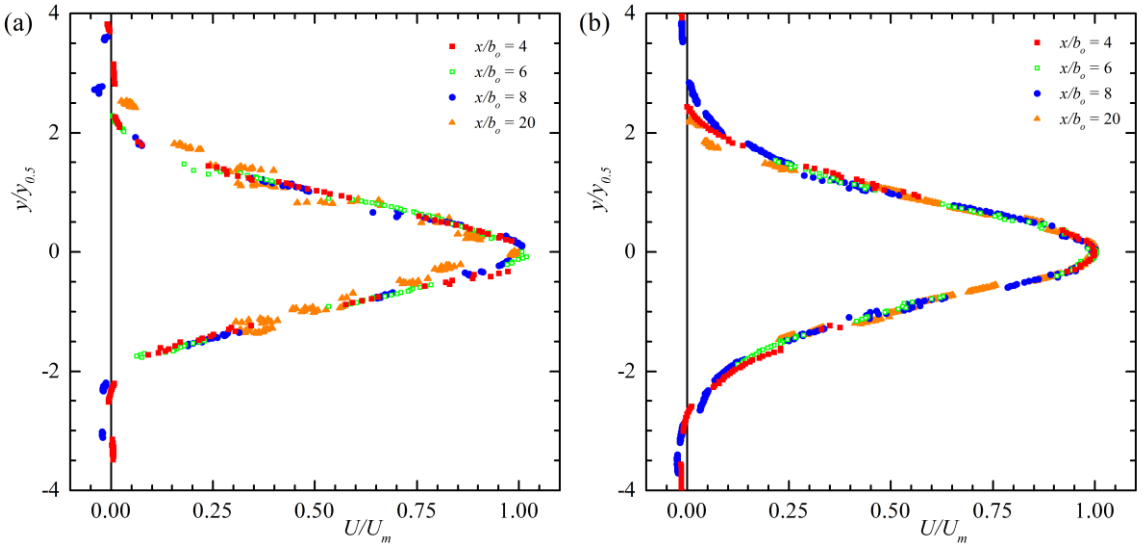

Figure 4-3 Profiles of streamwise mean velocities for (a) *Re* 34,000 and (b) *Re* 86,000

4.3 *Turbulent Kinetic Energy*

Figure 4-4 shows profiles of turbulent kinetic energy at all three Reynolds numbers at streamwise extents of x/b_o = 4, 8, and 20. The turbulent kinetic energy is calculated using all three Reynolds normal stresses as $k = 1/2\,(u_{rms}^2 + v_{rms}^2 + w_{rms}^2)$. This is possible because the ADV simultaneously measures all three components of velocity.

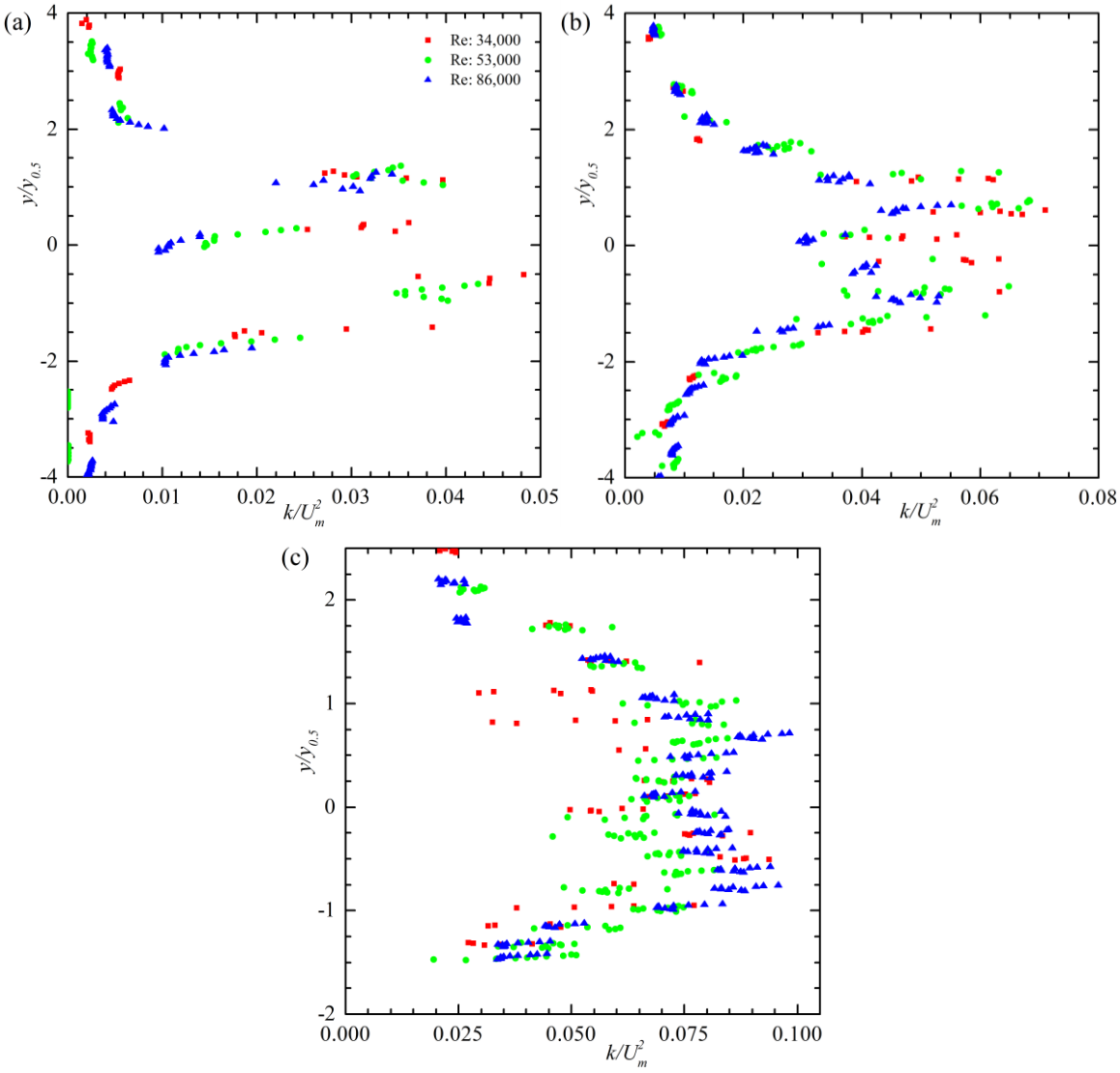

Figure 4-4 Profiles of turbulent kinetic energy at streamwise locations of (a) x/b_o=4, (b) x/b_o=8, and (c) x/b_o=20

The profiles of turbulent kinetic energy feature a double peak that is most pronounced near the orifice and diminishes with increasing streamwise distance. The peaks indicate regions of high shear located near the jet half widths, $y_{0.5}$. At the location of maximum velocity, y_m, the magnitude of the turbulent kinetic energy is reduced. This was expected based on the profiles of mean velocity. With increasing streamwise distance the double peak becomes less pronounced, which is explained by a reduction of the velocity gradient. The normalized turbulent kinetic energy, k/U_m^2, increases with streamwise distance indicating that the velocity decays at a faster rate than the turbulent kinetic

energy, *k*. At the three displayed locations the profiles of all three Reynolds numbers collapse onto each other with peaks of comparable magnitude indicating no significant Reynolds number dependence.

4.4 *Reynolds Shear Stresses*

Reynolds shear stresses for all three Reynolds numbers are shown in Figure 4-5 and Figure 4-6. The profiles of Reynolds shear stress in the *x*-*y* plane, *uv*, collapse onto each other and increase just slightly in magnitude with increasing streamwise distance when

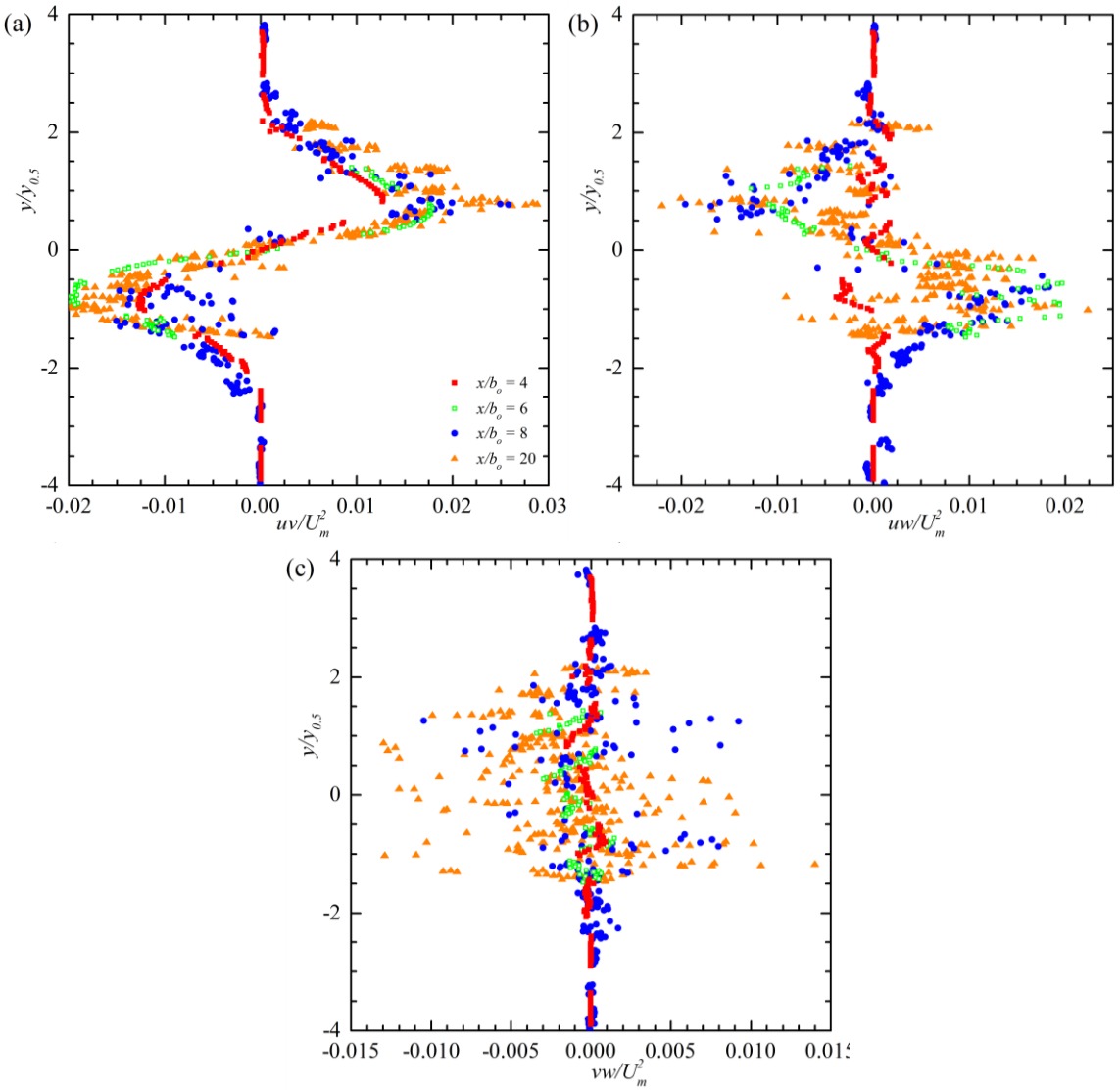

Figure 4-5 Profiles of Reynolds shear stresses (a) *uv*, (b) *uw*, and (c) *vw* for *Re* 53,000

normalized by the jet half width, $y_{0.5}$, and local maximum streamwise velocity, U_m. The Reynolds shear stress *uv* decays at a similar rate as U_m^2 indicating that the production of turbulence from this term is decreasing. The characteristics of Reynolds shear stress *uv* is similar at all three Reynolds numbers. Figure 4-5 also contains the profiles of Reynolds shear stresses in the *xz* and *vz*-planes, *uw* and *vw*. Like the profiles of Reynolds shear stress *uv*, the profiles of *uw* are antisymmetric with greater magnitudes focused within the inner and outer shear layers at all Reynolds numbers. The magnitude of Reynolds shear stress *uw* were observed to decrease with increasing Reynolds number, however, they remain of the same order of magnitude and maintain an increasing trend with increasing streamwise distance.

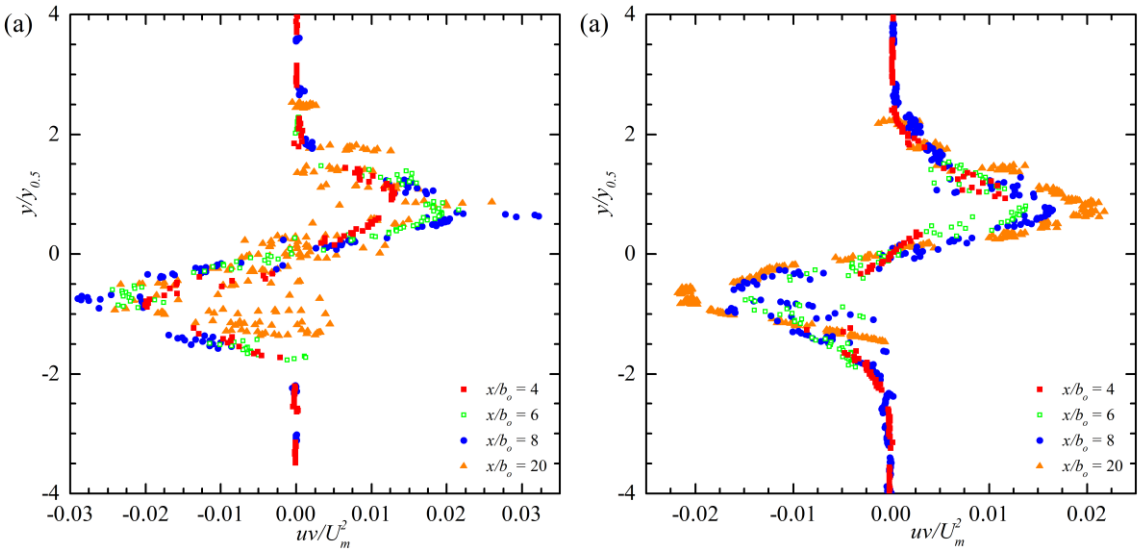

Figure 4-6 Profiles of Reynolds shear stress *uv* for (a) *Re* 34,000 and (b) *Re* 86,000

4.5 *Summary*

Preliminary experiments performed at three different Reynolds numbers permitted an assessment of the effects of Reynolds number on decay rates, spread rates, and distribution of mean velocities and turbulence statistics. Reynolds number effects on decay rate were insignificant at Reynolds numbers Re ≥ 53,000 and spread rates within

the region of $x/b_o = 20$ were independent of Reynolds number. No significant effects of Reynolds number were observed on profiles of mean velocities, *U*, *V*, and *W*, and turbulent kinetic energy, *k*. Although not shown here, the profiles of turbulence intensities, u_{rms}, v_{rms}, w_{rms}, were not significantly affected from changes in Reynolds number (Durand et al. 2014). The magnitude of Reynolds shear stress *uw* was reduced at higher Reynolds number but remain of the same order of magnitude, the Reynolds shear stress *uv* was independent of Reynolds number. The effects of Reynolds number were found to be small within the range of Reynolds number tested in these experiments. From the information and experience gathered in these preliminary experiments it was decided that a Reynolds number of 53,000, achieved with a discharge of 19.0 l/s, would be appropriate for the subsequent tailwater and asymmetry experiments. Most industrial applications operate at a high Reynolds number. Performing the subsequent experiments at a Reynolds number of 53,000 will make the results from these experiments relevant and applicable to the operations of industrial applications.

CHAPTER 5: TAILWATER LEVEL EXPERIMENTS

Four sets of experiments were conducted at different tailwater levels as outlined in Table 3-2. The discharge was kept constant at 19.0 l/s which resulted in a Reynolds number of 53,000. This chapter will evaluate the effects of different tailwater levels on three-dimensional offset jets. First, the effects on streamwise flow development will be evaluated. This includes the vertical location of maximum velocity, y_m, the maximum streamwise mean velocity decay, n_l and n_p, and the vertical and lateral spread rates, m, l_1, and l_2. Subsequently, the effects of tailwater level on profiles of mean velocities and turbulence statistics will be assessed.

5.1 *Streamwise Flow Development*

As an offset jet issues from an orifice the pressure within the recirculation region will be reduced due to entrainment. This causes the jet to curve towards the solid boundary. The dimensionless vertical location of the local maximum streamwise mean velocity, y_m/b_o, is plotted with normalized streamwise distance, x/b_o, in Figure 5-1 (a). It can be seen that the jet curves towards the channel bottom except at the lowest tailwater level where the

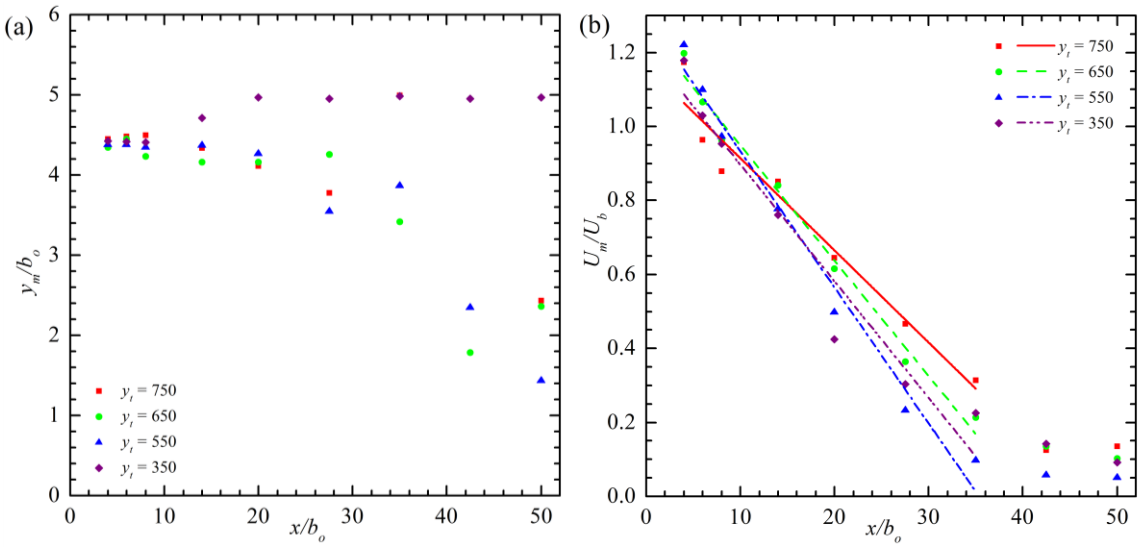

Figure 5-1 (a) Vertical location of maximum streamwise mean velocity (b) Decay of streamwise mean velocity

jet moves towards the water surface instead. At the lowest tailwater the recirculation zone above the jet was observed to be shorter than at higher tailwater levels. The limited water depth above the jet causes the jet to quickly spread to the water surface reducing the recirculation zone above the jet. It will be seen throughout the analysis that at the lowest tailwater level of y_t = 350 mm the jet behaves differently than at higher tailwater levels of y_t = 550 mm, 650 mm, and 750 mm.

Several methods such as pressure taps and dye visualization were attempted to measure the reattachment length near the channel bottom, however, none proved to be successful. The reattachment length, an important feature of an offset jet, is therefore absent in this study. From velocity profiles it was seen that the jet reattaches to the channel bottom within the region of $8 \leq x/b_o \leq 20$. Beyond the streamwise extent of x/b_o = 20, the jet evolves as a wall jet.

The maximum streamwise velocity of an offset jet is known to decrease with streamwise distance. Figure 5-1 (b) shows the local maximum mean streamwise velocity of the jets at different tailwater levels. To calculate the linear decay rate, n_l, a linear function of the

form $U_m/U_b = U_v - n_l \times (x/b_o)$ was fitted through the streamwise extent of $4 \leq x/b_o \leq 35$. The y-intercept of the linear fit is referred to as the virtual velocity, U_v, and is dimensionless. The decay rates, n_l, virtual velocity, U_v, and adjusted R-squared values can be seen in Table 5-1. The decay rate and virtual velocity can be seen to increase with decreasing tailwater at the three highest tailwater levels. At the lowest tailwater level the decay rate reduces, so does the virtual velocity.

Table 5-1 Linear decay rates of tailwater experiments

Tailwater level y_t [mm]	Decay rate n_l [-]	Virtual velocity U_v [-]	Adjusted R-squared
750	0.025	1.163	0.945
650	0.031	1.261	0.984
550	0.037	1.301	0.978
350	0.032	1.212	0.933

In previous studies the decay rate was calculated by fitting a curve of the form $U_m \propto x^{-n_p}$ within the self-similar wall jet region. Local maximum streamwise mean velocities for $x/b_o \geq 20$ from this study were fitted to this equation to facilitate a comparison to previous studies. The fitted curves can be seen in Figure 5-2 and the decay

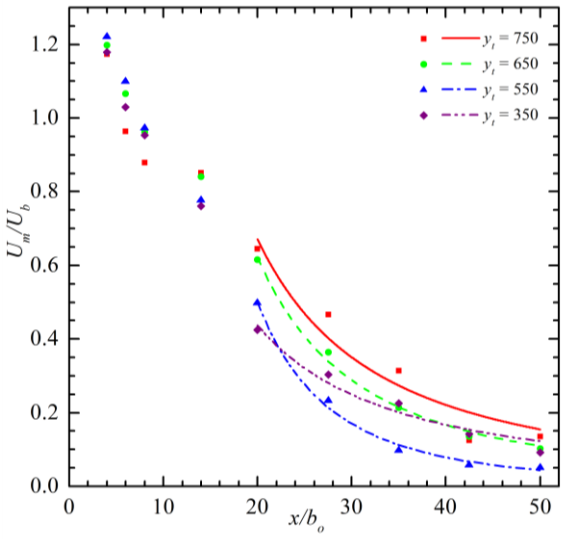

Figure 5-2 Power fit of maximum streamwise velocity within the wall jet region

rates, n_p, with adjusted R-squared values can be seen in Table 5-2. The decay rates within the wall jet region can be seen to increase with decreasing tailwater for the three highest tailwater levels, a similar trend as the linear decay rate. At the lowest tailwater, y_t = 350 mm, the decay rate is the lowest of all experiments. The decay rates within the wall jet region reported in this study are higher than the range of decay rates, $1.15 \leq n_p \leq 1.20$, reported in previous studies (Davis and Winarto 1980, Agelin-Chaab and Tachie 2011b). The higher decay rates obtained in this study are attributed to the nozzle geometry and turbulence levels. A sharp-edged nozzle and highly turbulent channel was used in this study while previous studies utilized long pipe and contoured nozzles.

Table 5-2 Power law decay rates of tailwater experiments

Tailwater level y_t [mm]	Decay rate n_p [-]	Adjusted R-squared
750	1.603	0.916
650	1.898	0.994
550	2.661	0.993
350	1.390	0.958

The jet spreads both vertically and laterally as it moves downstream by entraining the surrounding fluid. The jet half width, $y_{0.5}$ and $z_{0.5}$, is a measure of the jet spread. The spread rate, m, is the rate at which the jet half width increases with streamwise distance. The vertical jet half widths, $y^+_{0.5}$ and $y^-_{0.5}$, are shown in Figure 5-3 for the streamwise extent of $4 \leq x/b_o \leq 20$ with fitted lines showing the spread rates. Table 5-3 lists the vertical spread rate, m, the virtual origin of spread, x_o, and the adjusted R-squared value from Figure 5-3. At the lowest tailwater, two of the three points used to calculate the spread rate in the outer shear layer were extrapolated from partial velocity profiles due to limited water levels above the jet. It is typical for the decay and spread rate to follow a similar trend, an increased spread rate would go along with a higher decay rate. However

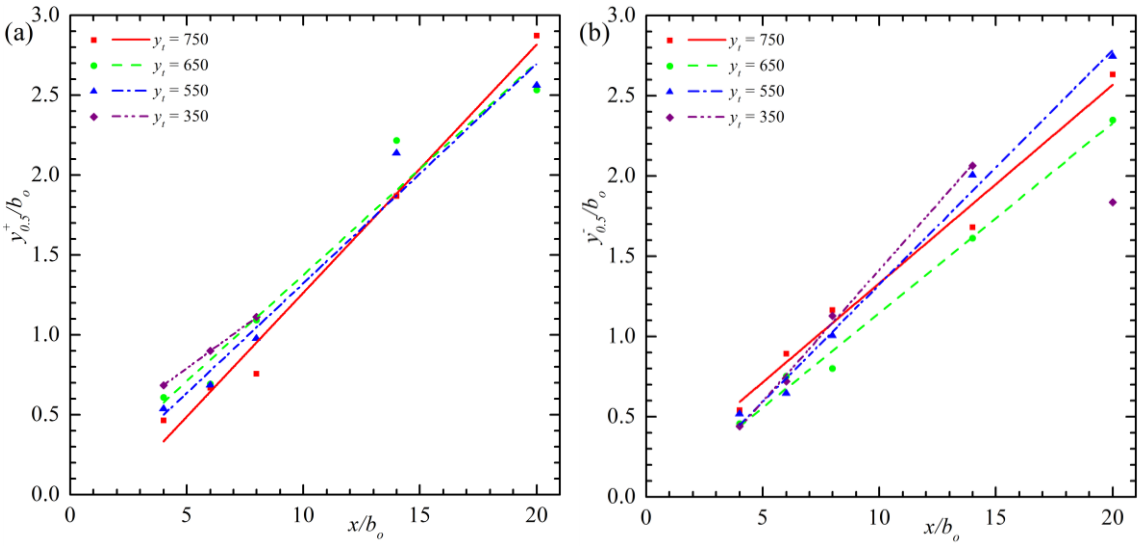

Figure 5-3 Vertical spread rate of tailwater experiment in (a) outer shear layer and (b) inner shear layer

this is not the case for the vertical spread rate in this study as the spread rate, m, does not follow the same trend as the decay rate, n_l. When excluding the lowest tailwater, the spread rates vary less than the decay rates indicating the tailwater level to have a smaller impact on vertical spread rate, m, than decay rate, n_l.

Table 5-3 Vertical spread rate of tailwater experiments

	Tailwater level y_t [mm]	Spread rate m [-]	Virtual origin x_o [-]	Adjusted R-squared
$y^+_{0.5}$	750	0.155	1.856	0.981
	650	0.133	-0.350	0.937
	550	0.137	0.367	0.959
	350	0.107	-2.405	0.999
$y^-_{0.5}$	750	0.123	0.787	0.982
	650	0.118	-0.283	0.989
	550	0.146	-0.936	0.991
	350	0.164	-0.136	0.997

The lateral spread rate is an interesting feature of a three-dimensional offset jet. The lateral jet half widths, $z_{0.5}$, were calculated from lateral profiles measured at the vertical location of y_m. The dimensionless jet half width, $z_{0.5}/b_o$, are plotted in Figure 5-4 for all four tailwater levels. The jet half width, $z_{0.5}$, can be seen to decrease for a significant streamwise distance. This is attributed to the vena contracta effect. A quadratic equation

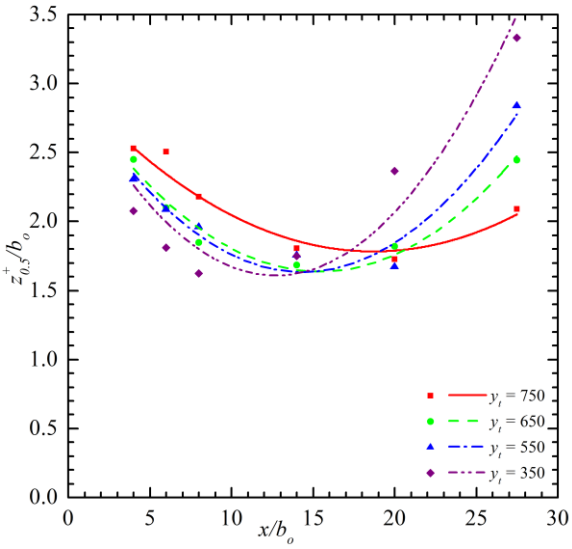

Figure 5-4 Lateral spread rate of tailwater experiment

of the form $(z_{0.5}/b_o) = 3 - l_1(x/b_o) + l_2(x/b_o)^2$ was fitted to the jet width data to evaluate the lateral spread. The coefficients of lateral spreading, l_1 and l_2, can be seen in Table 5-4 with the adjusted R-squared values. The inflection point of lateral spreading, x_{vc}, calculated from the quadratic equation, can also be seen in Table 5-4 for all four experiments. The streamwise distance of the inflection point can be seen to increase with increasing tailwater level, however, the reduction in jet width is more severe at lower tailwater levels. Both coefficient of lateral spreading, l_1 and l_2, increase with decreasing tailwater.

Table 5-4 Coefficients of lateral spreading and inflection points of tailwater experiments

	Tailwater level y_t [mm]	Coefficients of lateral spreading l_1 [-]	l_2 [-]	Adjusted R-squared	Inflection point x_{vc}/b_o [-]
$z^+_{0.5}$	750	0.130	0.0035	0.998	18.70
	650	0.177	0.0057	0.999	15.40
	550	0.190	0.0066	0.997	14.39
	350	0.219	0.0086	0.988	12.70

The vertical profiles do not show a reduction in jet width due to the vena contracta as seen in the lateral profiles. This difference is attributed to the aspect ratio, $b/b_o = 6$, of the orifice. The larger width of the orifice allows a larger decrease in lateral spread that is

seen at a further streamwise distance. The signs of a vena contracta effects in the vertical profiles have disappeared by the first sampled streamwise distance of $x/b_o = 4$.

5.2 *Mean Velocities*

Vertical and lateral profiles of streamwise, vertical, and lateral velocities are shown in Figure 5-5 to Figure 5-8. The velocities were normalized by the local maximum velocity, U_m. The y and z coordinates are centered on y_m and the orifice centerline, b', respectively, and normalized by the local jet half width, $y_{0.5}$ and $z_{0.5}$, respectively. The local jet half width, $y_{0.5}$ and $z_{0.5}$, represent the jet half width in its respective shear layer.

The vertical profiles of normalized streamwise mean velocity, U/U_m, are seen to collapse onto each other indicating that the jet achieves self-similarity at a streamwise distance of $x/b_o = 4$ from the nozzle. Small negative velocities are observed beyond $y/y_{0.5} = \pm 2$ indicating recirculation in both the inner and outer shear layer of the jets at the three highest tailwater levels. At the lowest tailwater level the recirculation zone of the inner region is not significant. It was not possible to provide complete measurements of the outer region because the ADV was located too close to the water surface. The outer recirculation region was however observed to be limited in length.

The vertical profiles of normalized vertical velocity, V/U_m, are antisymmetric with peak values near the jet half width in both the outer and inner shear layer. The negative and positive values in the inner and outer shear layer, respectively, indicate outwards spreading of the jet into the surrounding fluid. Beyond the shear layers the sign of the velocity reverses indicating entrainment of the surrounding fluid into the jet. At all tailwater levels, the magnitude of the peaks of normalized vertical velocities, V/U_m,

initially increases with streamwise distance and subsequently decreases. The decrease is first noticeable at a streamwise distance of x/b_o = 14, 20, and 20 for tailwater levels of 350 mm, 550 mm, and 650 mm respectively. At a tailwater of 750 mm the vertical velocity is still increasing at a streamwise location of x/b_o = 27.5. This is observed in both the inner and outer shear layer. A look at the vertical velocity profiles, *V*, not shown, shows the velocity to initially increase before decaying. The change from increasing to decreasing occurs at the same streamwise extent for both the inner and outer shear layer for all tailwater levels. The streamwise extent at which the vertical velocity, *V*, starts to decay for all tailwater levels is shown in Table 5-5. It is nearly the same as the inflection of lateral spread, x_{vc}, and increases with increasing tailwater. The limited vertical distance may explain the faster start of the decay of vertical velocity, *V*. Once the vertical velocity, *V*, decreases, it decays at a faster rate than the streamwise velocity, *U*.

Table 5-5 Streamwise range of onset of vertical velocity decay

Tailwater level y_t [mm]	Onset range of vertical velocity decay x/b_o [-]
750	>20
650	14-20
550	14-20
350	8-14

The vertical profiles of normalized lateral velocity, W/U_m, do not show a significant trend. These profiles were measured within the symmetry plane and were expected to be equal close to zero and not show a trend. This is confirmed by these profiles.

The lateral profiles of streamwise velocity, *U*, do not collapse onto each other as the vertical profiles have. Near the orifice the lateral profiles show a core region with nearly constant velocity, at the edge of the core region the velocity drops drastically. With increasing streamwise distance the sharp edge separating the two regions becomes less

pronounced and the profiles develop to resemble a Gaussian distribution. The normalized streamwise velocities, U/U_m, beyond the jet half width $z/z_{0.5} = 1$ increase with streamwise distance. This indicates the streamwise velocities, U, beyond $z/z_{0.5} = 1$ to decay at a slower rate than the maximum velocity of the jet. At tailwater levels of 550 mm and 350 mm the streamwise velocity, U, increases in this region. This was confirmed by looking at lateral profiles of streamwise velocity, U.

The lateral profiles of normalized vertical velocity, V/U_m, are essentially zero. The profiles are located at the vertical location of maximum streamwise mean velocity, y_m, where the shear stress is zero, therefor we expected a zero velocity.

The velocities shown in the lateral profiles of normalized lateral velocity, W/U_m, are very low. The lateral velocity relates to the lateral spreading of the jet. The inflection point of lateral spreading, see Table 5-4 can be used to separate the lateral profiles of lateral velocity into two regions. The lateral velocity near $z/z_{0.5} = 1$ is mostly negative within the upstream region as the vena contracta is dominant. Downstream of the inflection point, x_{vc}, after the vena contracta effect has disappeared, the lateral velocity near $z/z_{0.5} = 1$ changes to positive and the jet begins to spread laterally. The magnitude of lateral velocities, W, are small compared to the streamwise velocity, U. The scatter seen in the lateral profiles is within experimental error.

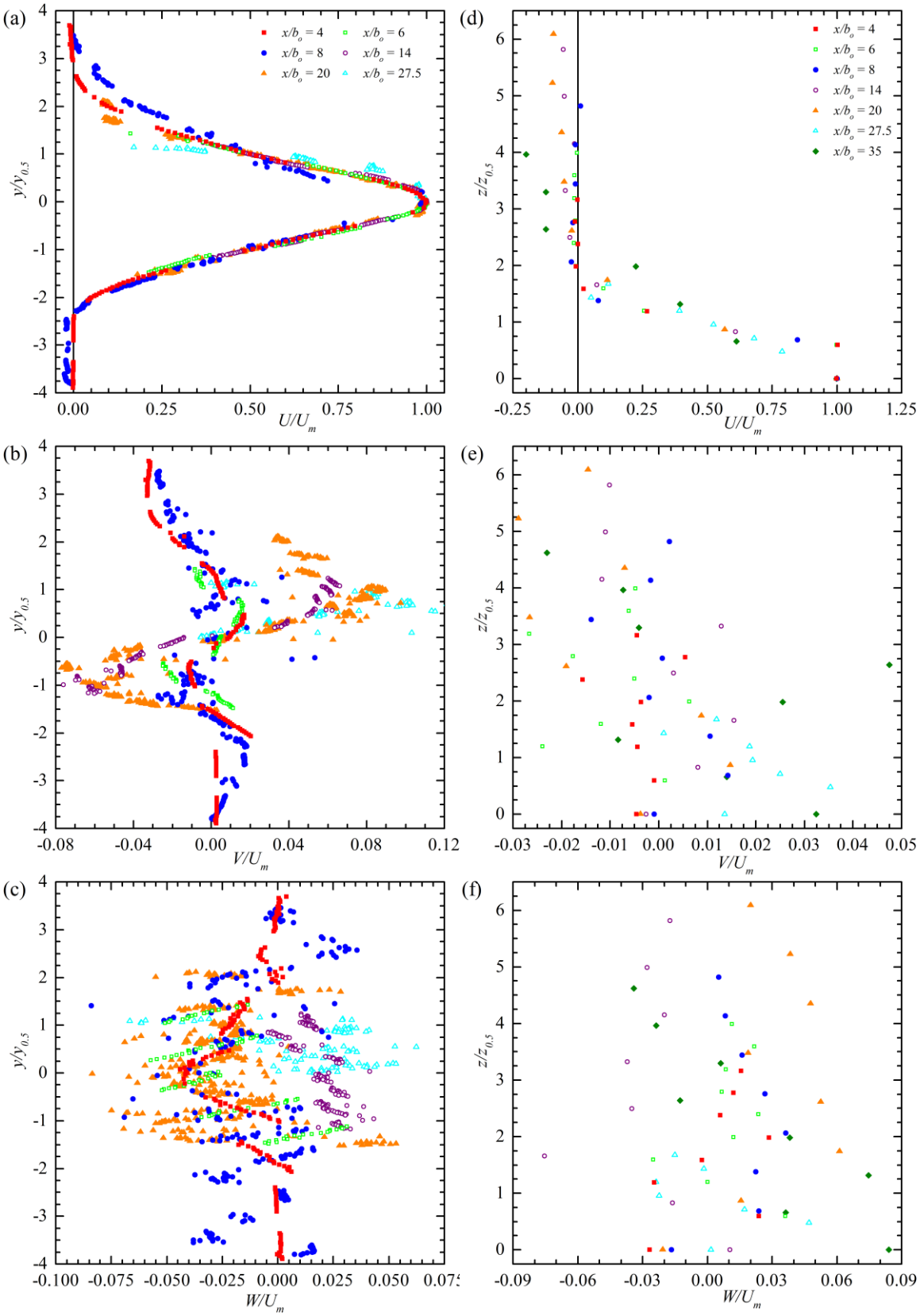

Figure 5-5 Velocity profiles for tailwater level of 750 mm

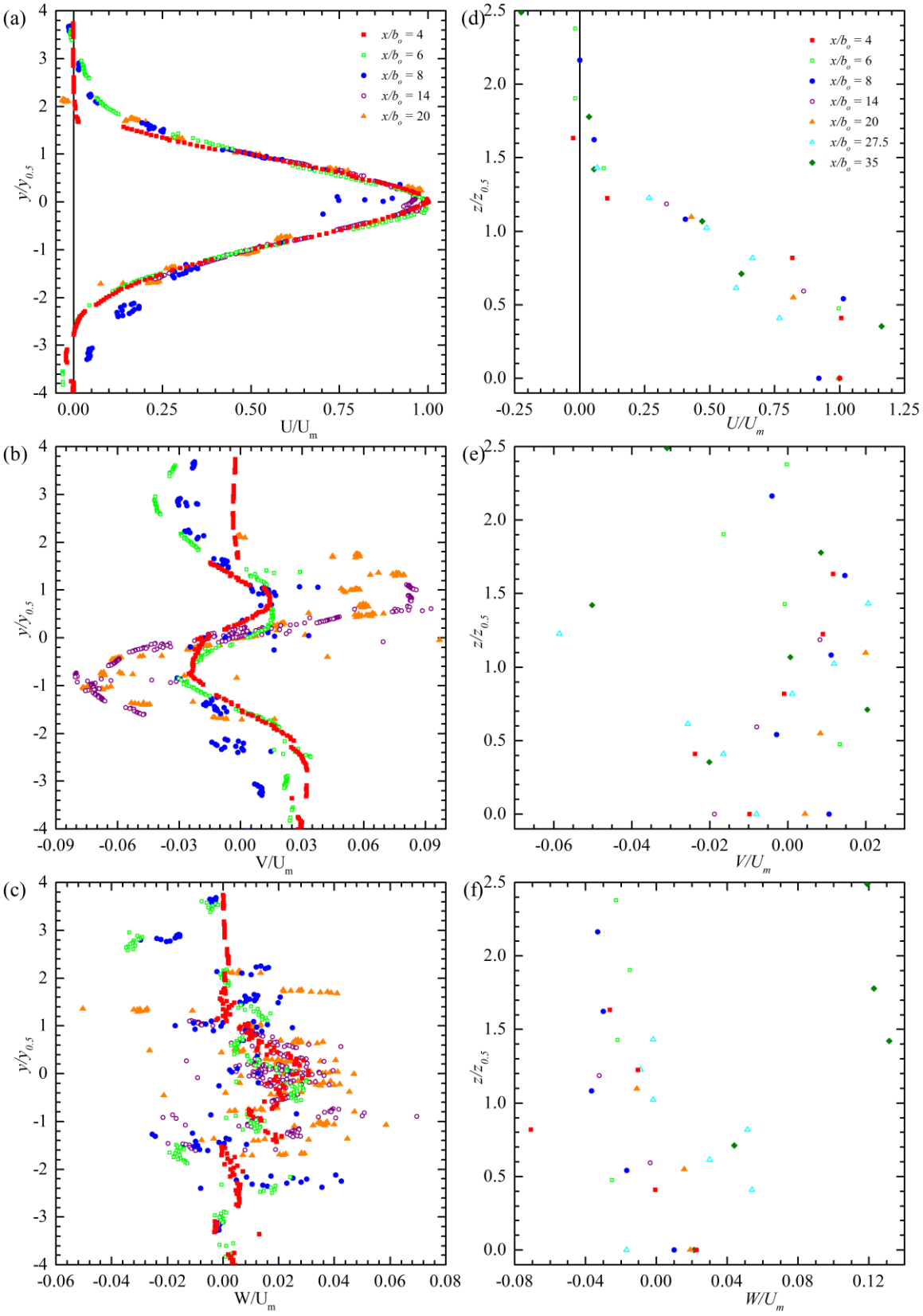

Figure 5-6 Velocity profiles for tailwater level of 650 mm

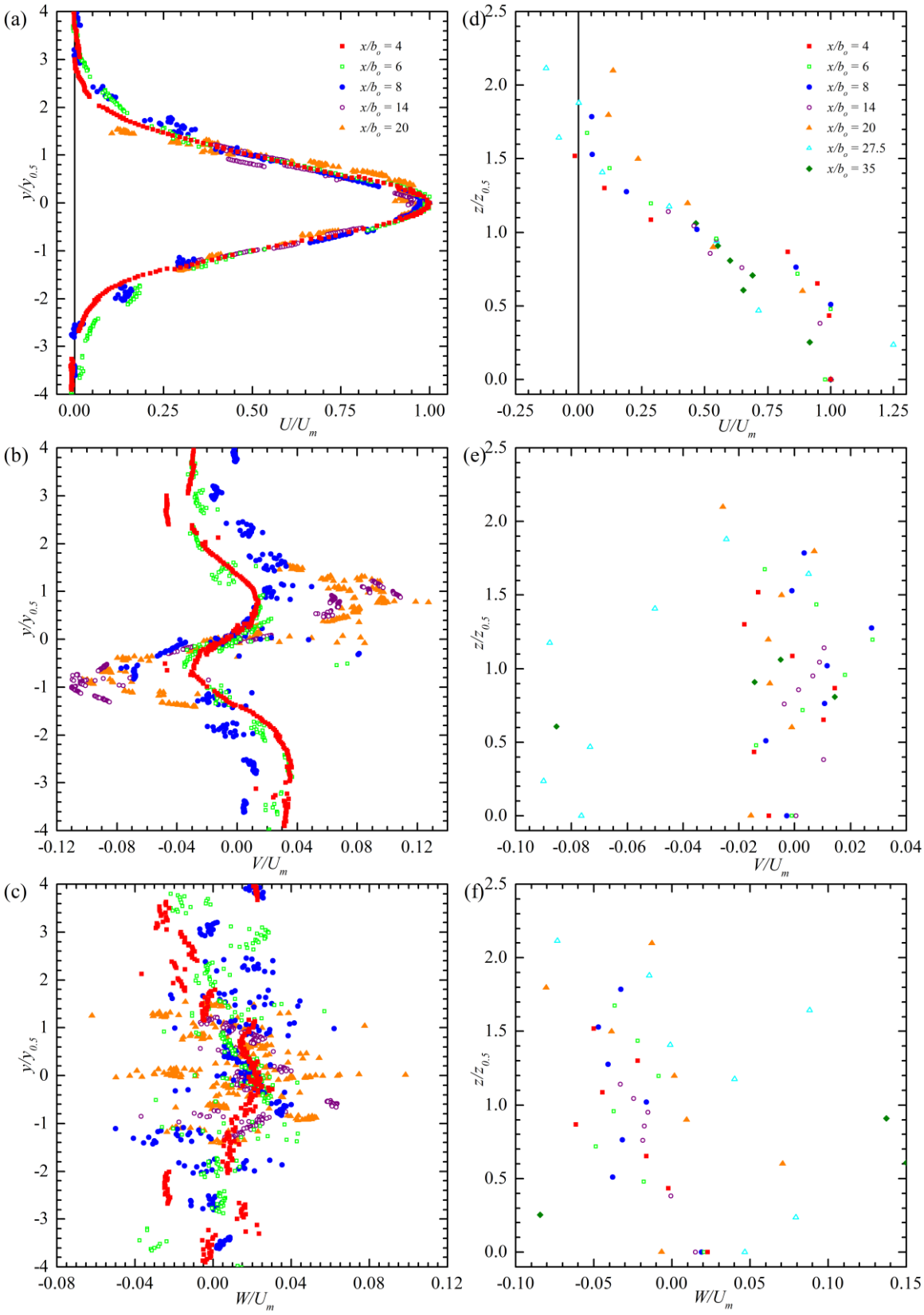

Figure 5-7 Velocity profiles for tailwater level of 550 mm

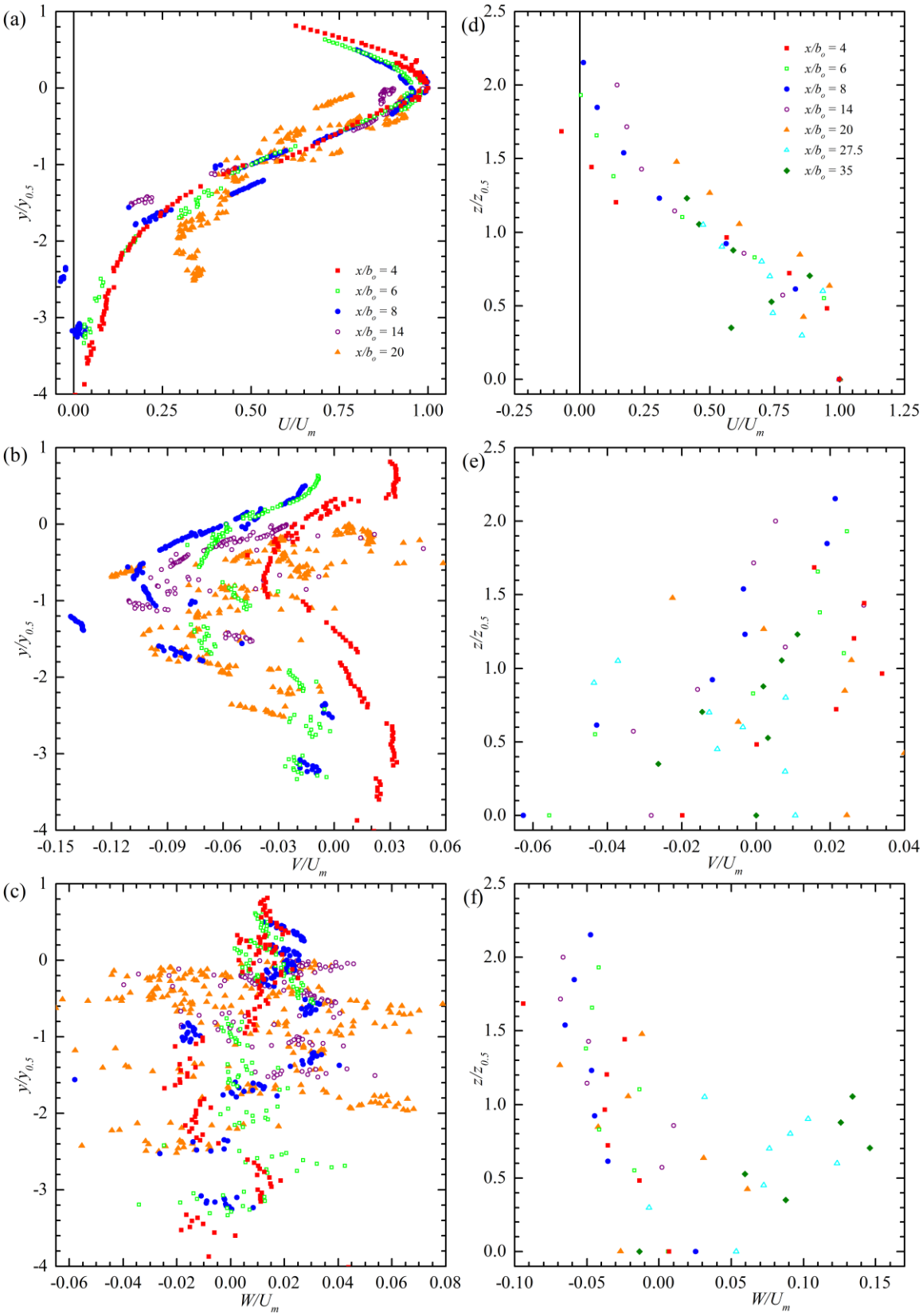

Figure 5-8 Velocity profiles for tailwater level of 350 mm

5.3 *Turbulence Intensities*

Vertical and lateral profiles of normalized turbulence intensities, u_{rms}/U_m, v_{rms}/U_m, and w_{rms}/U_m, are shown in Figure 5-9 to Figure 5-12. For all turbulence intensities, u_{rms}, v_{rms}, w_{rms}, and tailwater levels, the profiles in both the vertical and horizontal plane features a double peak that becomes less pronounced with increasing streamwise distance. Only one side of the lateral profile is presented as the jets were confirmed to be symmetric in the lateral direction. The peaks are located near the jet half width, $y_{0.5}$ and $z_{0.5}$, where the streamwise velocity gradient is near its maximum. At the location of maximum velocity, $y = y_m$ and $z = b'$, where the streamwise velocity gradient is reduced, the turbulence intensities are also reduced. The areas of high shear in the vertical and lateral velocity profiles, V and W, do not coincide with the peaks of turbulence intensities. This shows that the streamwise velocity, U, is the main contributing velocity to turbulence intensities.

The magnitude of dimensionless turbulence intensities increases with streamwise distance indicating that the streamwise mean velocity, U_m, decays at a faster rate than the turbulence intensities. With increasing streamwise distance, the dimensionless turbulence intensity, u_{rms}/U_m, increases the most, followed by w_{rms}/U_m, and v_{rms}/U_m has the smallest increase. This is seen in both vertical and lateral profiles.

When comparing the profiles of dimensionless turbulence intensities between different tailwater levels, their magnitudes are seen to decrease with increasing tailwater. This indicates that a higher tailwater level will decrease the turbulence levels of a jet.

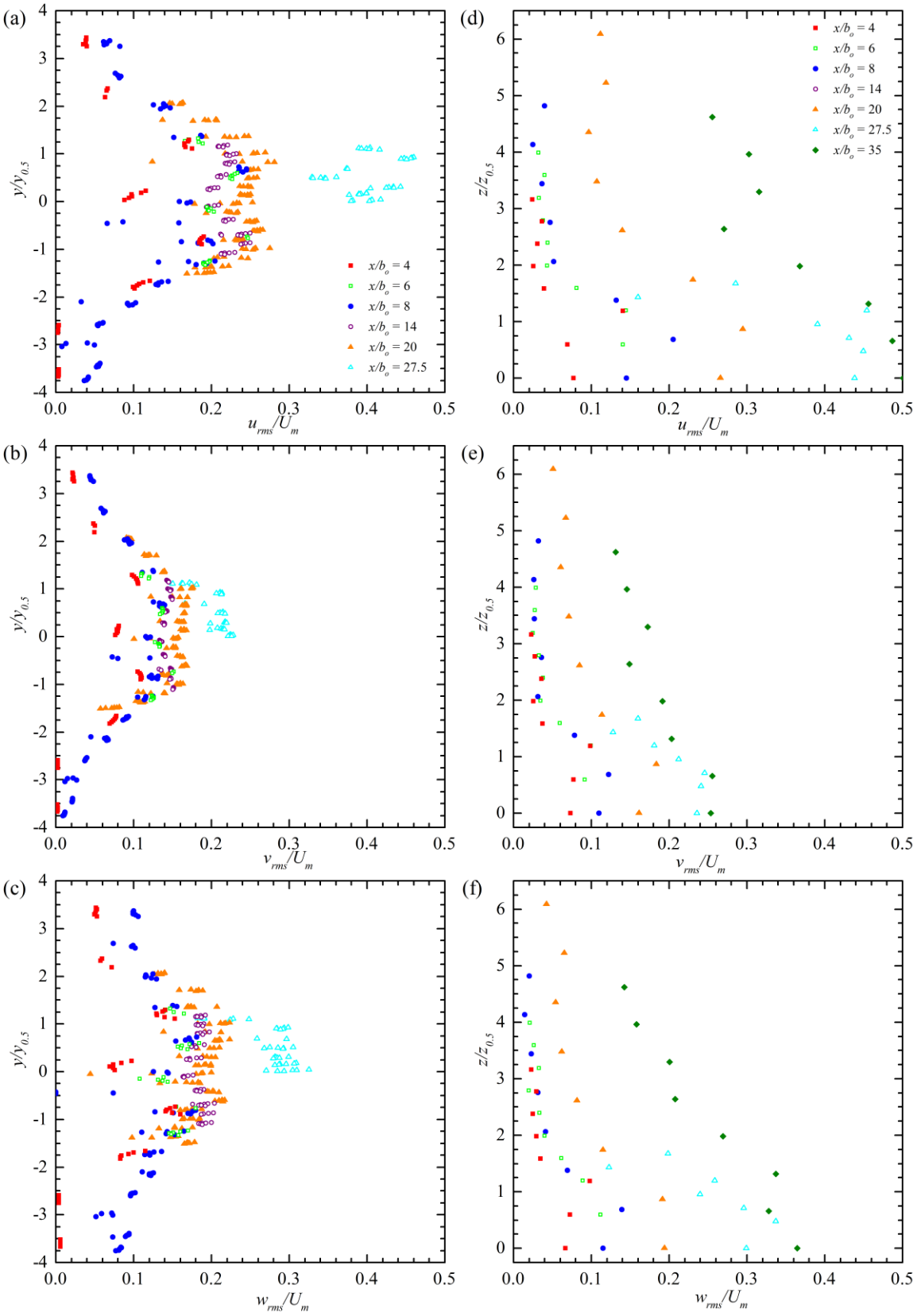

Figure 5-9 Profiles of turbulence intensities for tailwater level of 750 mm

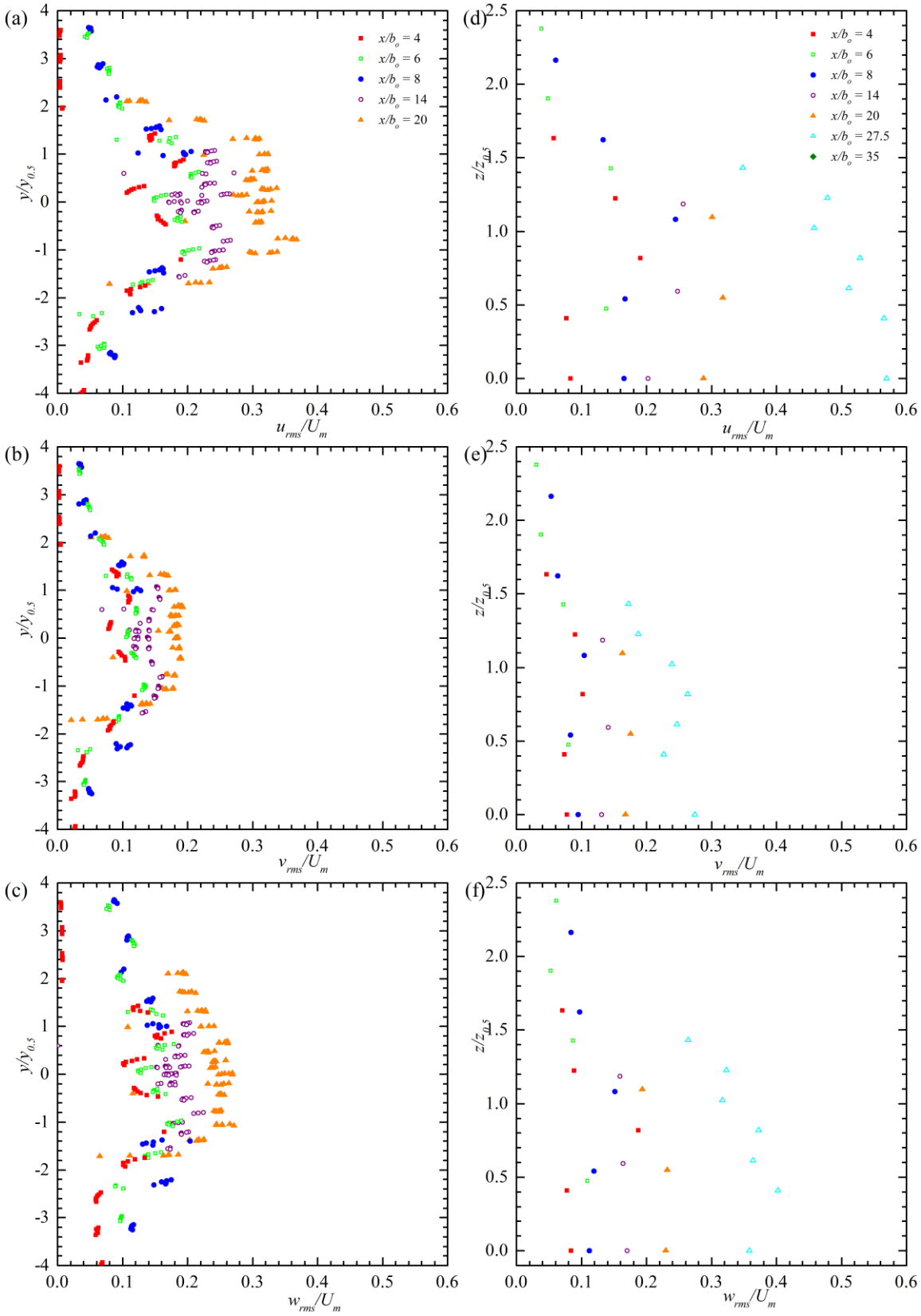

Figure 5-10 Profiles of turbulence intensities for tailwater level of 650 mm

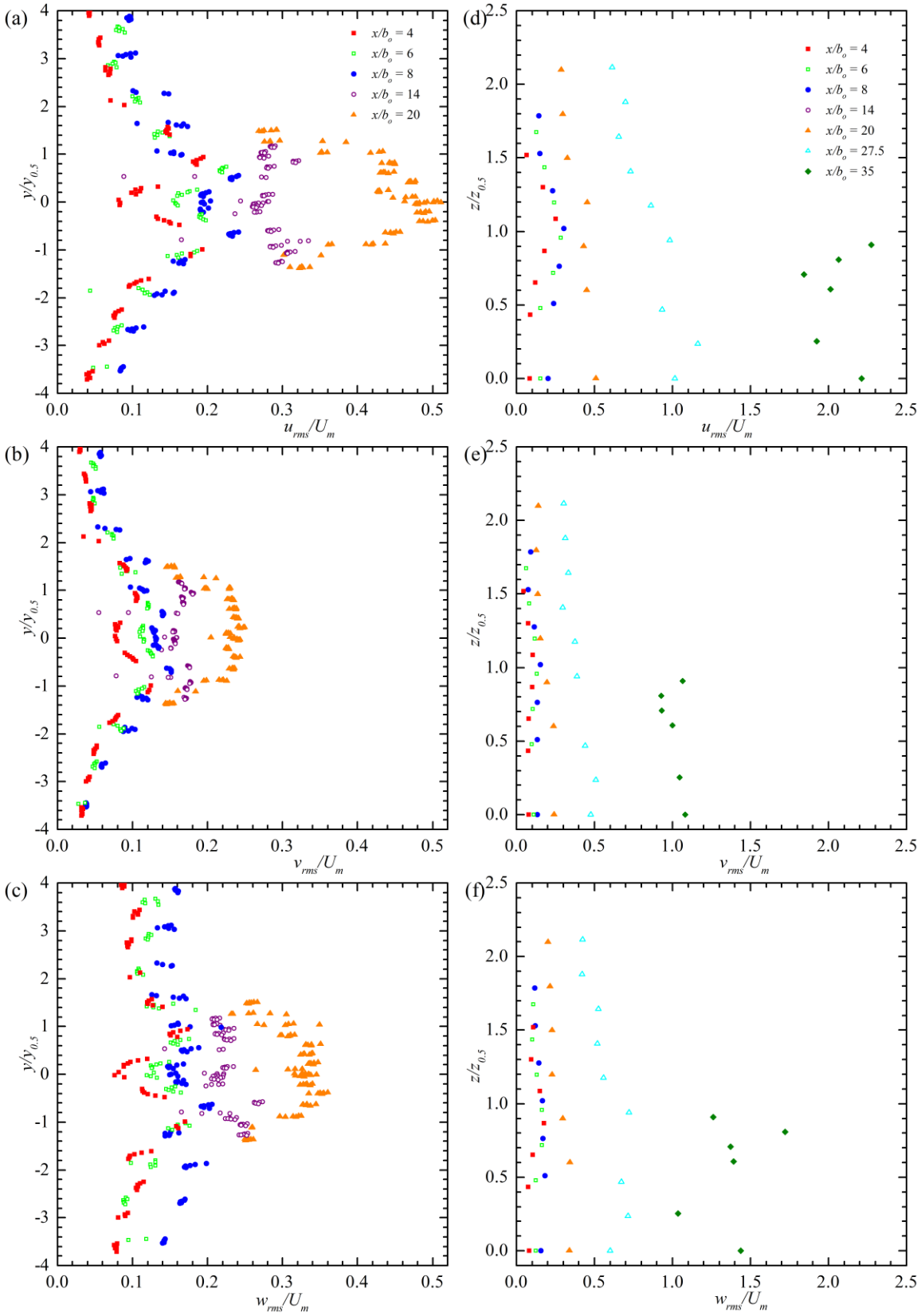

Figure 5-11 Profiles of turbulence intensities for tailwater level of 550 mm

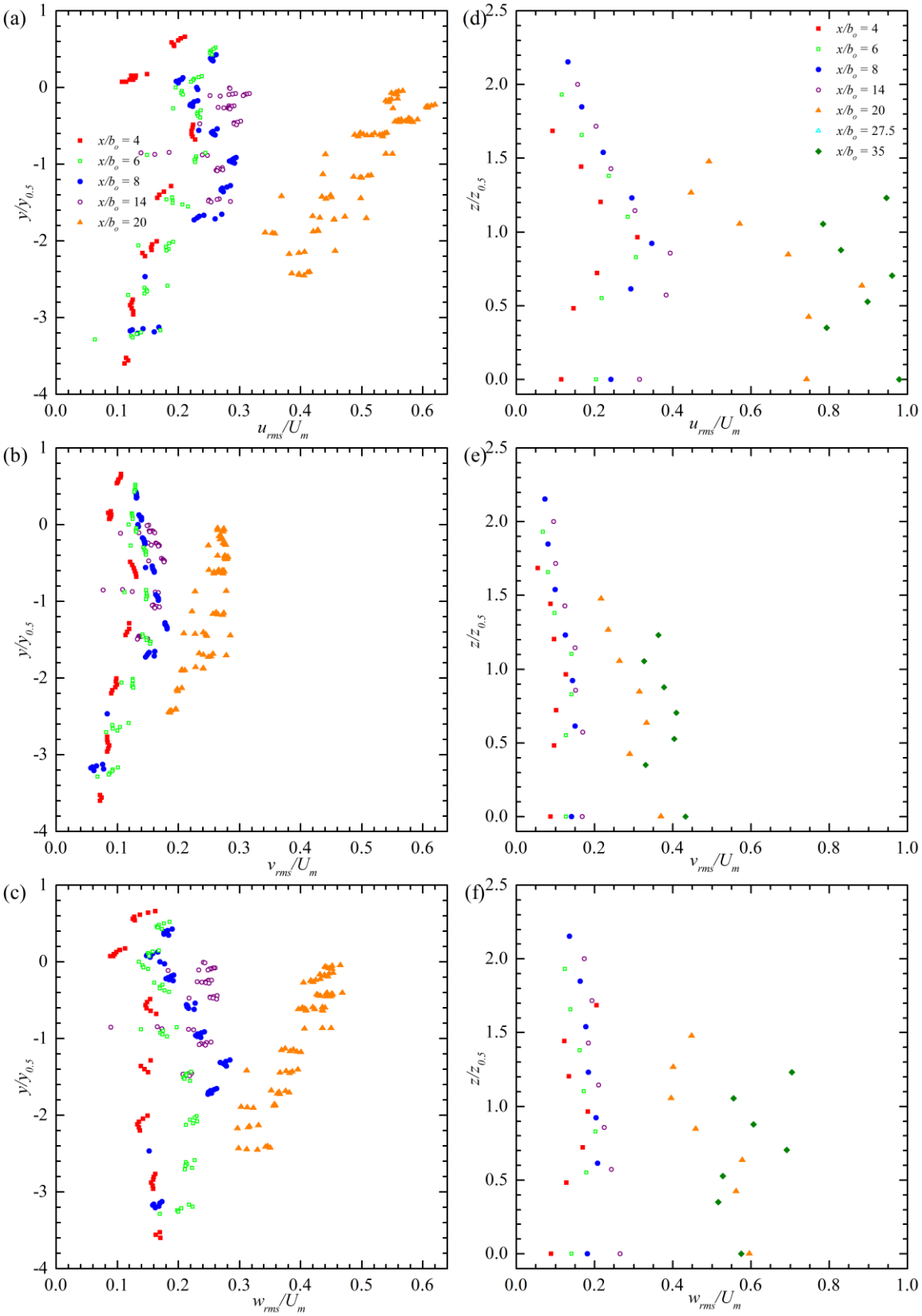

Figure 5-12 Profiles of turbulence Intensities for tailwater level of 350 mm

5.4 *Turbulent Kinetic Energy*

Profiles of turbulent kinetic energy, *k*, are shown in Figure 5-13 to Figure 5-16. Unlike many of the previous studies in which the turbulent kinetic energy, *k*, was estimated from two of the three components of turbulence intensity, the values of *k* presented in these plots are calculated using all three components of turbulence intensity as $k = 1/2\,(u_{rms}^2 + v_{rms}^2 + w_{rms}^2)$. The profiles of turbulent kinetic energy closely follow

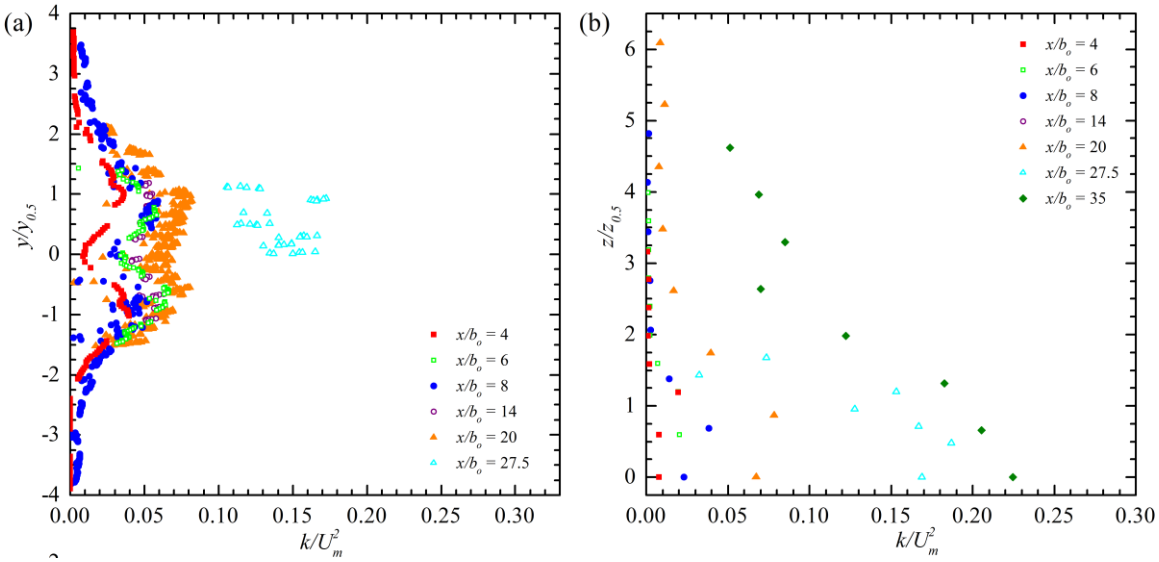

Figure 5-13 Turbulent kinetic energy for tailwater level of 750 mm (a) vertical profile, (b) lateral profile

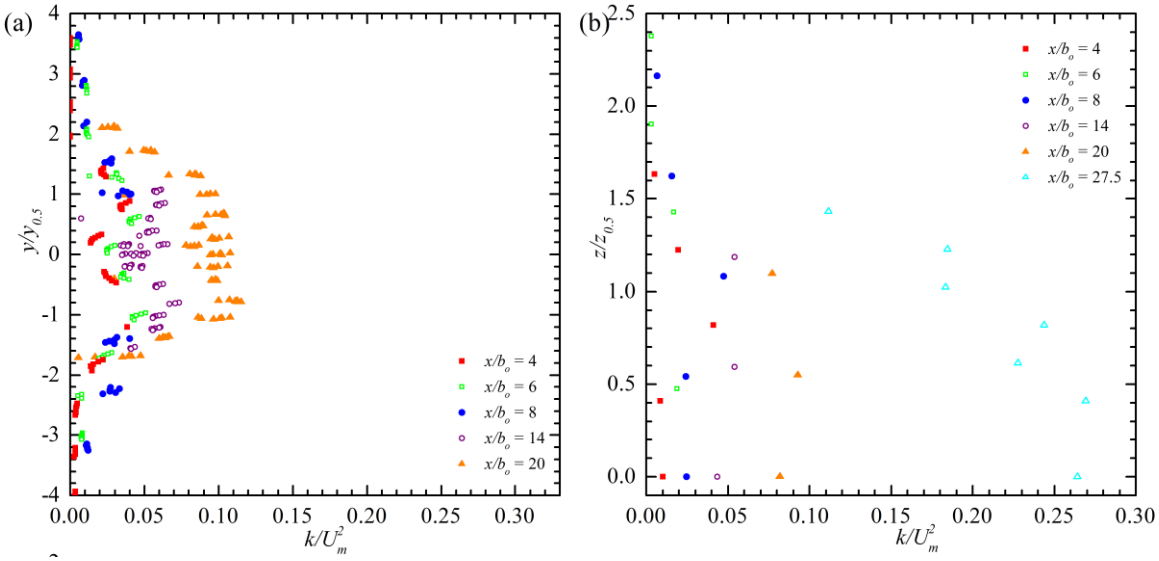

Figure 5-14 Turbulent kinetic energy for tailwater level of 650 mm (a) vertical profile (b) lateral profile

the trends seen in the turbulence intensities. They have a prominent double peak near the orifice that disappears with streamwise distance. The peaks are located near the jet half width in both vertical and lateral profiles. Profiles of normalized turbulent kinetic energy increase with streamwise distance. Similarly to the turbulence intensities, the normalized turbulent kinetic energy achieves higher magnitudes at lower tailwater levels. This indicates that a higher tailwater level decreases the turbulent kinetic energy in a jet.

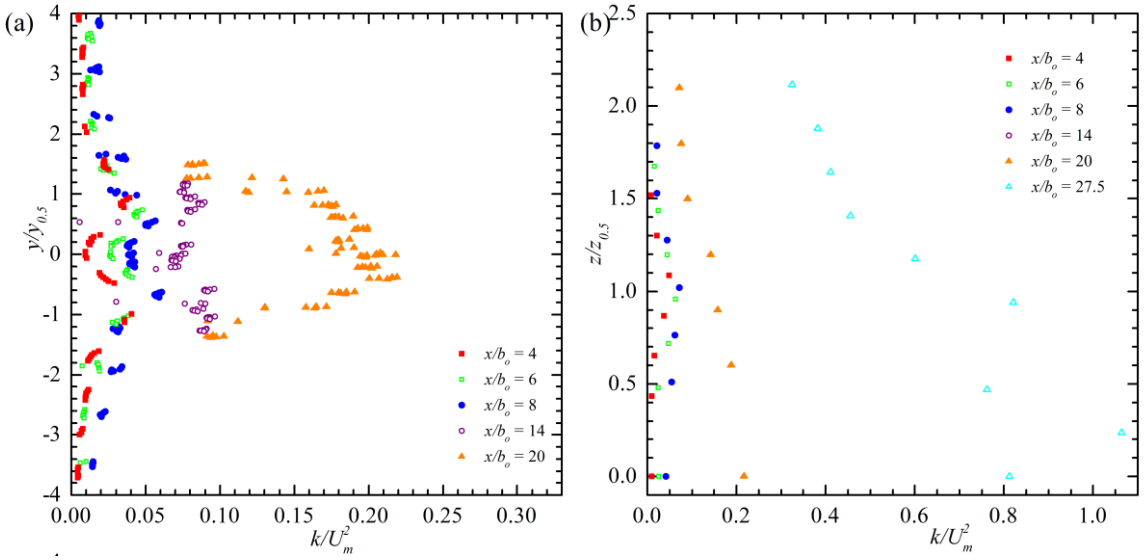

Figure 5-15 Turbulent kinetic energy for tailwater level of 550 mm (a) vertical profile (b) lateral profile

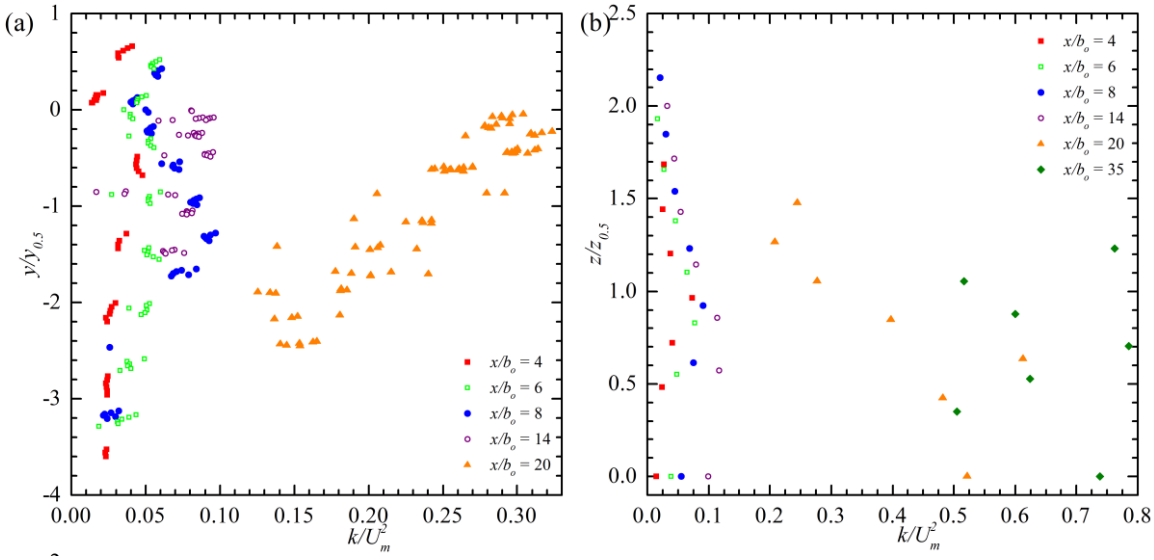

Figure 5-16 Turbulent kinetic energy for tailwater level of 350 mm (a) vertical profile (b) lateral profile

5.5 *Reynolds Shear Stresses*

The profiles of dimensionless Reynolds shear stresses, uv/U_m, uw/U_m, and vw/U_m, are plotted in Figure 5-17 to Figure 5-20. Figure 5-20 only shows a partial profile as it was not possible to measure the complete outer shear layer due to its proximity to the water surface. The collected data follows a similar trend as data collected at higher tailwater levels. The vertical profiles of Reynolds shear stress *uv* are antisymmetric with peaks located near the jet half width, $y_{0.5}$. The peak magnitude is seen to increase slightly with streamwise distance. This indicates that the Reynolds shear stress *uv* decays at a slightly slower rate than the squared local maximum streamwise mean velocity, U_m^2. By looking at vertical profiles of Reynolds shear stress *uv* it was confirmed that it does in fact decay with increasing streamwise distance. The magnitude of Reynolds shear stress *uv* does not significantly differ with changing tailwater levels.

The vertical profiles of Reynolds shear stress *uw* start equal to zero and increase in magnitude with increasing streamwise distance. At the highest tailwater level the profiles develop into an anti-symmetric shape while at lower tailwater levels no significant trend is noticeable. Vertical profiles of Reynolds shear stress *vw* stay near zero at all tailwater levels.

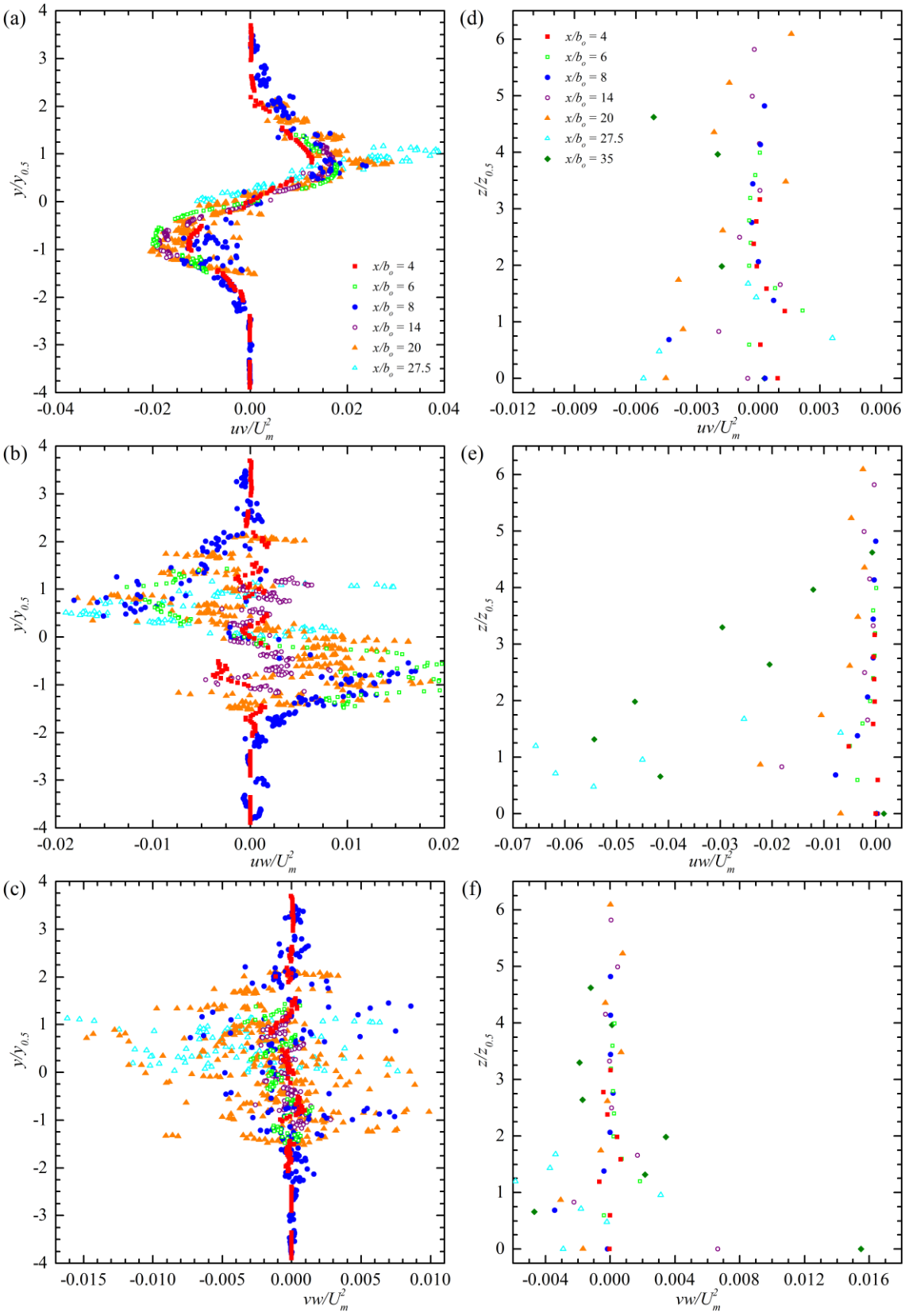

Figure 5-17 Profiles of Reynolds shear stresses for tailwater level of 750 mm

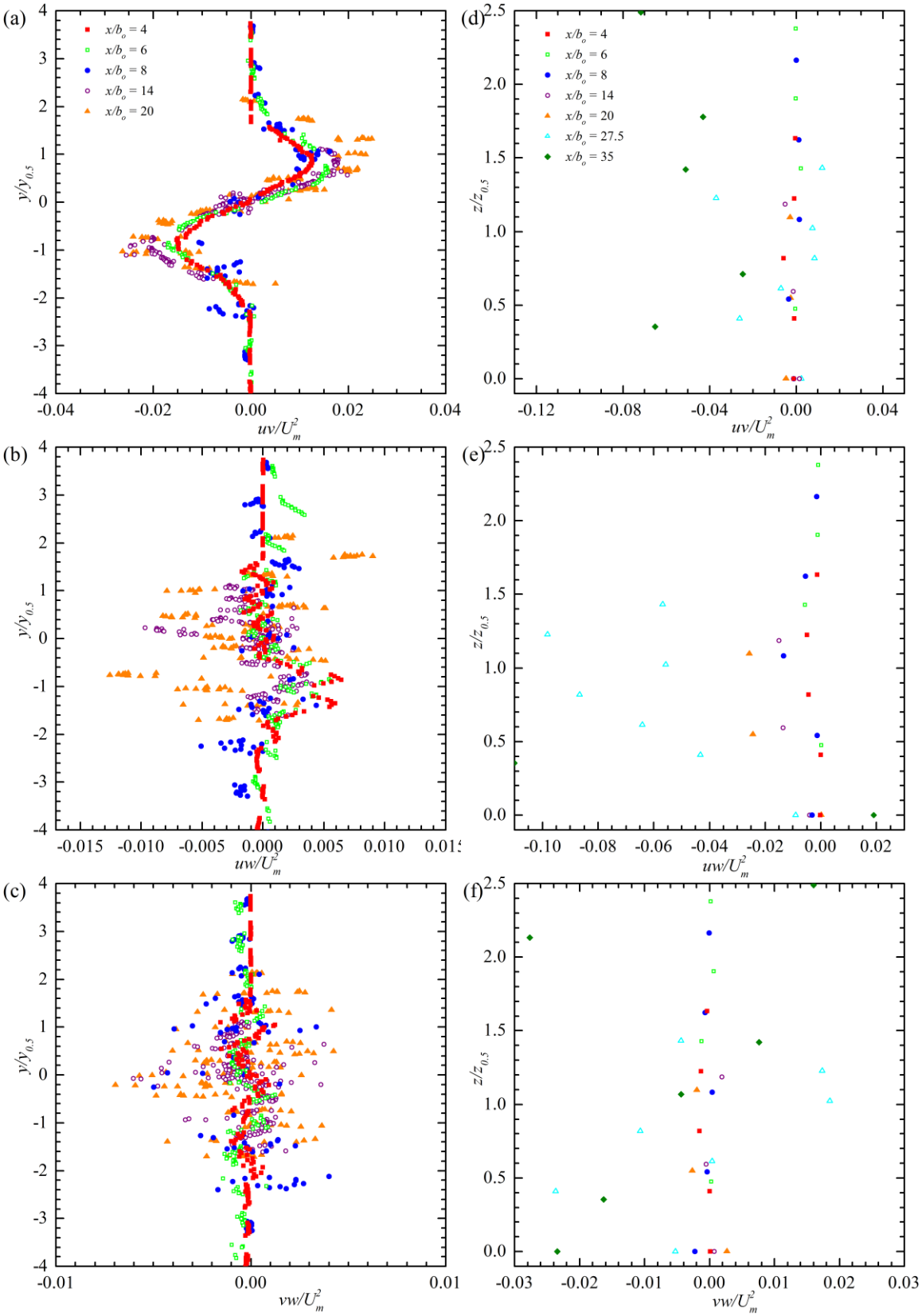

Figure 5-18 Profiles of Reynolds shear stresses for tailwater level of 650 mm

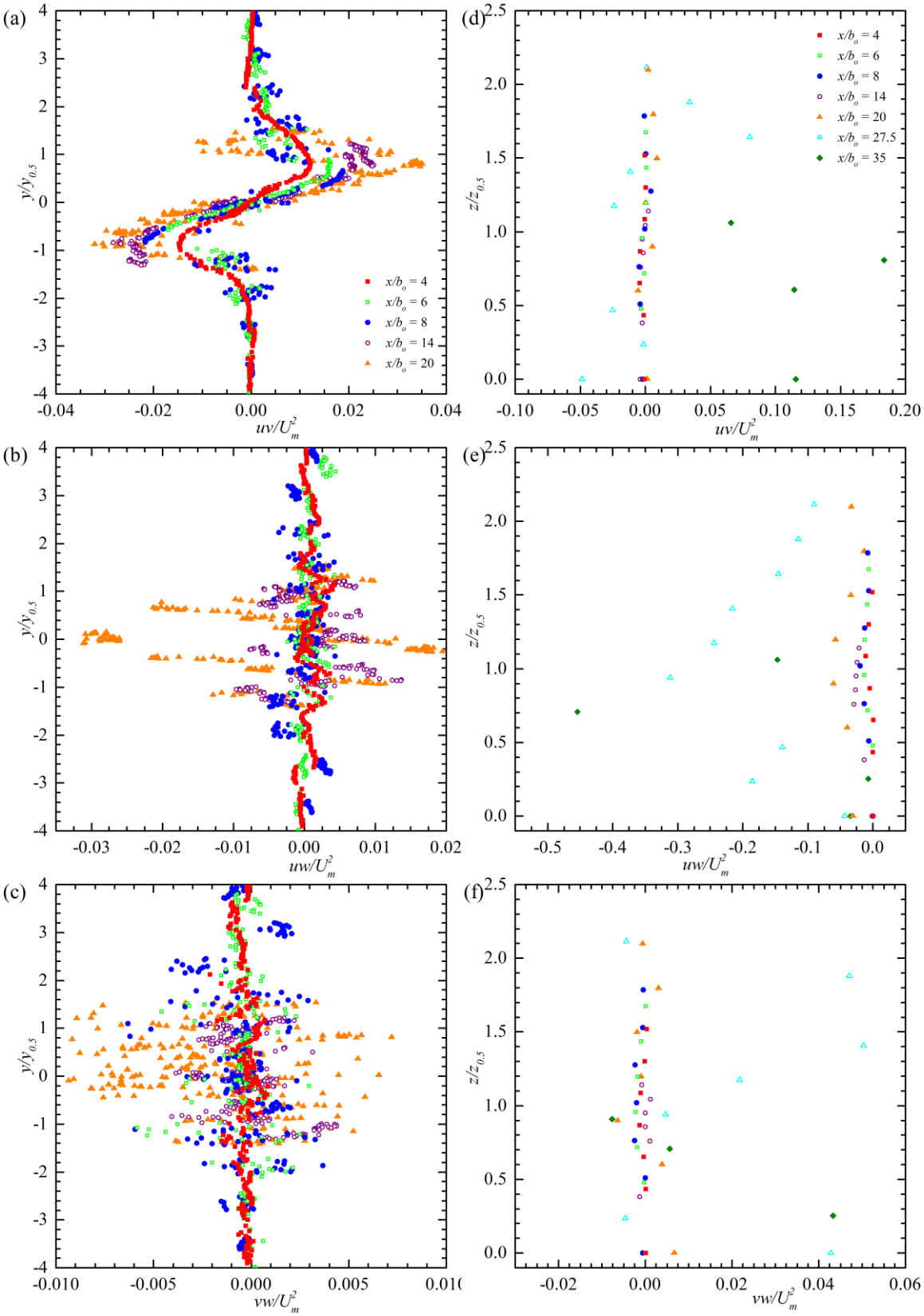

Figure 5-19 Profiles of Reynolds shear stresses for tailwater level of 550 mm

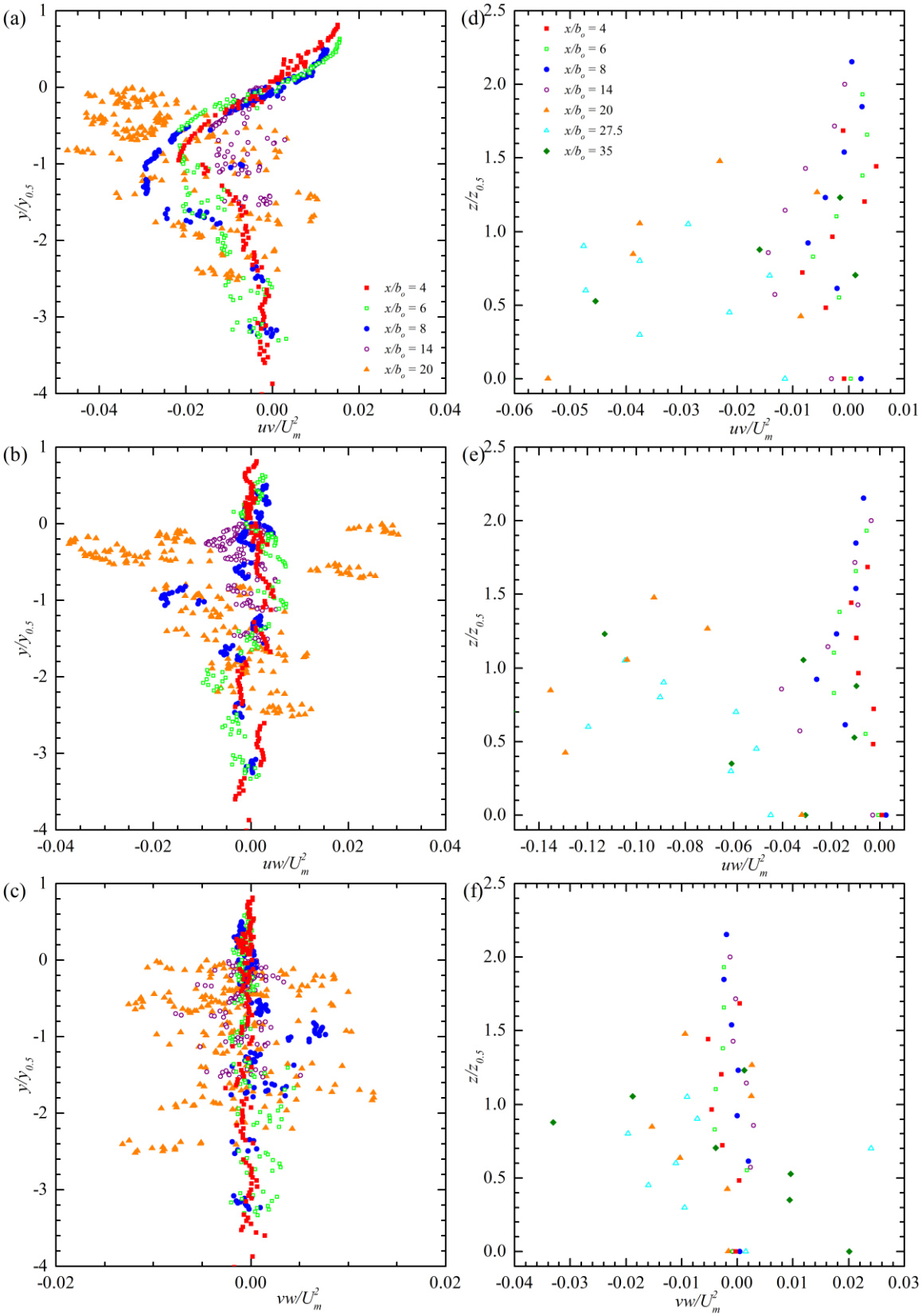

Figure 5-20 Profiles of Reynolds shear stresses for tailwater level of 350 mm

5.6 *Triple Velocity Correlations*

The triple velocity correlations, whose spatial gradients constitute the turbulence diffusion terms in the transport equations for the turbulent kinetic energy and Reynolds stresses, have never been reported in previous studies of offset jets. These turbulence statistics can provide insight into how turbulence is diffused throughout the jet. Since turbulence diffusion is one of the terms that require modelling, the distributions of the

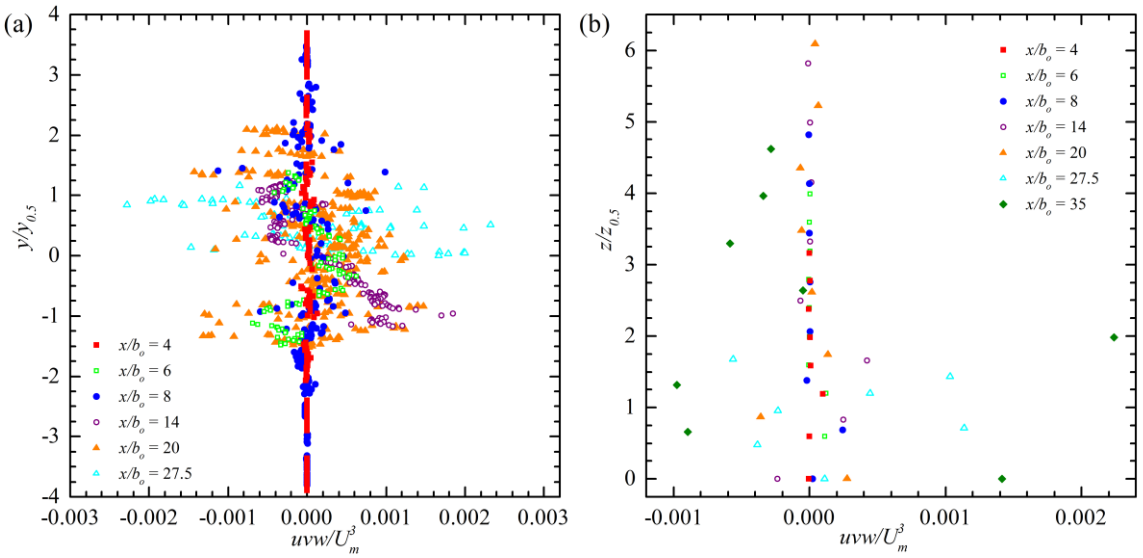

Figure 5-21 Triple velocity correlation for tailwater level of 750 mm (a) vertical profile (b) lateral profile

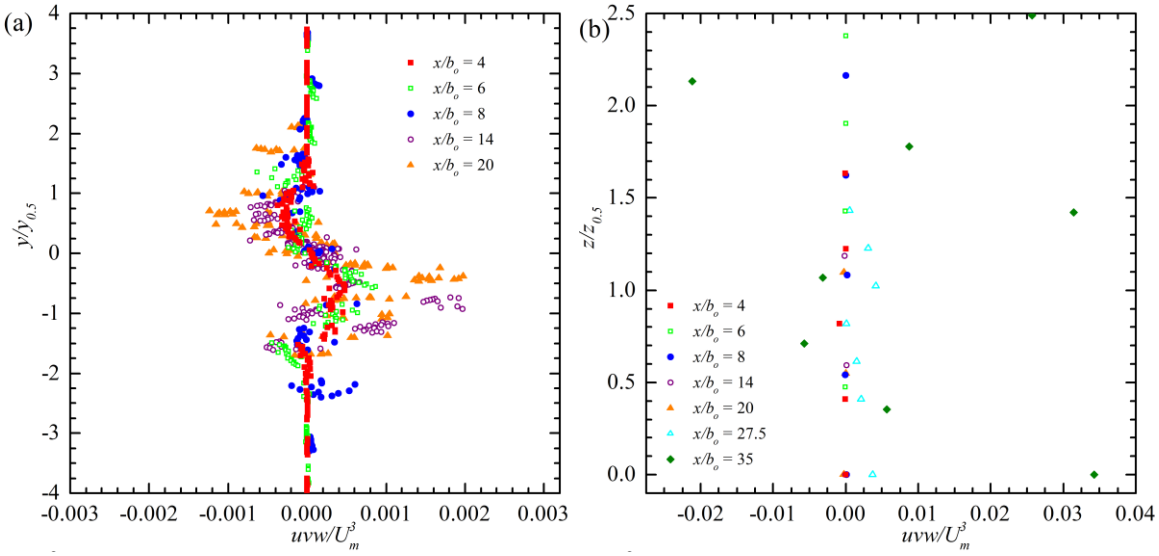

Figure 5-22 Triple velocity correlation for tailwater level of 650 mm (a) vertical profile (b) lateral profile

triple velocity correlations will provide a useful guide in developing reliable turbulence models. The triple velocity correlations *uvw* are plotted in Figure 5-21 to Figure 5-24. The profiles of *uvw* have an antisymmetric profile with a slight increase in magnitude with streamwise distance. The antisymmetric profile is not present at the highest tailwater level and becomes more pronounced with decreasing tailwater level. This indicates that the jet has higher diffusion of turbulence at lower tailwater levels.

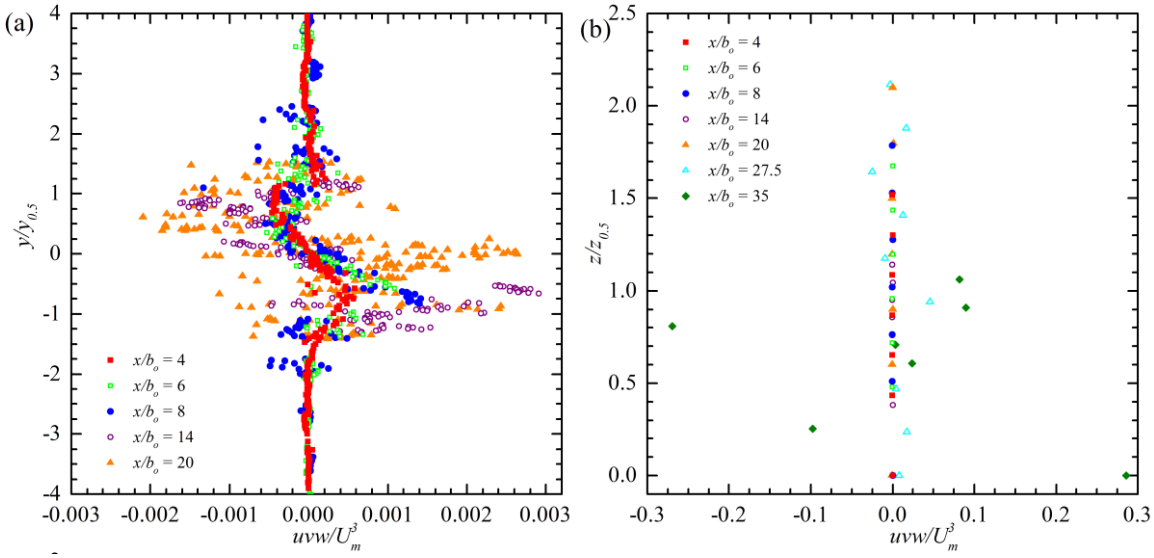

Figure 5-23 Triple velocity correlation for tailwater level of 550 mm (a) vertical profile (b) lateral profile

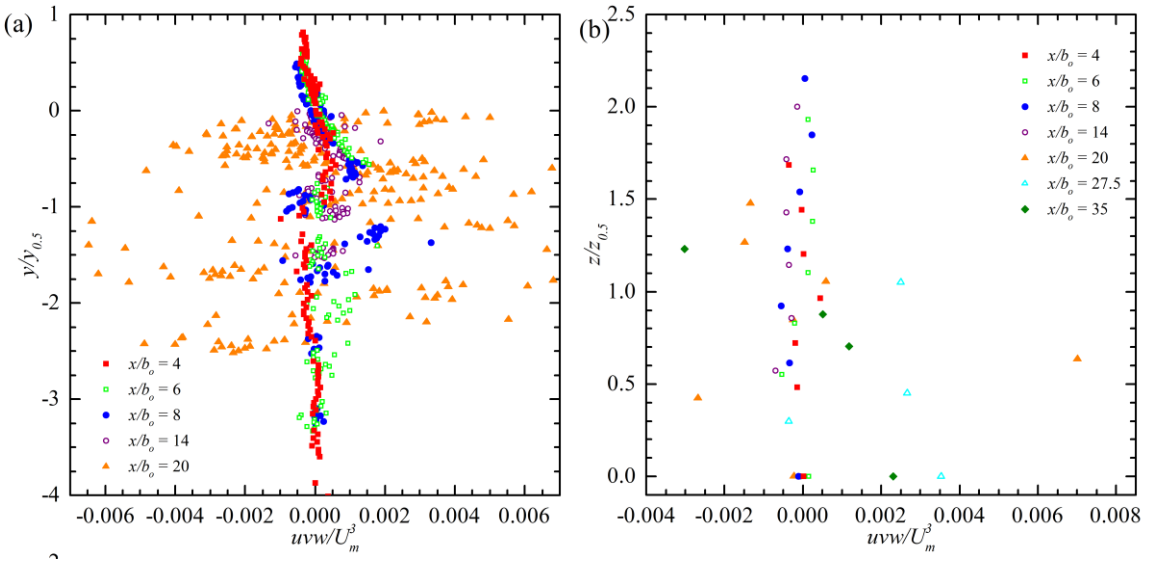

Figure 5-24 Triple velocity correlation for tailwater level of 350 mm (a) vertical profile (b) lateral profile

5.7 *Summary*

An experimental investigation of the tailwater level effects on three-dimensional offset jets has been conducted. An analysis of the effects of tailwater levels on streamwise flow development and profiles of mean velocity and turbulence statistics has been completed.

A jet will curve towards a solid boundary because of the Coanda effect, however, if the depth of water above the jet is small the jet will move towards the water surface instead. This different behavior has an effect on the decay and spread rate of the jet. When the jet reattaches to the solid boundary, the linear decay rate within the recirculation region, n_l, and the power decay rate within the wall jet region, n_p, increase with decreasing tailwater level. The vertical spread rates of a reattaching jet will not significantly differ with changing tailwater levels, however, the lateral spread rate before and after the inflection point, x_{vc}, will increase with decreasing tailwater level. The streamwise location of the inflection point will increase with increasing tailwater level.

The vertical profiles of streamwise mean velocity attained similarity and were decaying by $x/b_o = 4$. They showed recirculation zones in all shear layers. The recirculation zones were reduced at the lowest tailwater level. The vertical velocity, V, increases until the inflection point of lateral spread, x_{vc}, and subsequently decays. The lateral velocities, W, beyond $z/z_{0.5} = 1$ move towards the jet upstream of the inflection point and away from the jet downstream of the inflection point.

The profiles of turbulence intensities and turbulent kinetic energy featured a double peak near the jet half width which disappeared with streamwise distance. The magnitude of turbulence intensities and turbulent kinetic energy decreased with increasing tailwater.

The Reynolds shear stresses, *uv*, *uw*, and *vw*, are essential in turbulence models to simulate the production of turbulence. Triple velocity correlations terms are also important in turbulence models to simulate the diffusion of turbulence. The profiles of Reynolds shear stresses and triple velocity correlation collected in this study will aid in the calibration and validation of turbulence models to the particular flow conditions of offset jets. These distributions will also be useful for hydrotechnical engineers designing new or rehabilitating existing structures that have similar flow patterns as three-dimensional offset jets. The profiles of Reynolds shear stress *uv* displayed an antisymmetric shape with no significant changes with tailwater levels. The profiles of Reynolds shear stress *uw* initially started very low with no significant shape. At high tailwater levels the magnitude increased and developed into an antisymmetric shape while it did not at lower tailwater levels. Triple velocity correlation terms showed increased diffusion at lower tailwater levels.

CHAPTER 6: ASYMMETRY RATIO EXPERIMENTS

The effects of asymmetry ratio on three-dimensional offset jets are evaluated in this chapter. Five different asymmetry ratios were used in this set of experiments. They are outlined in Table 3-3. The effects of asymmetry ratio will first be evaluated on the streamwise flow development. This includes the vertical location of maximum velocity, y_m, the maximum streamwise mean velocity decay, n_l and n_p, and vertical and lateral spread rates, m, l_1, and l_2. The effects on profiles of mean velocities and turbulence statistics will follow.

6.1 *Streamwise Flow Development*

Figure 6-1 (a) shows the vertical location of maximum streamwise velocity, y_m. The jet curves towards the channel bottom due to the Coanda effect. The jet is seen to curve towards the channel bottom faster at the two highest asymmetry ratios while it is not significantly affected at the three lowest asymmetry ratios. This is also observed in the vector plot of the *xy*-plane seen in Figure 6-5 to Figure 6-9.

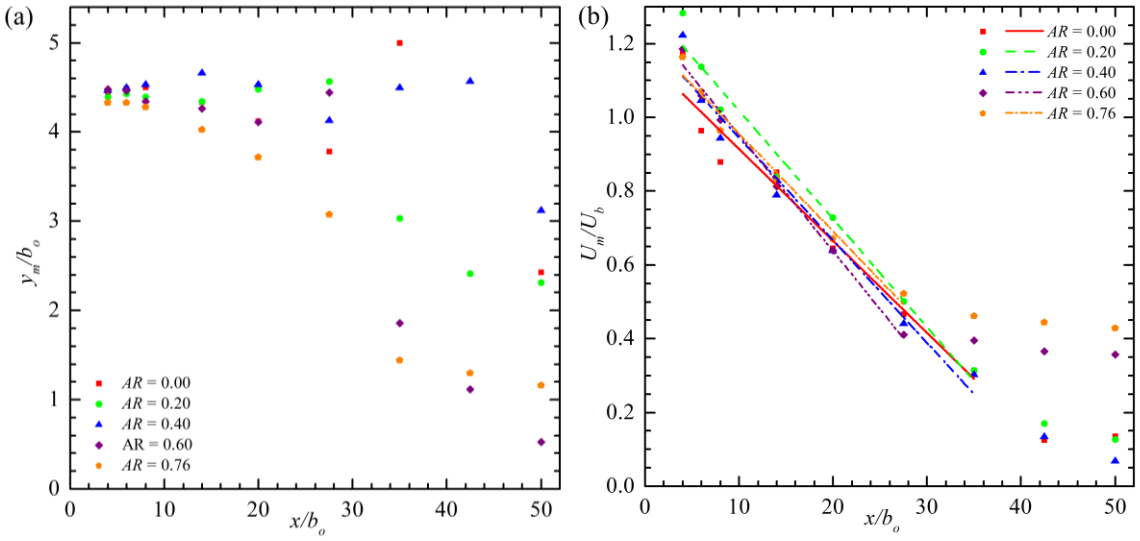

Figure 6-1 (a) Vertical location of maximum streamwise mean velocity (b) linear decay of maximum streamwise mean velocity

The local maximum mean streamwise velocities are shown in Figure 6-1 (b) with streamwise distance, x/b_o. The velocities can be seen to decrease with increasing streamwise distance. At the higher asymmetry ratios of 0.60 and 0.76 the decay rate of local maximum velocities reduces drastically at x/b_o = 27.5. This causes the velocities to only decay to 35-45% of the bulk velocity by x/b_o = 50 which is significantly higher than the 5-15% achieved at asymmetry ratios of 0.00, 0.20, and 0.40. Lines were fitted through the data to calculate the linear decay rates, n_l, and are summarized in Table 6-1. The linear decay was fitted to data points within $4 \leq x/b_o \leq 35$ for the three lowest asymmetry ratios, 0.00, 0.20, and 0.40, and $4 \leq x/b_o \leq 27.5$ for the higher asymmetry ratios of 0.60 and 0.76 because of the drastic change in decay rate. The linear decay rate increases with

Table 6-1 Linear decay rates of asymmetry experiments

Asymmetry ratio *AR* [-]	Decay rate n_l [-]	Virtual velocity U_v [-]	Adjusted R-squared
0.00	0.025	1.163	0.945
0.20	0.029	1.311	0.974
0.40	0.028	1.223	0.960
0.60	0.032	1.268	0.991
0.76	0.026	1.221	0.974

the asymmetry ratio, *AR*, however decreases at the maximum asymmetry ratio where the jet is constantly attached to the channel wall. The virtual velocity, U_v, does not significantly change with changing asymmetry ratios.

A curve of the form $U_m \propto x^{-n_p}$ was fitted to data points within the streamwise extent of $20 \leq x/b_o \leq 50$ and can be seen in Figure 6-2. The decay rates, n_p, can be seen in Table 6-2 along with the adjusted R-squared values. At the highest asymmetry ratios of 0.60 and 0.76 the decay rates, n_p, are reduced 57-70% when compared to the lower asymmetry ratios of 0.00, 0.20, and 0.40. The decay rates at the lower asymmetry ratios of 0.00, 0.20, and 0.40 are higher than the range of $1.15 \leq n_p \leq 1.20$ for three-dimensional offset jets previously reported by Davis and Winarto (1980) and Agelin-Chaab and Tachie (2011b). The higher decay rates are attributed to the channel turbulence levels and nozzle geometry used in this study which differed from previous studies. The decay rates for asymmetry ratios, *AR*, of 0.60 and 0.76 are less than what has previously been reported for three-dimensional offset jets and similar to 0.52 and 0.50 that has been reported for

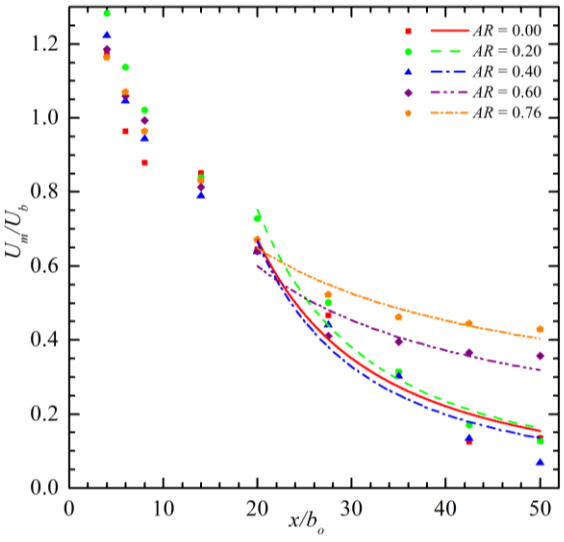

Figure 6-2 Power decay of maximum streamwise mean velocity within the wall jet region

two-dimensional offset jets by Bhuiyan et al. (2011) and Ead and Rajaratnam (2001), respectively. The vertical profiles in Figure 6-8 and Figure 6-9 show that the jet has spread to a near uniform velocity for a large vertical distance by the streamwise distance of x = 1650 mm or in dimensionless format x/b_o = 27.5. The lateral profiles show the jet to have significantly moved towards, and likely reattached, to the channel wall. These flow characteristics are similar to that of a two-dimensional offset jet and hence explain the similarity in decay rate.

Table 6-2 Power law decay rates of asymmetry experiments

Asymmetry ratio AR [-]	Decay rate n_p [-]	Adjusted R-squared
0.00	1.603	0.916
0.20	1.680	0.959
0.40	1.742	0.917
0.60	0.692	0.799
0.76	0.520	0.915

The vertical jet half width $y^+_{0.5}$ and $y^-_{0.5}$ are shown in Figure 6-3 with streamwise distance, x/b_o. The jet half widths in both outer and inner shear layers increase with increasing streamwise distance, an indication that the jet is entraining the surrounding

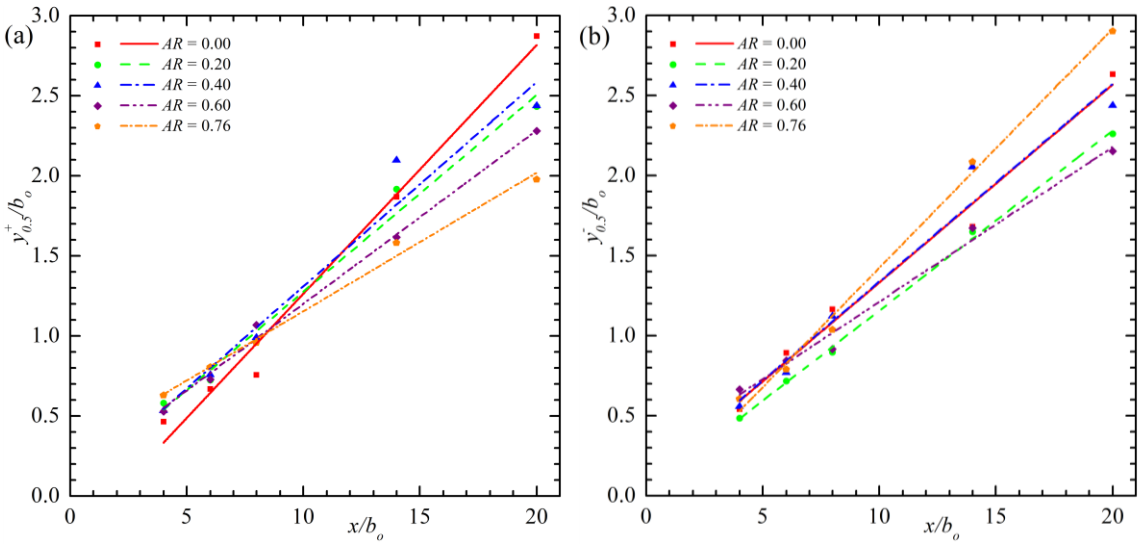

Figure 6-3 Vertical spread rate of asymmetry experiment in (a) outer shear layer and (b) inner shear layer

fluid. A line was fitted to the jet half width to calculate the spread rate, *m*. The results are shown in Table 6-3. The spread rate in the outer shear layer is seen to decrease with increasing asymmetry ratio. Typically the decay rate and spread rate would be proportional to each other. This is not the case in this experiment as the spread rates decrease with increasing decay rate. The spread rate in the inner shear layer does not follow a significant trend with changing asymmetry ratio.

Table 6-3 Vertical spread rate of asymmetry experiments

	Asymmetry ratio *AR* [-]	Spread rate *m* [-]	Virtual origin x_o [-]	Adjusted R-squared
$y^+_{0.5}$	0.00	0.155	1.856	0.981
	0.20	0.123	-0.404	0.982
	0.40	0.128	-0.273	0.952
	0.60	0.108	-1.083	0.994
	0.76	0.086	-3.355	0.991
$y^-_{0.5}$	0.00	0.123	-0.787	0.982
	0.20	0.112	-0.273	0.998
	0.40	0.123	-0.835	0.962
	0.60	0.097	-2.553	0.985
	0.76	0.149	0.453	0.993

The lateral jet half widths were calculated from lateral profiles measured at the vertical location of, y_m. They are shown in Figure 6-4 for both positive and negative horizontal shear layers. The jet half width initially decreases due to the vena contracta effect, then increases. A quadratic equation of the form $(z_{0.5}/b_o) = 3 - l_1(x/b_o) + l_2(x/b_o)^2$ was fitted to the jet width data to evaluate the lateral spread. The coefficients of lateral spreading, l_1 ans l_2, and adjusted R-squared values are shown in Table 6-4. The inflection points, the location where the lateral spreading changes from decreasing to increasing, were calculated from the fitted curves and are also shown in Table 6-4. The effects of the vena contracta are noticeably different between the positive and negative shear layers. In the positive shear layer, the side closest to the wall, the minimum half width increases with

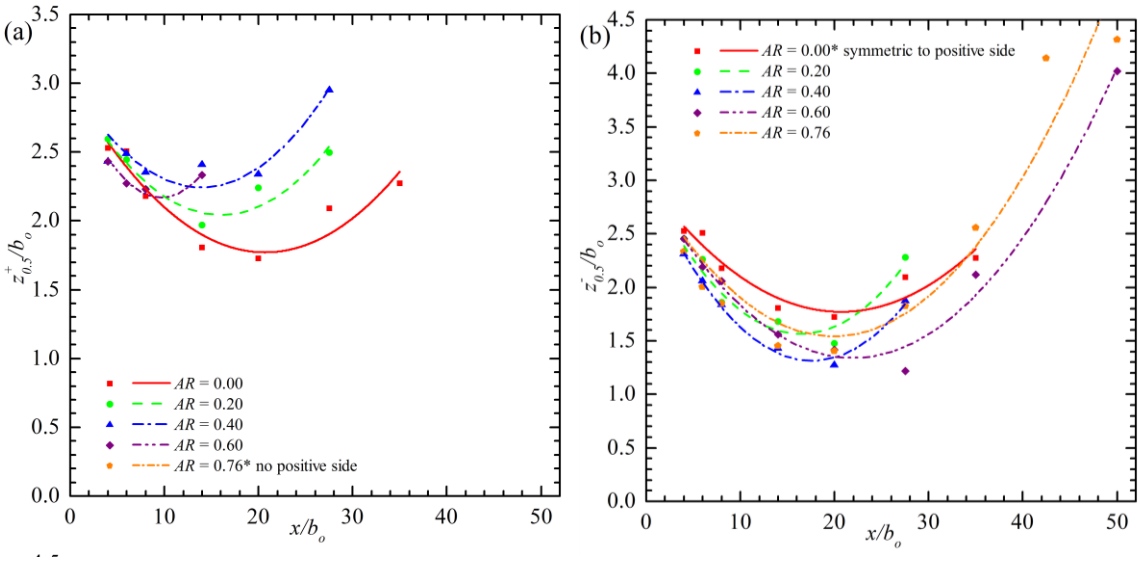

Figure 6-4 Lateral spread rate of tailwater experiment in (a) positive shear layer and (b) negative shear layer

increasing asymmetry ratio. The opposite is true for the negative shear layer where the minimum half width decreases with increasing asymmetry ratio. This indicates that the jet is shifting away from the center line of the orifice towards the channel wall. This is also observed in the vector plots of Figure 6-5 to Figure 6-9. The coefficient of lateral spreading l_2 in the positive shear layer increases with increasing asymmetry ratio. In the negative shear layer the coefficient of lateral spreading l_2 increased at asymmetry ratios of 0.20 and 0.40 and decreased at asymmetry ratios of 0.60 and 0.76. The differences at higher asymmetry ratios can be attributed to the jet having reattached to the channel wall. In the positive shear layer the inflection point decreases with increasing asymmetry ratio. In the negative shear layer the inflection point is reduced at asymmetry ratios of 0.20 and 0.40, and increased at asymmetry ratio of 0.60. At the asymmetry ratio of 0.76 it is not significantly affected.

Table 6-4 Coefficients of lateral spreading and inflection points of asymmetry experiments

	Asymmetry ratio *AR* [-]	Coefficients of lateral spreading l_1 [-]	l_2 [-]	Adjusted R-squared	Inflection point x_{vc}/b_o [-]
$z_{0.5}^{+}$	0.00	0.119	0.0029	0.997	20.69
	0.20	0.120	0.0037	0.999	15.99
	0.40	0.108	0.0039	0.997	13.94
	0.60	0.172	0.0089	0.999	9.65
	0.76	-	-	-	-
$z_{0.5}^{-}$	0.00	0.119	0.0029	0.997	20.69
	0.20	0.175	0.0053	0.996	16.43
	0.40	0.191	0.0054	0.999	17.62
	0.60	0.151	0.0034	0.997	21.95
	0.76	0.147	0.0037	0.978	19.89

6.2 *Vector Plots*

This section displays vector plots of vertical and horizontal velocity profiles. The vertical profiles were taken at the orifice centerline, $z = b'$. The lateral profiles were taken at the vertical location of local maximum streamwise mean velocity, $y = y_m$.

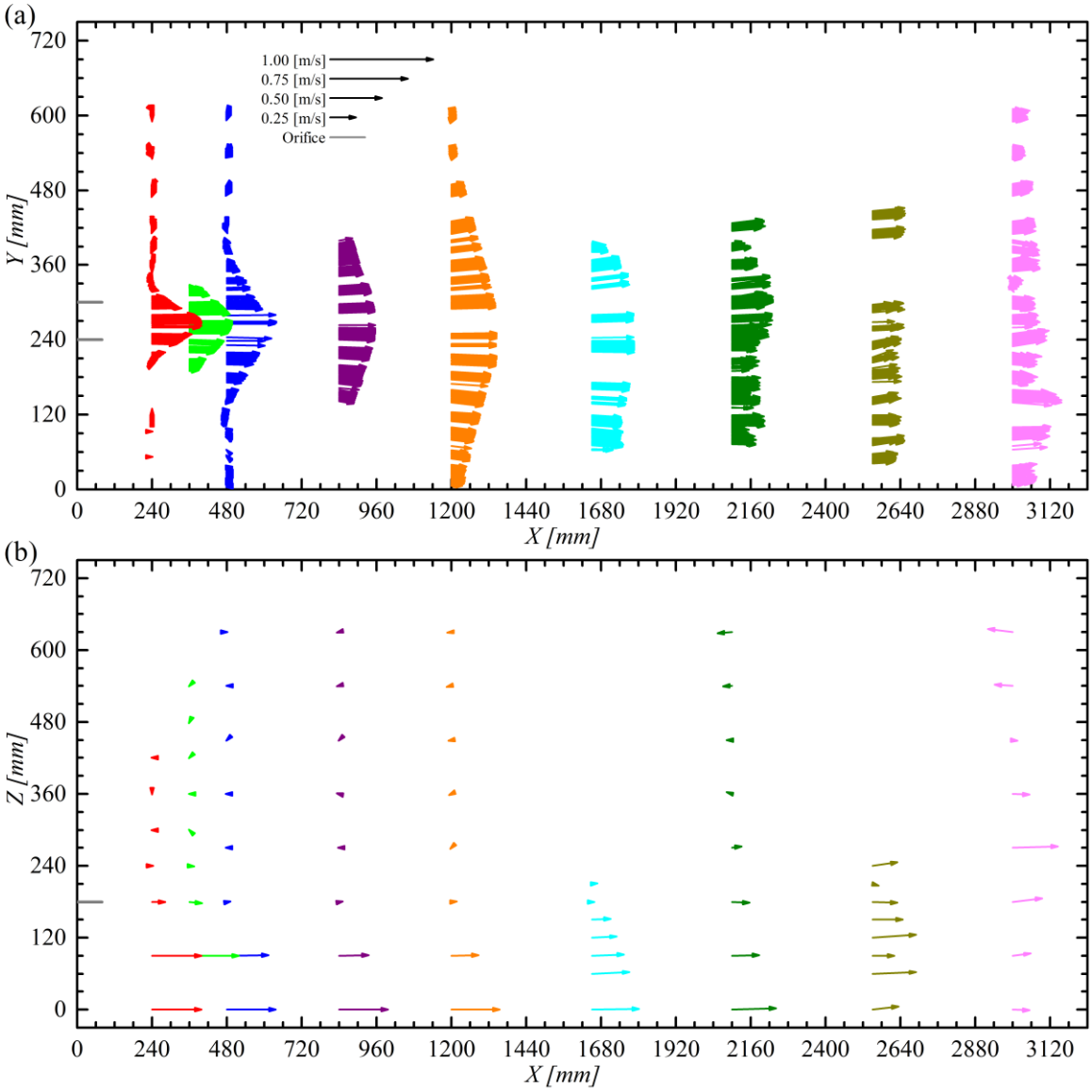

Figure 6-5 Vector plot for asymmetry ratio of 0.00 in (a) *xy*-plane and (b) *xz*-plane

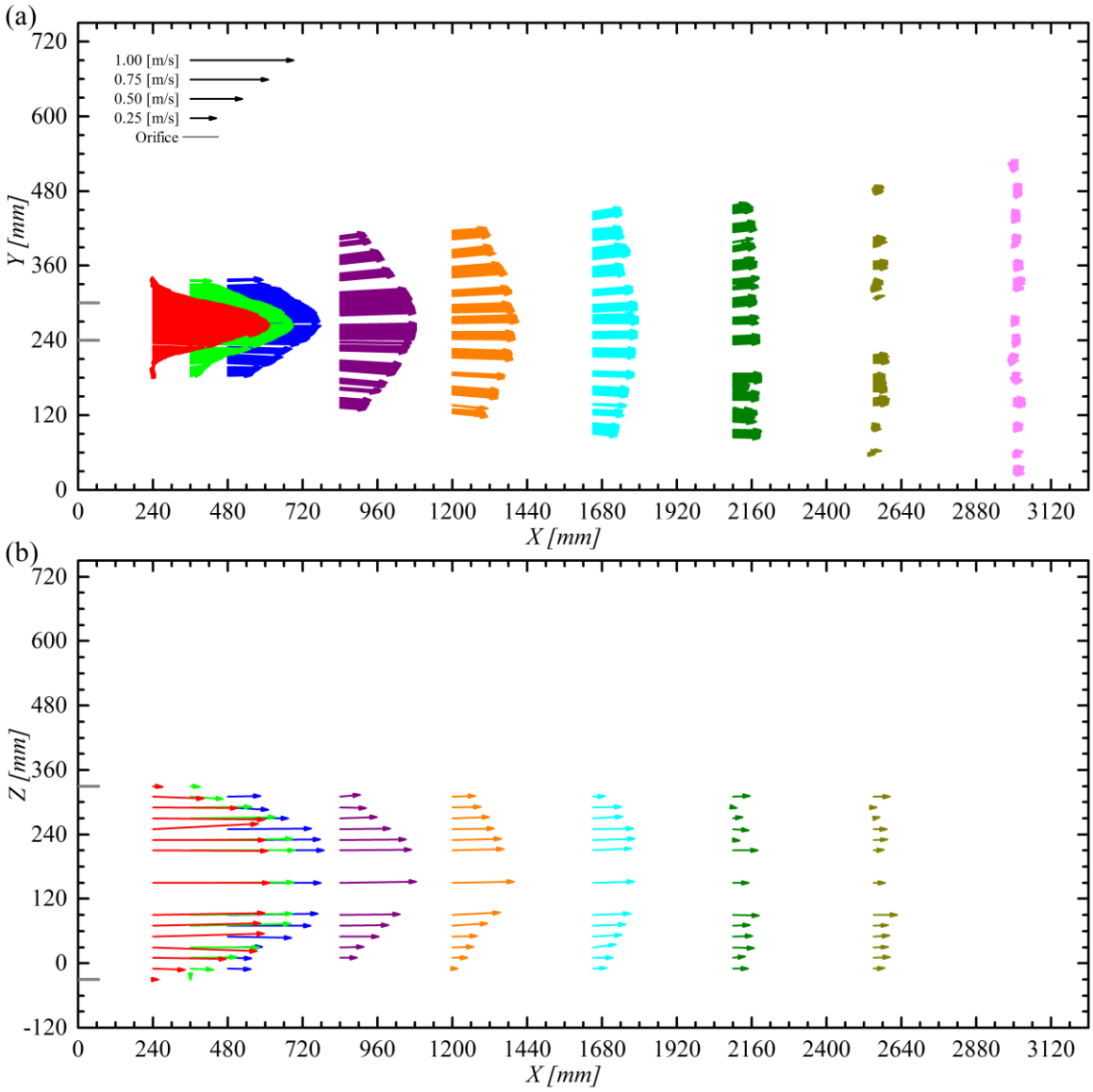

Figure 6-6 Vector plot for asymmetry ratio of 0.20 in (a) *xy*-plane and (b) *xz*-plane

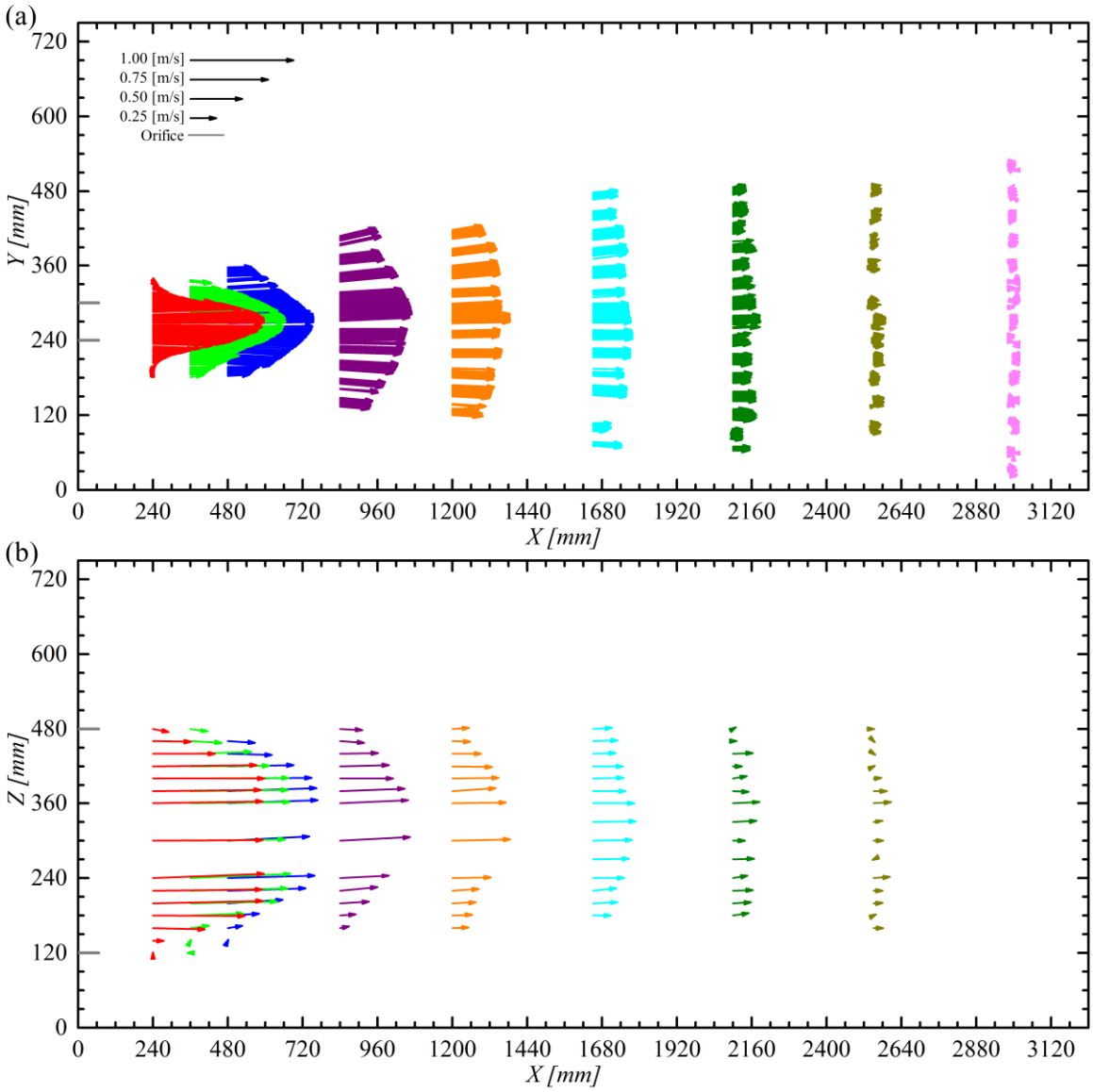

Figure 6-7 Vector plot for asymmetry ratio of 0.40 in (a) *xy*-plane and (b) *xz*-plane

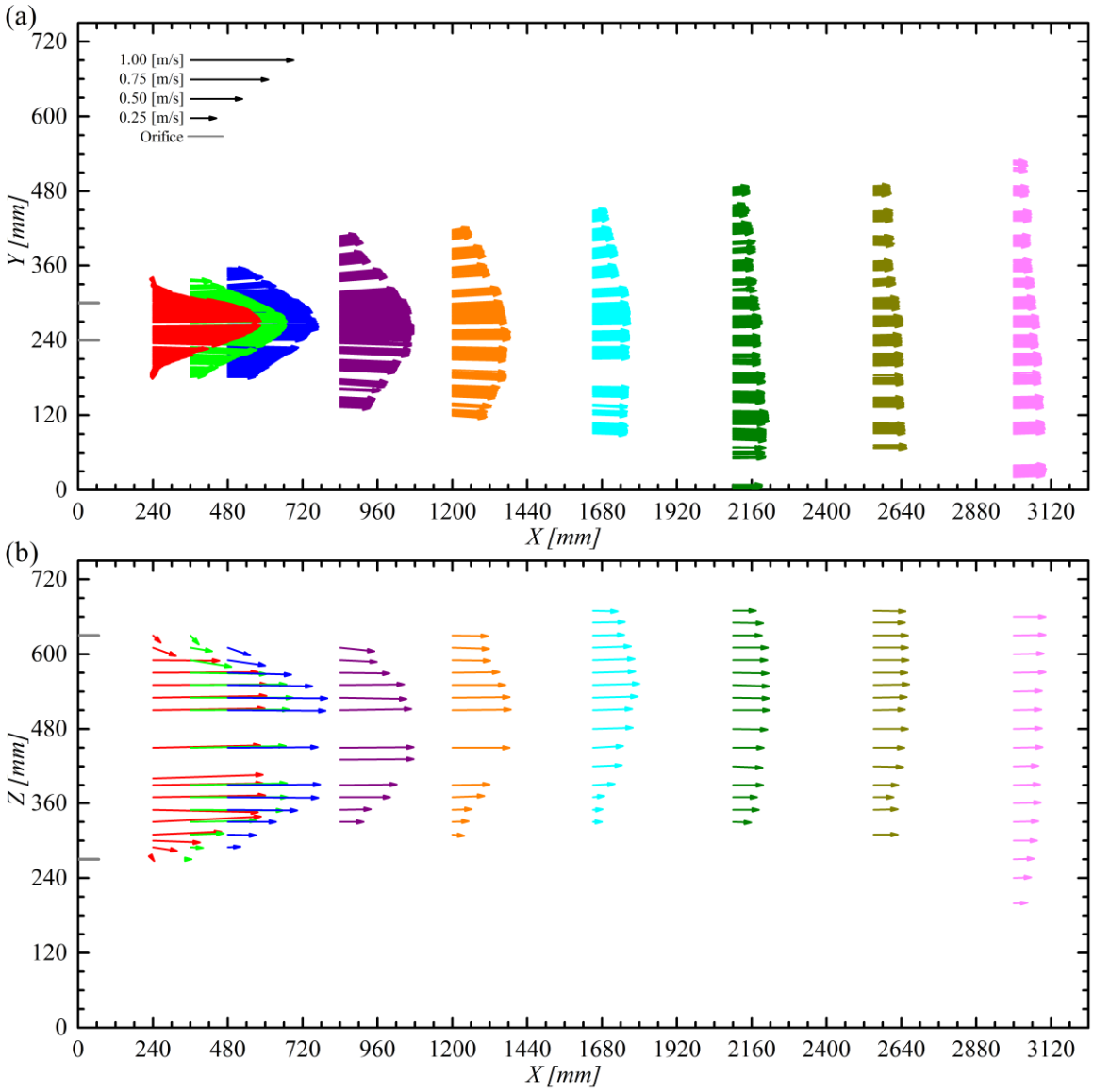

Figure 6-8 Vector plot for asymmetry ratio of 0.60 in (a) *xy*-plane and (b) *xz*-plane

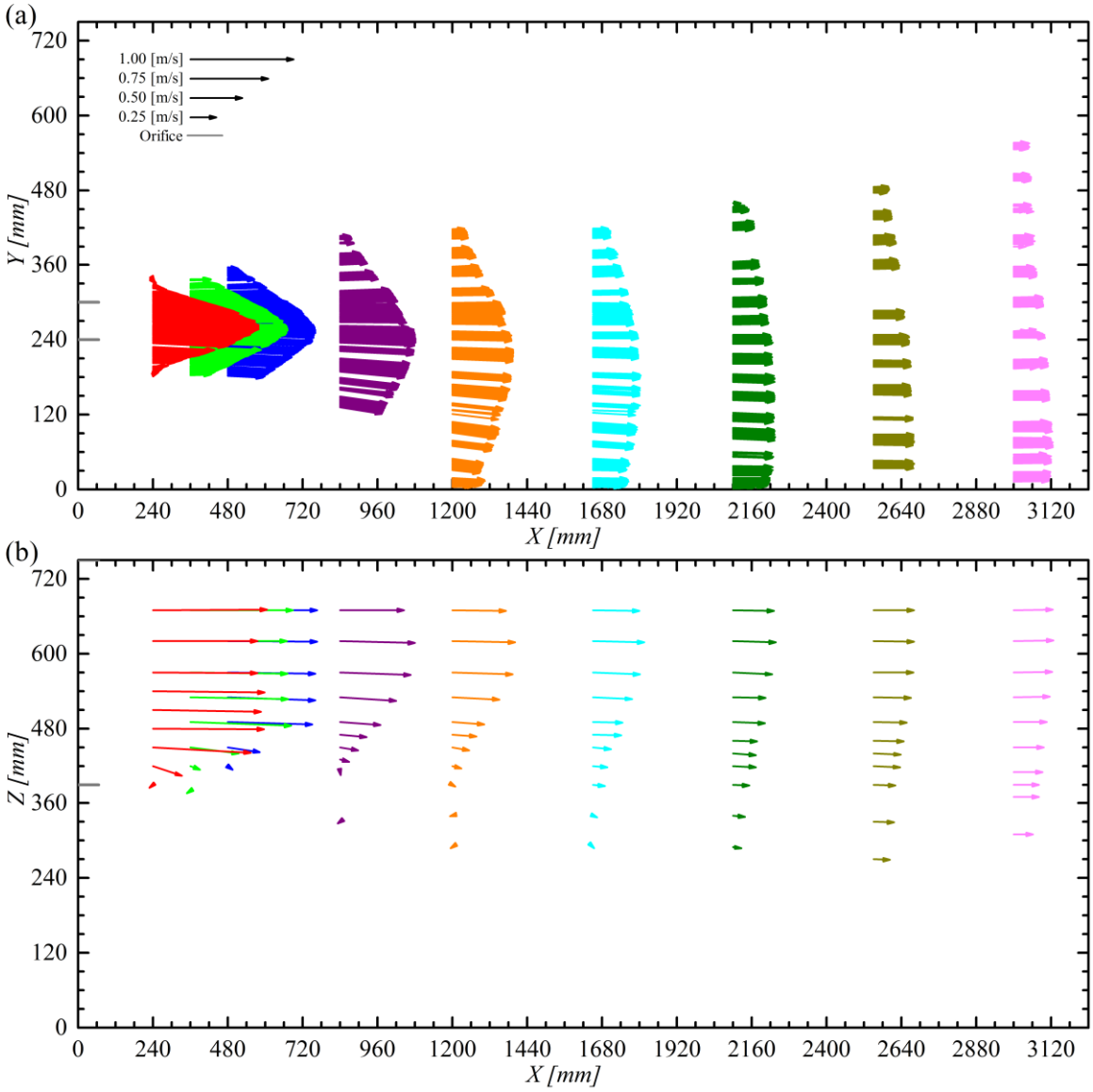

Figure 6-9 Vector plot for asymmetry ratio of 0.76 in (a) *xy*-plane and (b) *xz*-plane

6.3 *Mean Velocities*

Figure 6-10 to Figure 6-14 show vertical and lateral profiles of streamwise, vertical, and lateral velocities. The velocities were normalized by the local maximum streamwise velocity, U_m. The y and z coordinates were centered on the vertical location of maximum streamwise velocity, y_m, and orifice centerline, b', respectively, and normalized by the jet half width, $y_{0.5}$ and $z_{0.5}$, respectively.

The vertical profiles of normalized streamwise velocity, U/U_m, are seen to collapse well onto each other for all shown streamwise distances. Jets at all asymmetry ratios achieve self-similarity by the streamwise distance of $x/b_o = 4$. The velocities are positive within the vertical distance of $y/y_{0.5} = \pm 2$. Recirculation zones beyond $y/y_{0.5} = \pm 2$ are seen in Figure 6-10 (a) for asymmetry ratio of 0.00. The sampled vertical extent for all other asymmetry ratios did not extend into the recirculation zone, however, it is expected that the same recirculation zone is present beyond $y/y_{0.5} = \pm 2$ as the profiles are very similar to that of asymmetry ratio of 0.00.

The vertical profiles of normalized vertical velocity, V/U_m, display an antisymmetric shape. Peaks of outwards velocities are located near the jet half width, $y_{0.5}$, where outward spreading occurs. As you move away from the jet the velocities reverse towards the jet indicating entrainment. At the streamwise location of $x/b_o = 14$ the magnitude of the peaks located near the jet half width significantly increase for both shear layers at asymmetry ratios of 0.00 and 0.20, the outer shear layer at asymmetry ratio of 0.40, and inner shear layer at asymmetry ratio of 0.76. When looking at profiles of vertical velocity, V, not shown, the vertical velocity increases with streamwise distance for these specified regions. The vertical velocity remains relatively constant for both shear layers

at asymmetry ratio of 0.60, the inner shear layer at asymmetry ratio of 0.40, and the outer shear layer at asymmetry ratio of 0.76. At the highest asymmetry ratio profiles of vertical velocity skews towards the negative with increasing streamwise distance. The vertical velocity decreases with streamwise distance at the location of maximum streamwise velocity, y_m. For all other asymmetry ratios the vertical velocity stays near zero. This occurs because the Coanda effect forces the jet towards the channel bottom.

No significant trend is seen in the vertical profiles of normalized lateral velocity, W/U_m. The lateral velocities are equal to zero. This is expected as the measurements were taken in the symmetry plane.

The lateral profiles of normalized streamwise mean velocity, U/U_m, at the first cross section show a core region of near constant velocity with a sharp drop at the edges. With increasing streamwise distance the sharp edges of the core region become less pronounced and the profiles take a shape similar to a Gaussian distribution. In the negative shear layer, the side furthest from a wall, the velocities beyond the jet half width, $z_{0.5} = 1$, are increasing with the asymmetry ratio. As the jet moves towards the channel wall it leaves behind a region of low velocities.

The lateral profiles of normalized vertical velocity, V/U_m, do not show a trend and are equal to zero. This was expected as the profiles are located at the vertical location of maximum streamwise velocity, y_m, where the shear stress is zero.

Lateral profiles of normalized lateral mean velocities, W/U_m, for asymmetry ratios of 0.00 and 0.76 only show one side of the jet. For asymmetry ratio of 0.00 the negative side is equal and opposite to the positive side because of symmetry. At the asymmetry ratio of

0.76 the positive side does not exist because the orifice and jet are attached to the channel wall. Magnitudes and direction of lateral velocities are seen to differ between both shear layers. Stronger positive magnitudes are seen in the positive shear layer and are seen to increase with asymmetry ratio, *AR*. In the negative shear layer the velocities start negative at asymmetry ratio of 0.00 and increase to positive values at the highest asymmetry ratio of 0.76. With increased asymmetry ratio, *AR*, the distance between the jet and wall is reduced. This increases the Coanda effect which causes the lateral velocities to increase and the jet to curve towards the wall. Figure 6-5 to Figure 6-9 clearly show the jet curving towards the wall at increased asymmetry ratios.

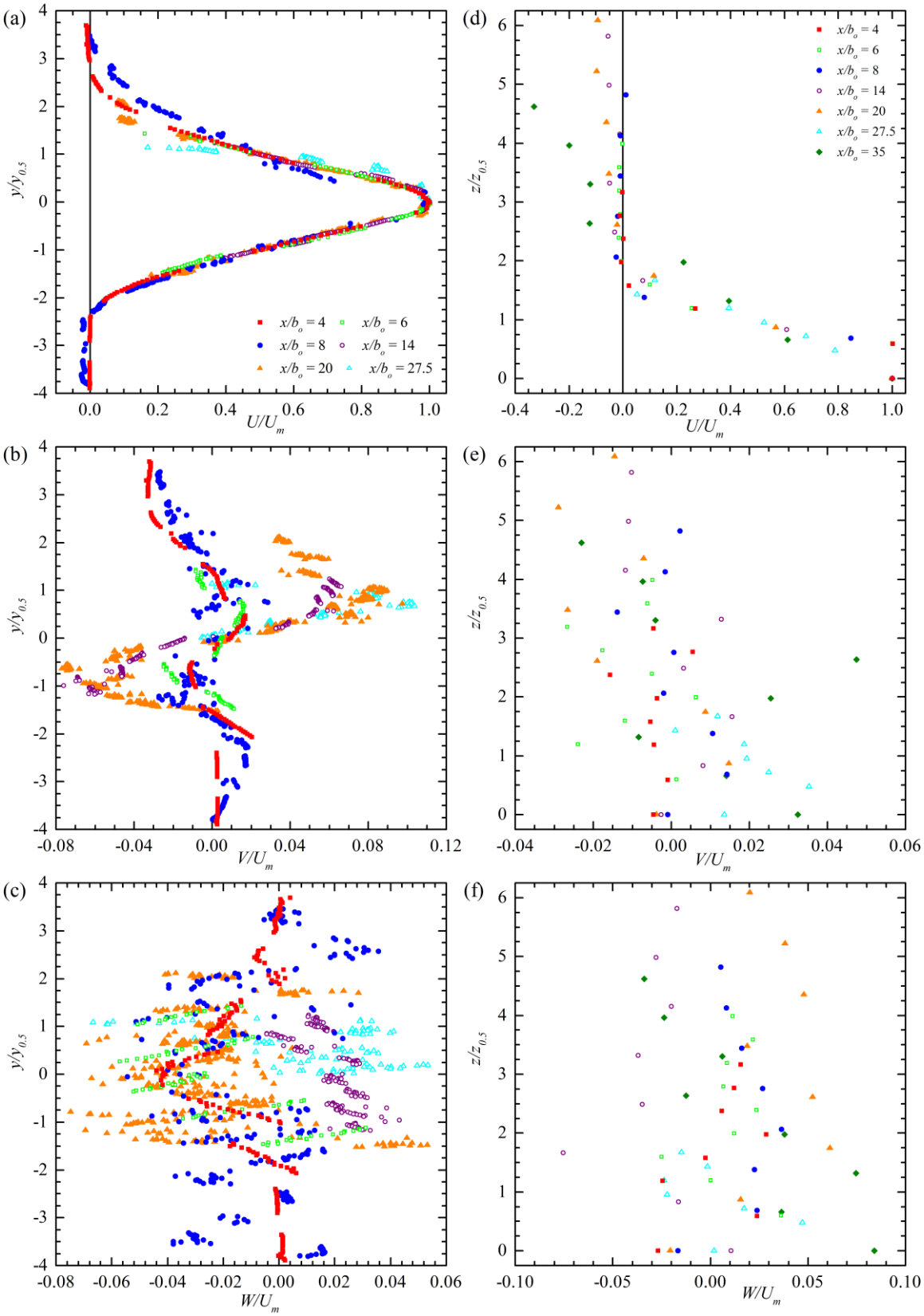

Figure 6-10 Velocity profiles for asymmetry ratio of 0.00

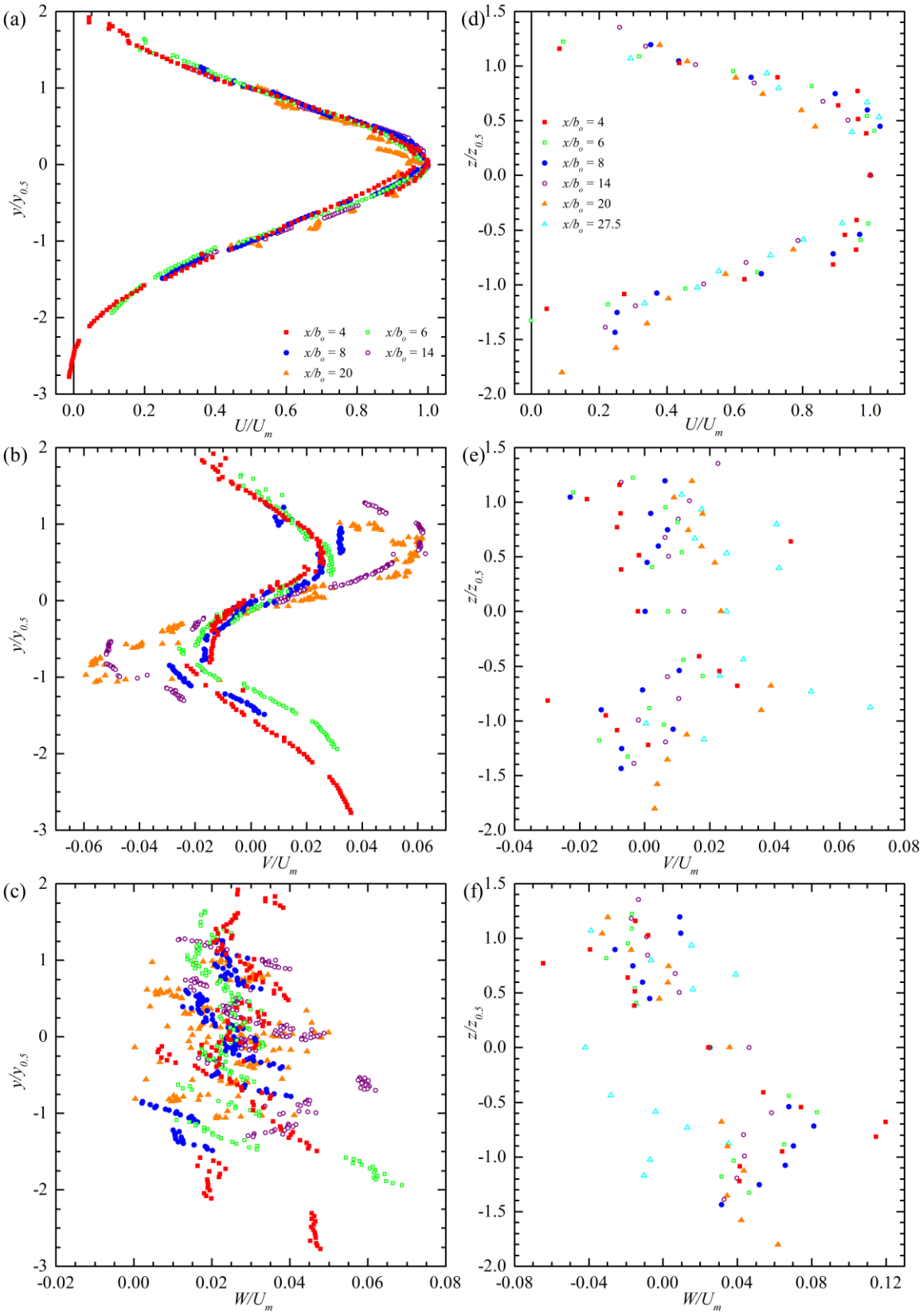

Figure 6-11 Velocity profiles for asymmetry ratio of 0.20

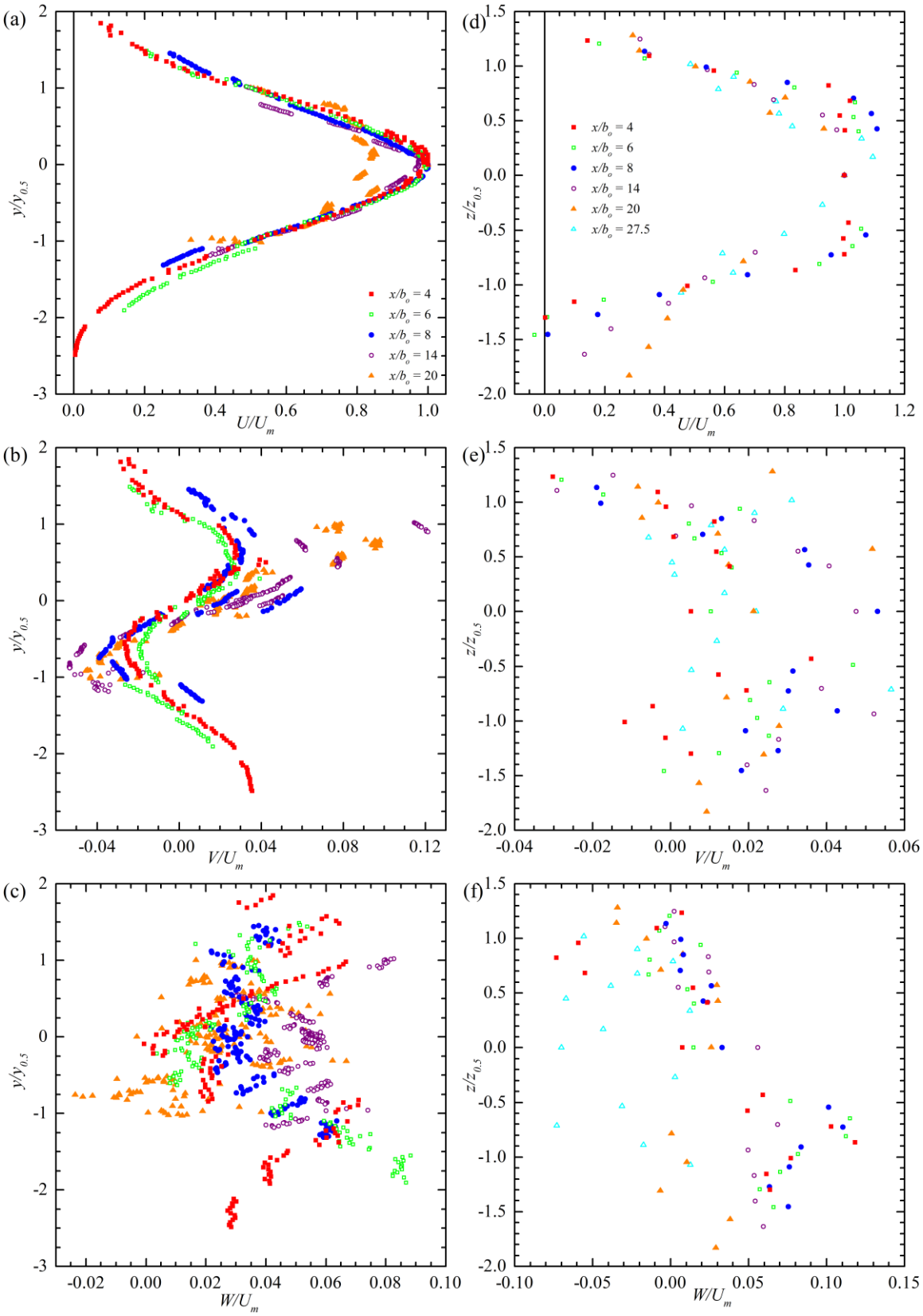

Figure 6-12 Velocity profiles for asymmetry ratio of 0.40

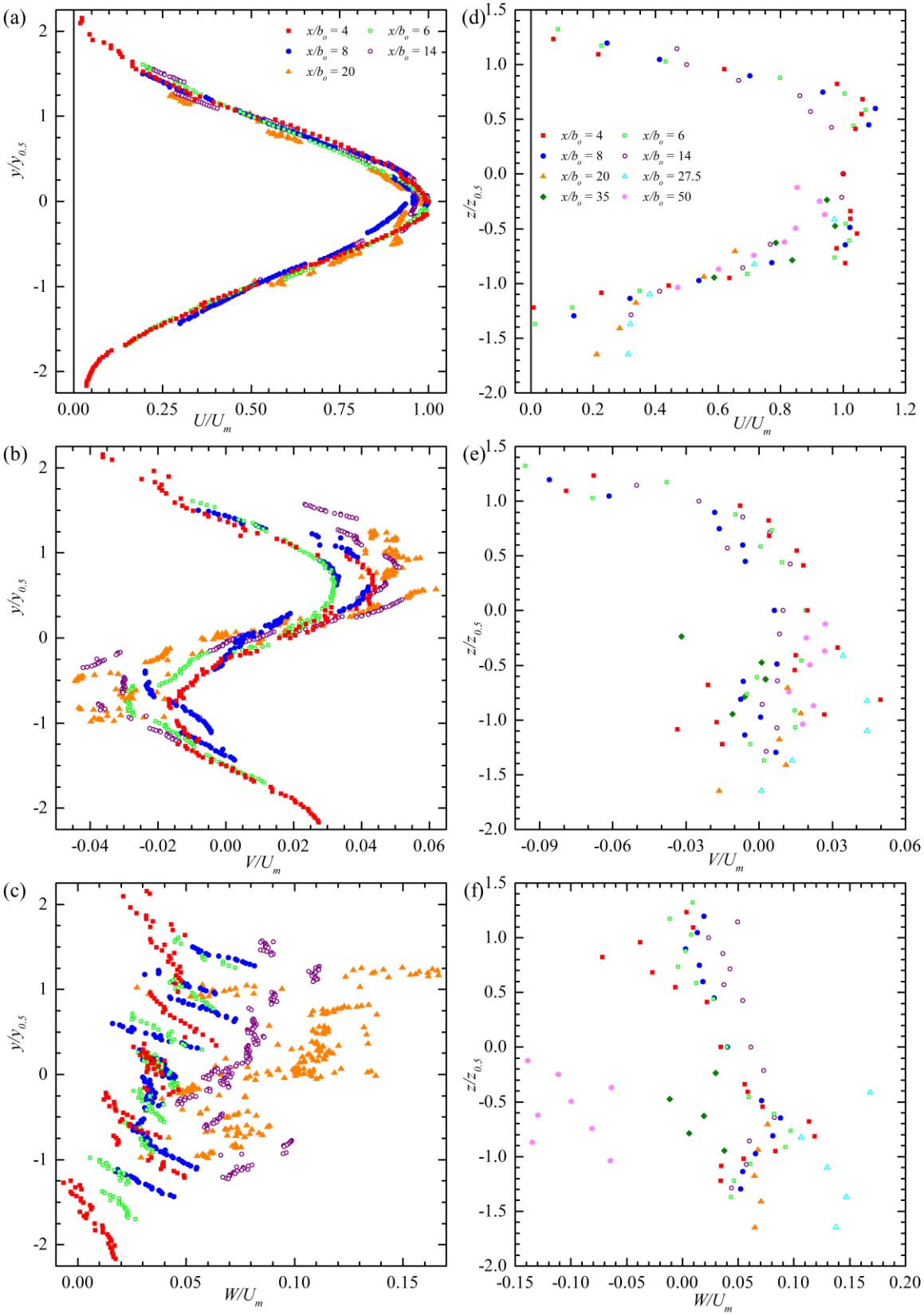

Figure 6-13 Velocity profiles for asymmetry ratio of 0.60

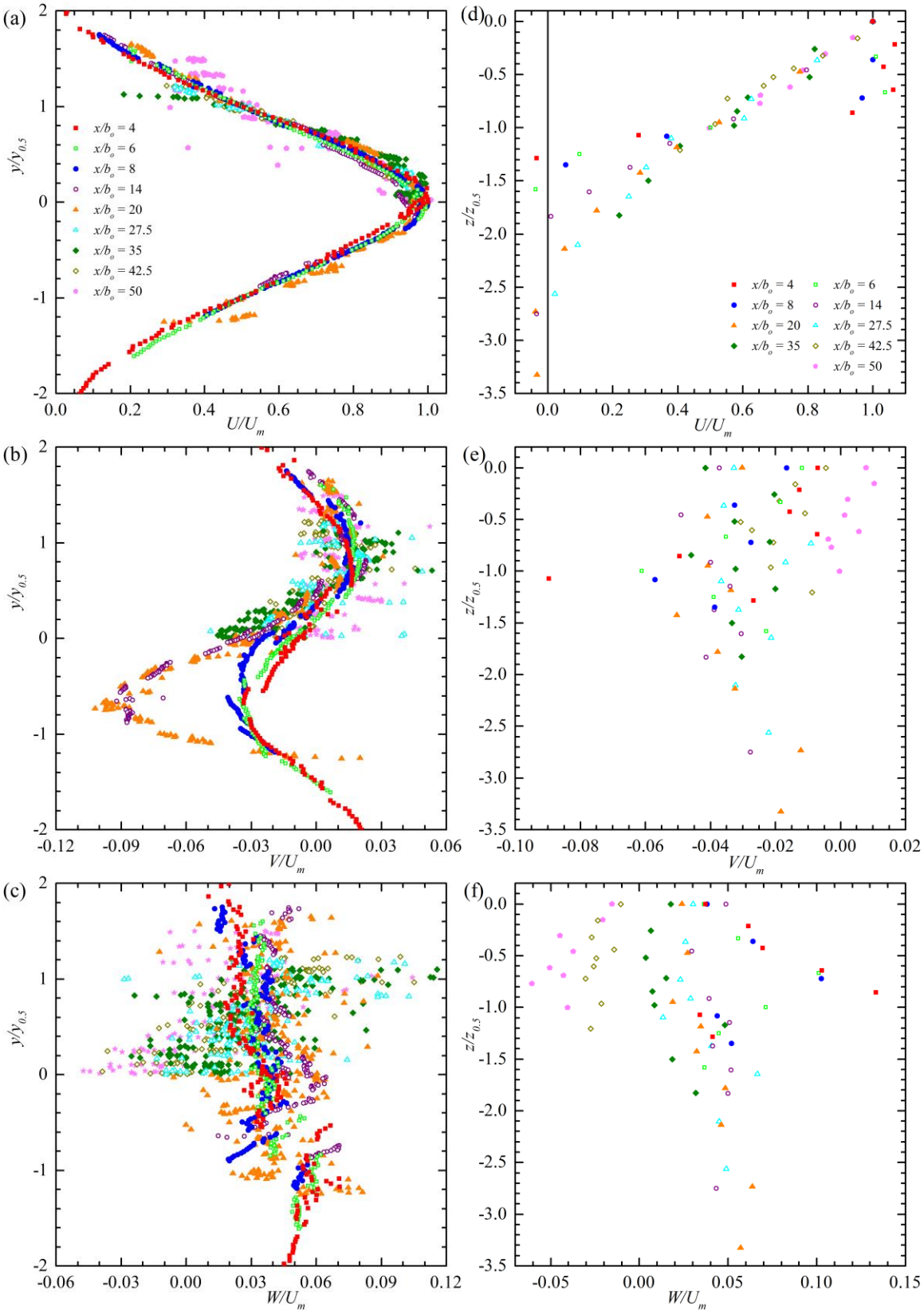

Figure 6-14 Velocity profiles for asymmetry ratio of 0.76

6.4 *Turbulence Intensities*

Vertical and lateral profiles of dimensionless turbulence intensities, u_{rms}/U_m, v_{rms}/U_m, and w_{rms}/U_m, are shown in Figure 6-15 to Figure 6-19. Only one side of the lateral profiles is shown at asymmetry ratio of 0.00 as both sides are identical. At asymmetry ratio of 0.76 the positive side of the jet is not shown because it is attached to the channel wall. The profiles are rendered dimensionless through the same convention outlined earlier.

The profiles feature a prominent double peak near the orifice which becomes less distinct with increasing streamwise distance. The peaks are located near the jet half widths, $y_{0.5}$ and $z_{0.5}$, where the velocity gradient is near its maximum both in the vertical and lateral profiles. Turbulence intensities decrease where the velocity gradient is reduced which forms the double peak. The velocity gradient decreases at the location of maximum streamwise velocity, $y = y_m$, in the vertical profiles and near the orifice centerline, $z = b'$, in the lateral profiles.

The magnitude of all three dimensionless turbulence intensities are seen to increase with streamwise distance. This indicates the local maximum streamwise velocity, U_m, to decay at a faster rate than the turbulence intensities. The turbulence intensities were confirmed to decay by looking at profiles of turbulence intensities, u_{rms}, v_{rms}, w_{rms}, not shown. Turbulence intensities, u_{rms}, v_{rms}, and w_{rms}, were observed to decay significantly at the two peaks while they stayed relatively constant near the location of maximum streamwise mean velocity, y_m. The turbulence intensities u_{rms} are highest in magnitude, followed by w_{rms}, then v_{rms}.

The magnitudes of turbulence intensities u_{rms} and v_{rms} do not differ significantly with changing asymmetry ratio while turbulence intensities w_{rms} in both shear layers have an

increasing trend with increasing asymmetry ratio. The turbulence intensities w_{rms} in the negative shear layer achieve higher values than the turbulence intensities in the positive shear layer.

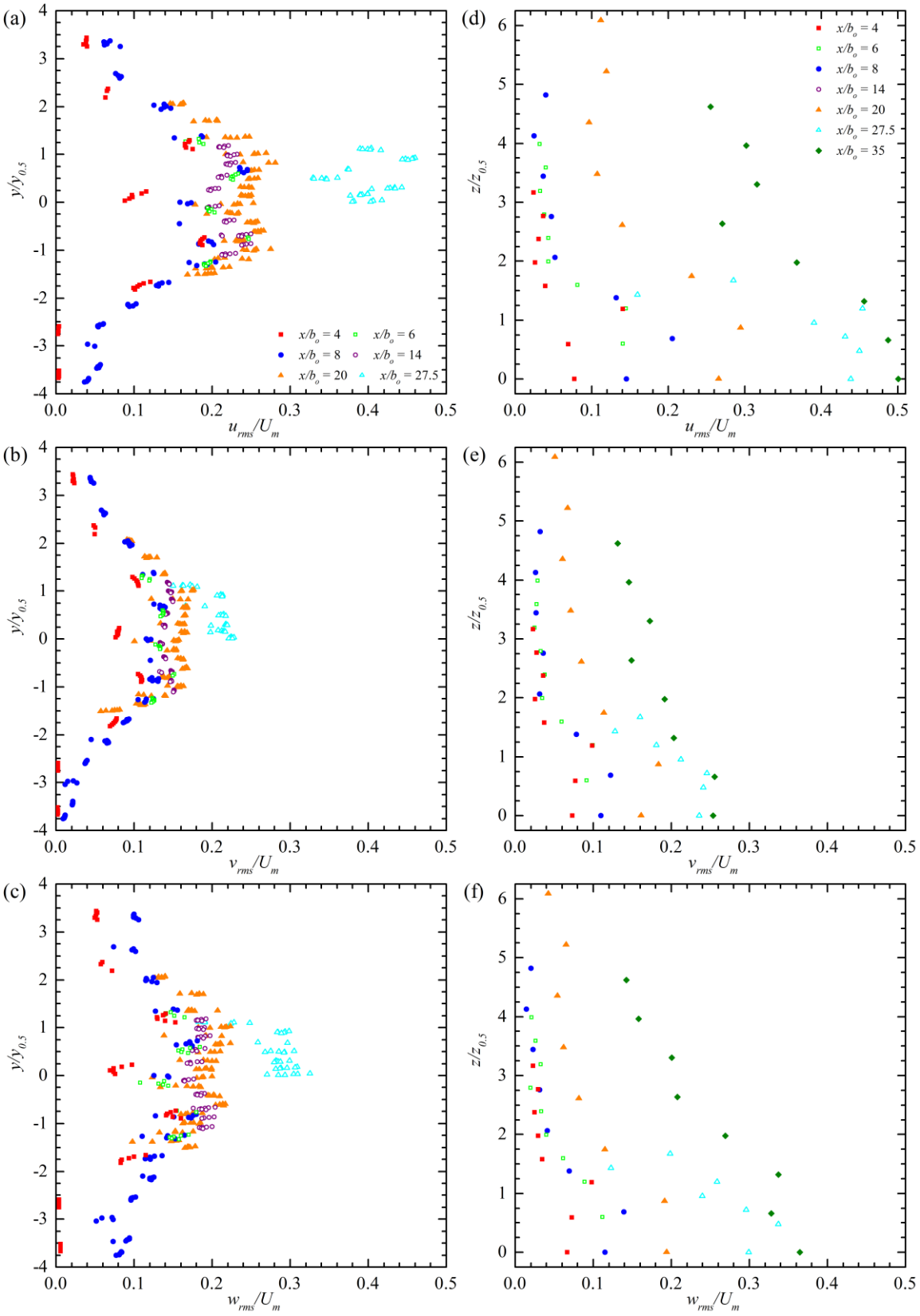

Figure 6-15 Profiles of turbulence intensities for asymmetry ratio of 0.00

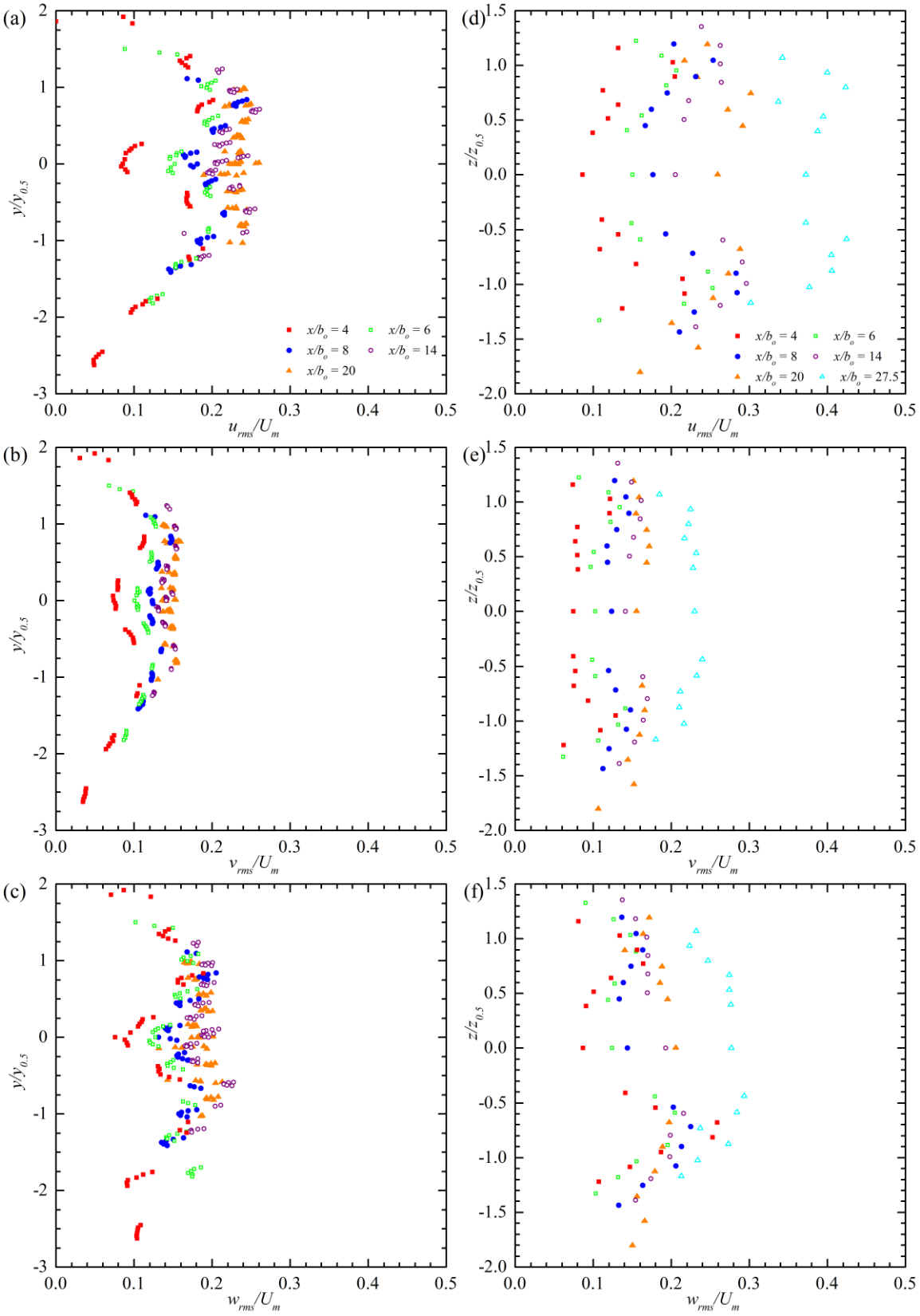

Figure 6-16 Profiles of turbulence intensities for asymmetry ratio of 0.20

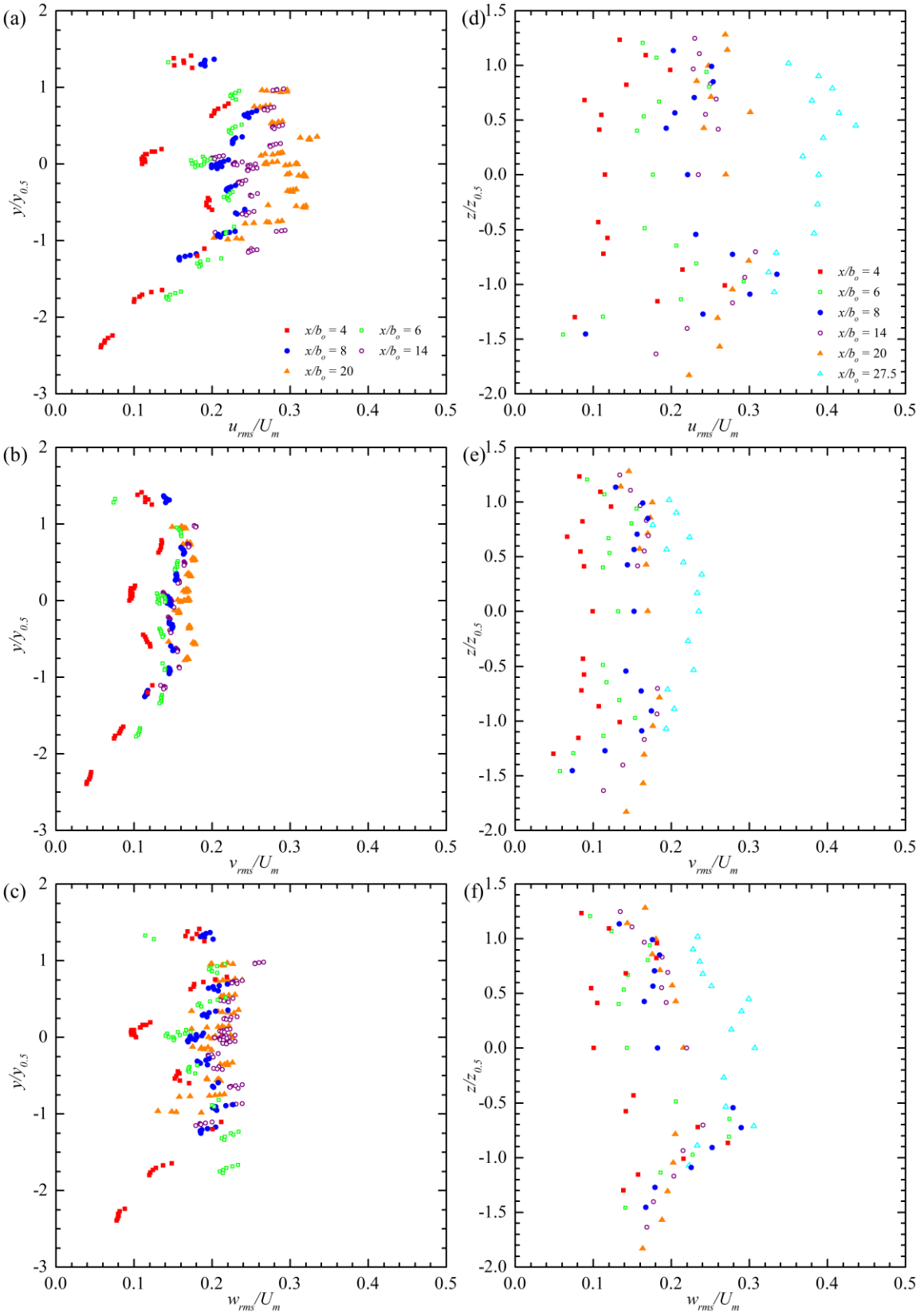

Figure 6-17 Profiles of turbulence intensities for asymmetry ratio of 0.40

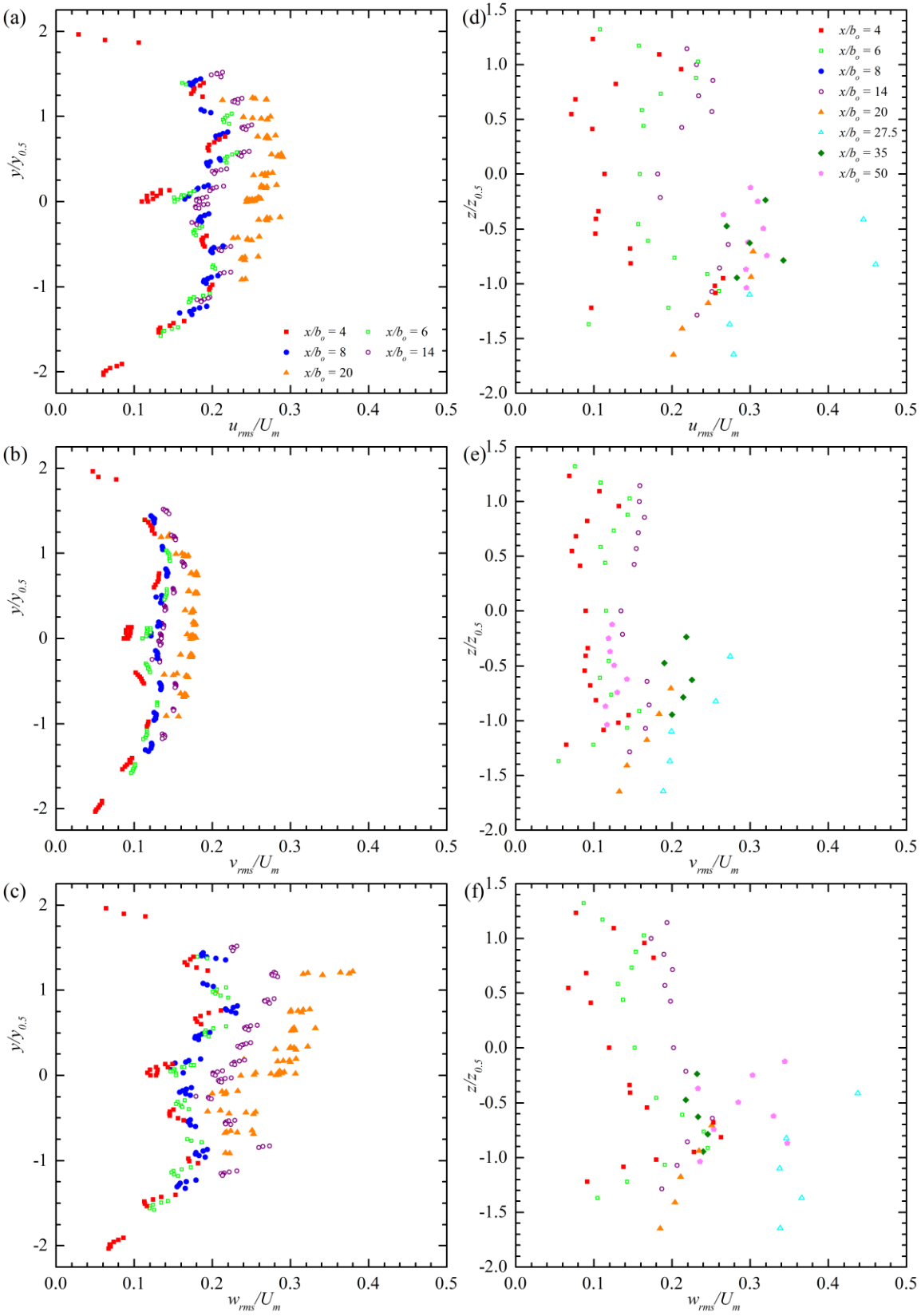

Figure 6-18 Profiles of turbulence intensities for asymmetry ratio of 0.60

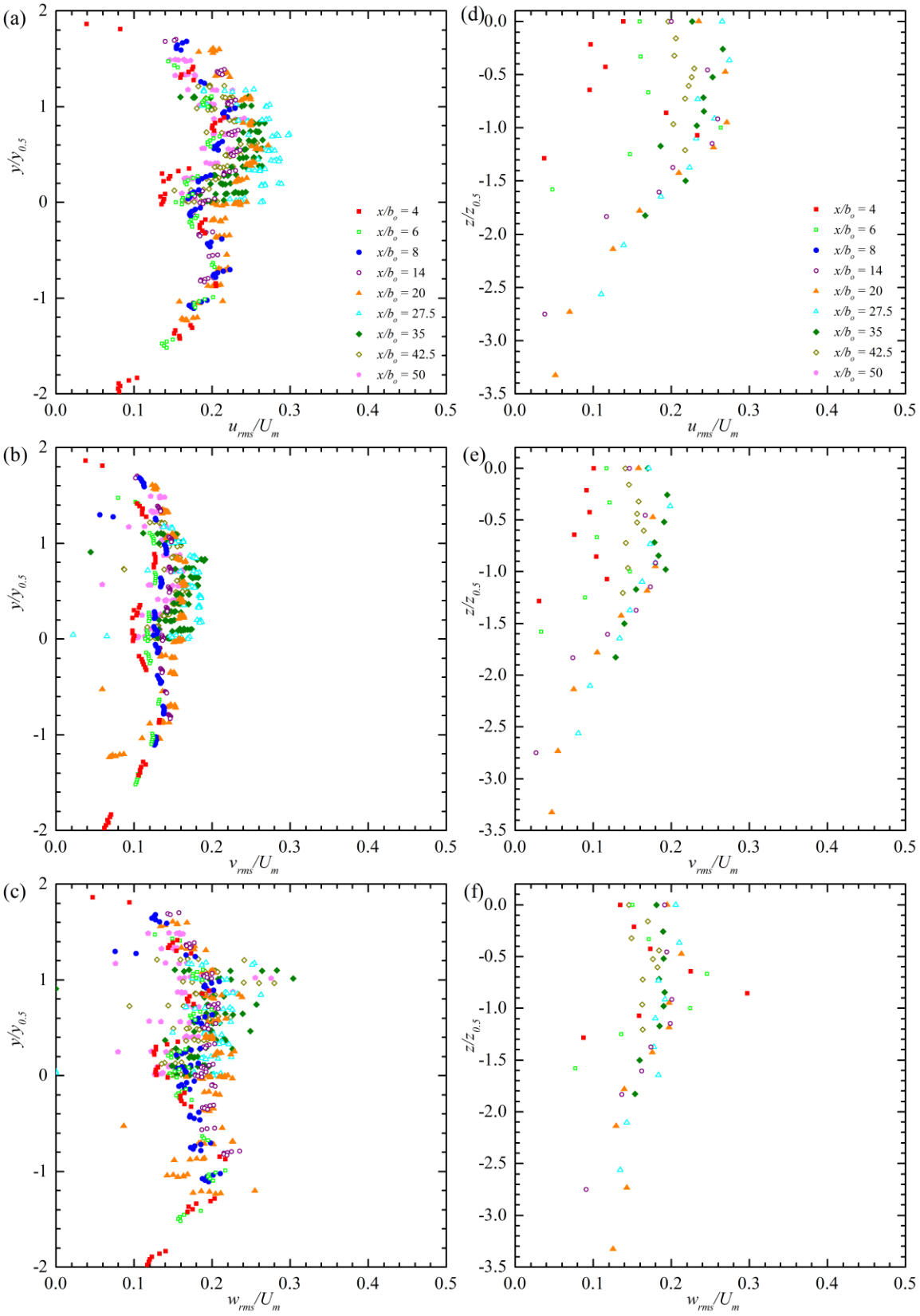

Figure 6-19 Profiles of turbulence intensities for asymmetry ratio of 0.76

6.5 *Turbulent Kinetic Energy*

Profiles of turbulent kinetic energy, *k*, are shown in Figure 6-20 to Figure 6-24. The turbulent kinetic energy, *k*, is calculated using all three components of turbulence intensity as $k = 1/2\,(u_{rms}^2 + v_{rms}^2 + w_{rms}^2)$. This is unlike many of the previous studies where the turbulent kinetic energy was estimated from two of the three components of turbulence intensity. The trend seen in the profiles of turbulent kinetic energy, *k*, is

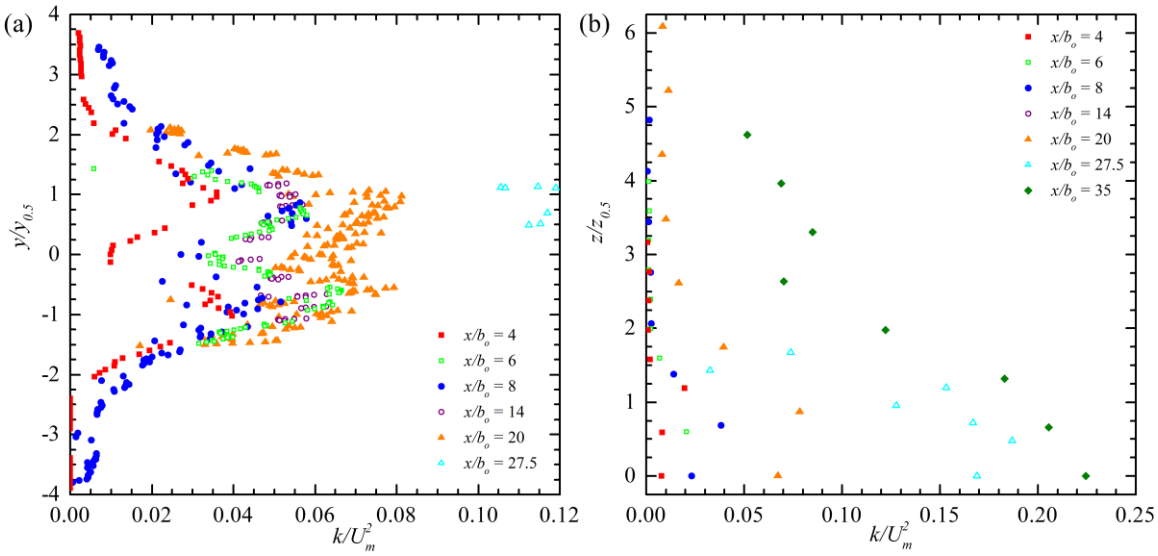

Figure 6-20 Turbulent kinetic energy for asymmetry ratio of 0.00 (a) vertical profile (b) lateral profile

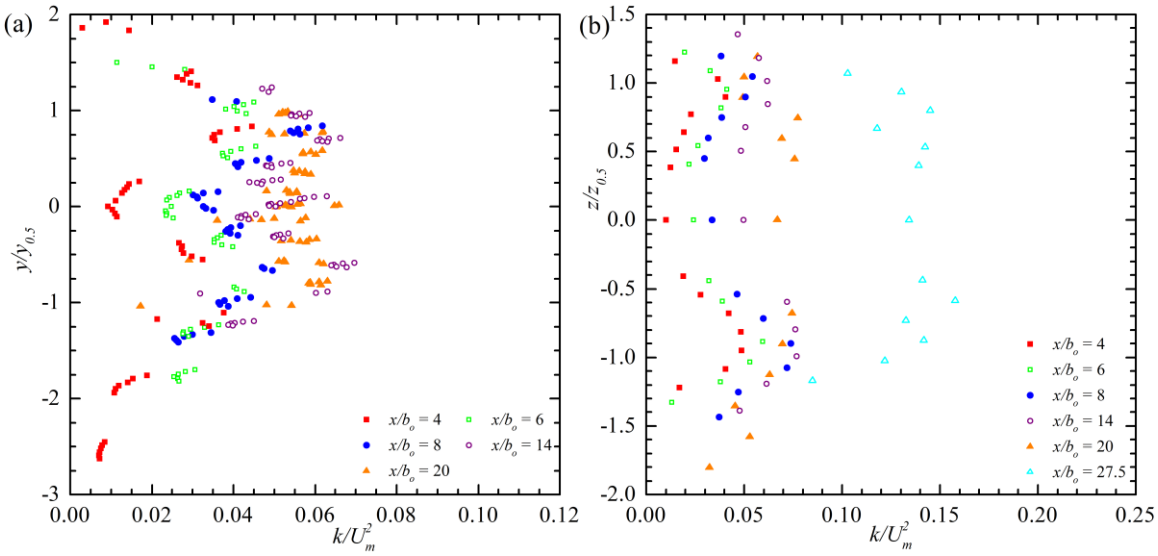

Figure 6-21 Turbulent kinetic energy for asymmetry ratio of 0.20 (a) vertical profile (b) lateral profile

similar to that seen in the profiles of turbulence intensities. The profiles feature a double peak in both vertical and lateral profiles near the jet half widths, $y_{0.5}$ and $z_{0.5}$, with a reduction in turbulent kinetic energy near the vertical location of maximum streamwise velocity, y_m, and orifice centerline, b'. The dimensionless turbulent kinetic energy, k/U_m, increases with increasing streamwise distance, x/b_o, and the double peaks become less pronounced. It was confirmed that the turbulent kinetic energy, k, decays at a slower rate

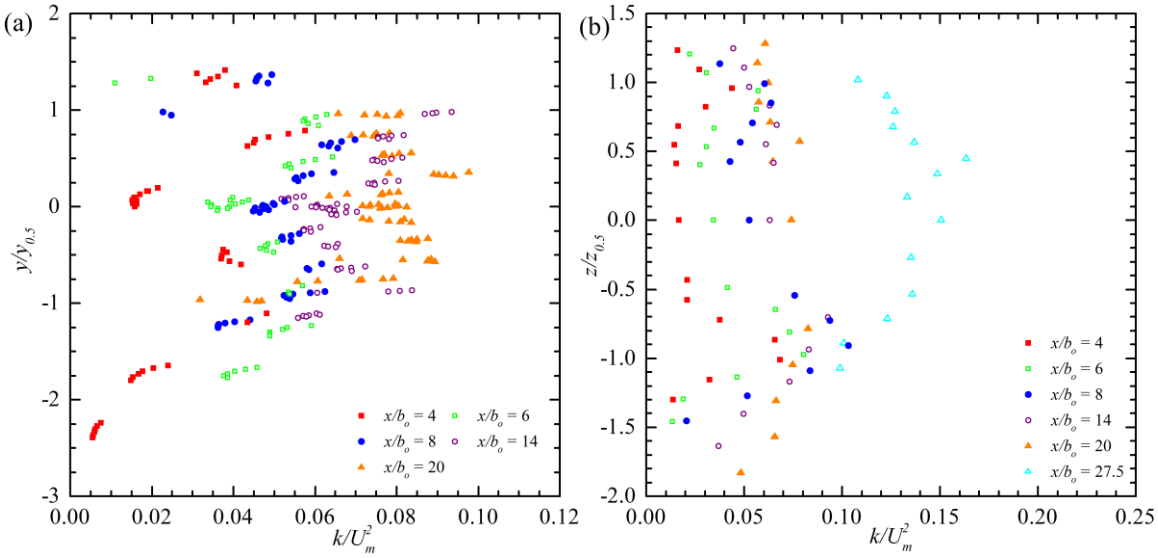

Figure 6-22 Turbulent kinetic energy for asymmetry ratio of 0.40 (a) vertical profile (b) lateral profile

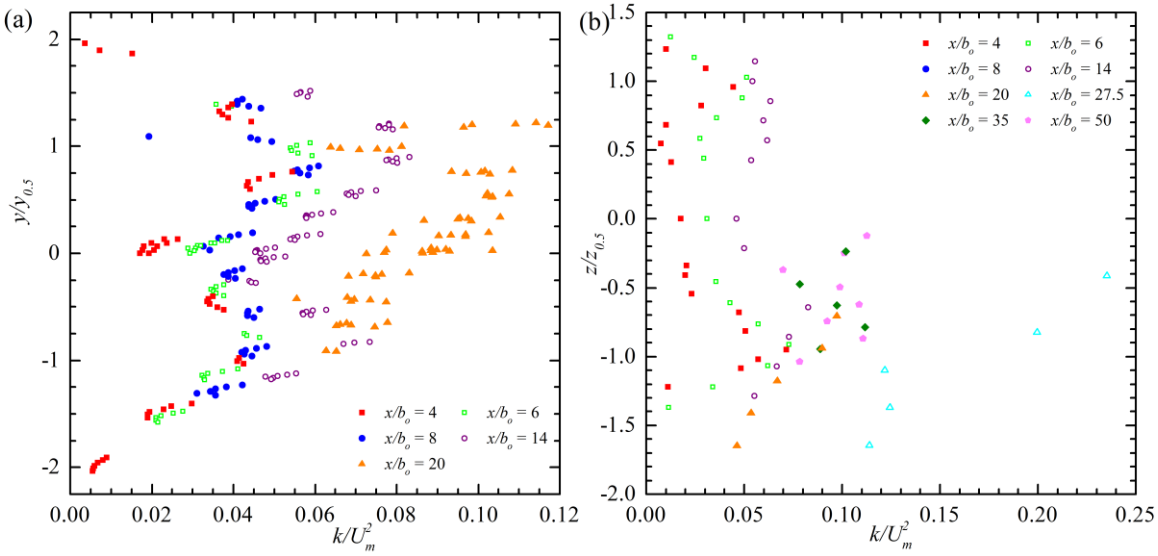

Figure 6-23 Turbulent kinetic energy for asymmetry ratio of 0.60 (a) vertical profile (b) lateral profile

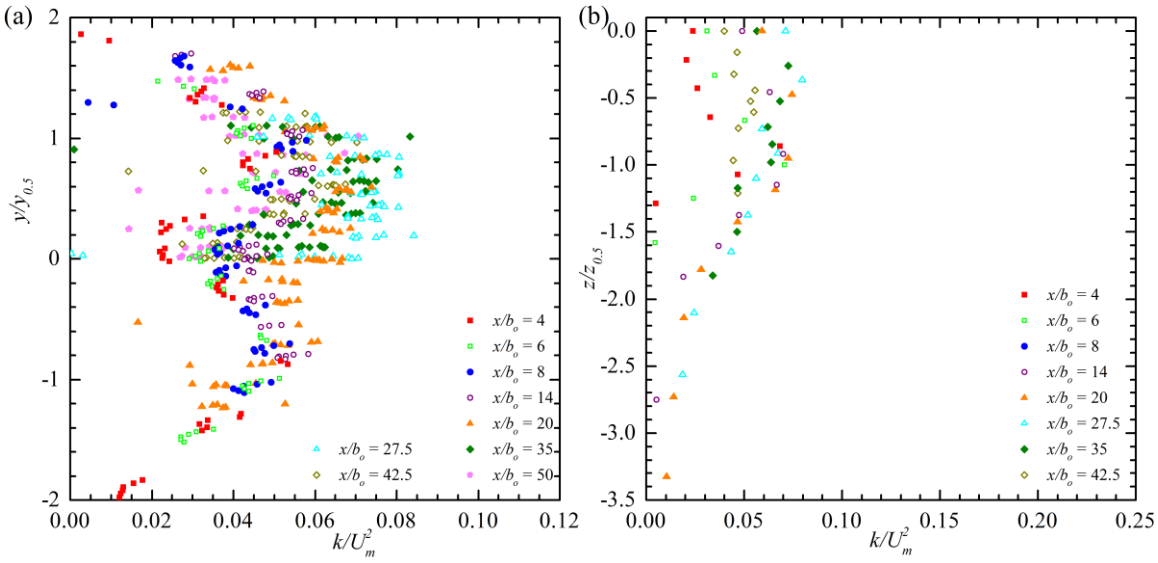

Figure 6-24 Turbulent kinetic energy for asymmetry ratio of 0.76 (a) vertical profile (b) lateral profile

than the maximum streamwise mean velocity, U_m, by looking at vertical profiles of turbulent kinetic energy, k. Higher levels of turbulent kinetic energy were achieved with increased asymmetry ratio and the decay rate was also increased. Similar levels of turbulent kinetic energy, k, were achieved for all asymmetry ratios by a streamwise distance $x/b_o = 20$.

6.6 *Reynolds Shear Stresses*

Profiles of Reynolds shear stresses are shown in Figure 6-25 to Figure 6-29. The profiles are normalized using the convention outlined above. The lateral profiles of asymmetry ratio of 0.00 and 0.76 only have one side shown for the same reason as previously explained. Vertical profiles of Reynolds shear stress uv at all asymmetry ratios are antisymmetric with peaks near both jet half width, $y_{0.5}$, and zero at the location of maximum streamwise velocity. The magnitude is seen to increase slightly with streamwise distance indicating that the Reynolds shear stress uv decays just slightly slower than the maximum streamwise mean velocity, U_m. A slight antisymmetric trend is observed in the vertical profiles of Reynolds shear stress uw however the magnitudes are

much lower than the Reynolds shear stress *uv*. At asymmetry ratio of 0.00 the profile is initially equal to zero and the magnitude increases as it develops into an antisymmetric profile with streamwise distance. The vertical profiles of Reynolds shear stress *vw* are equal to zero at all asymmetry ratios.

Of the three lateral profiles of Reynolds shear stress, the Reynolds shear stress *uw* shows the most significant trend. It has an antisymmetric trend that increases in magnitude with increasing streamwise distance while Reynolds shear stress *uv* and *vw* stay close to zero and do not significantly increase with streamwise distance. The peaks of Reynolds shear stress *uw* are located near the jet half width $z_{0.5}$, the magnitudes achieved at these peaks by a streamwise distance of $x/b_o = 20$ are seen to decrease with increasing asymmetry ratio.

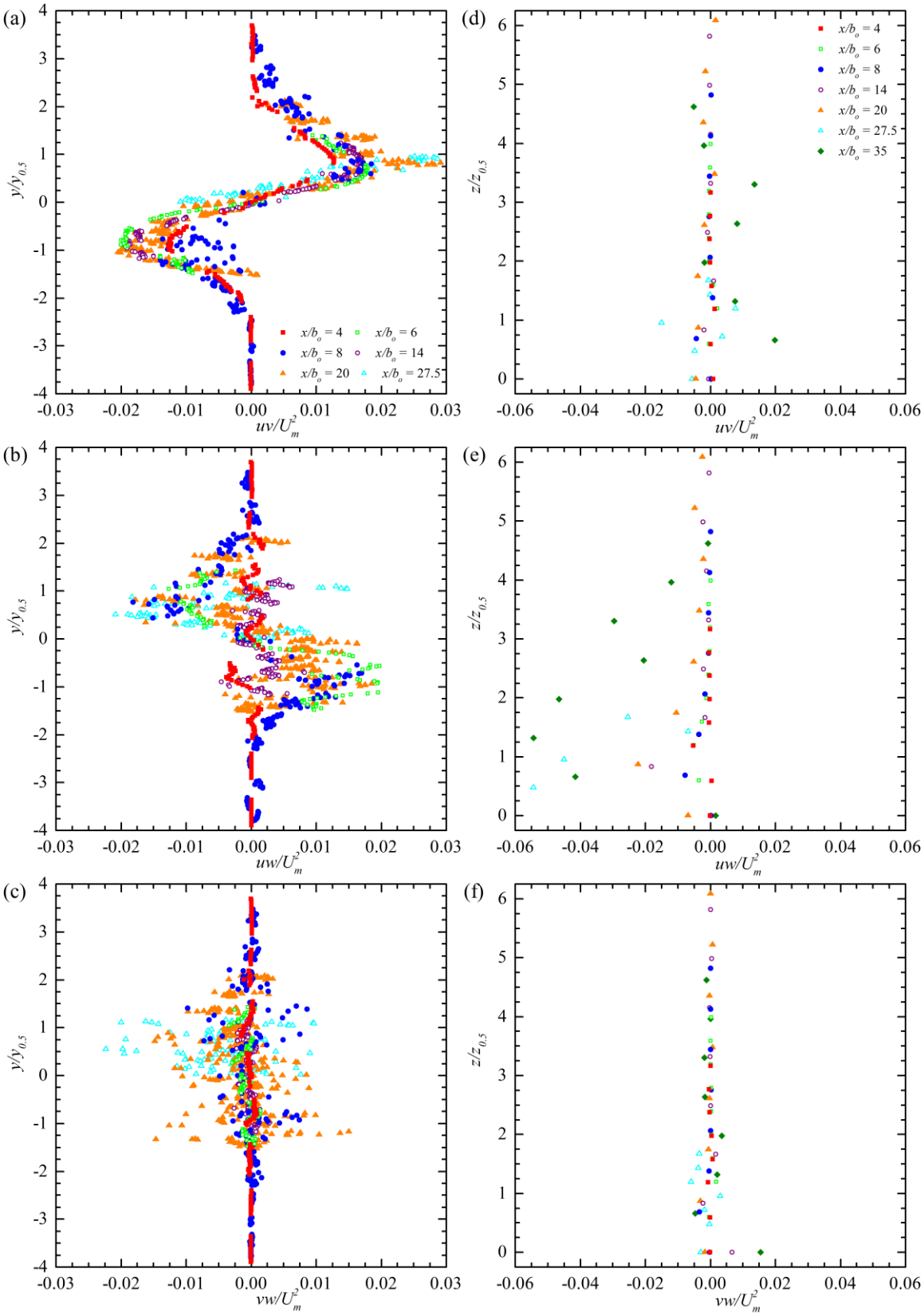

Figure 6-25 Profiles of Reynolds shear stresses for asymmetry ratio of 0.00

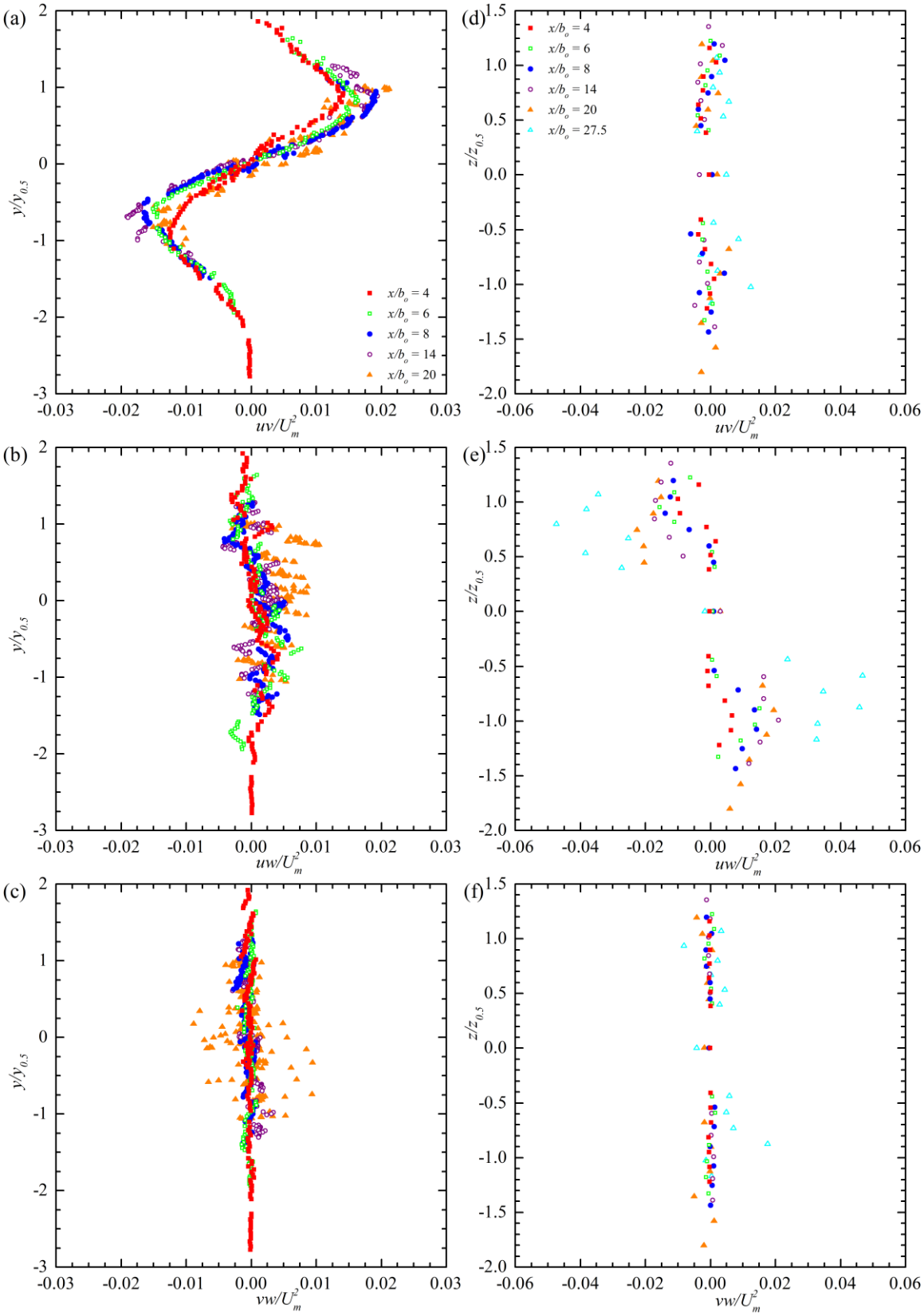

Figure 6-26 Profiles of Reynolds shear stresses for asymmetry ratio of 0.20

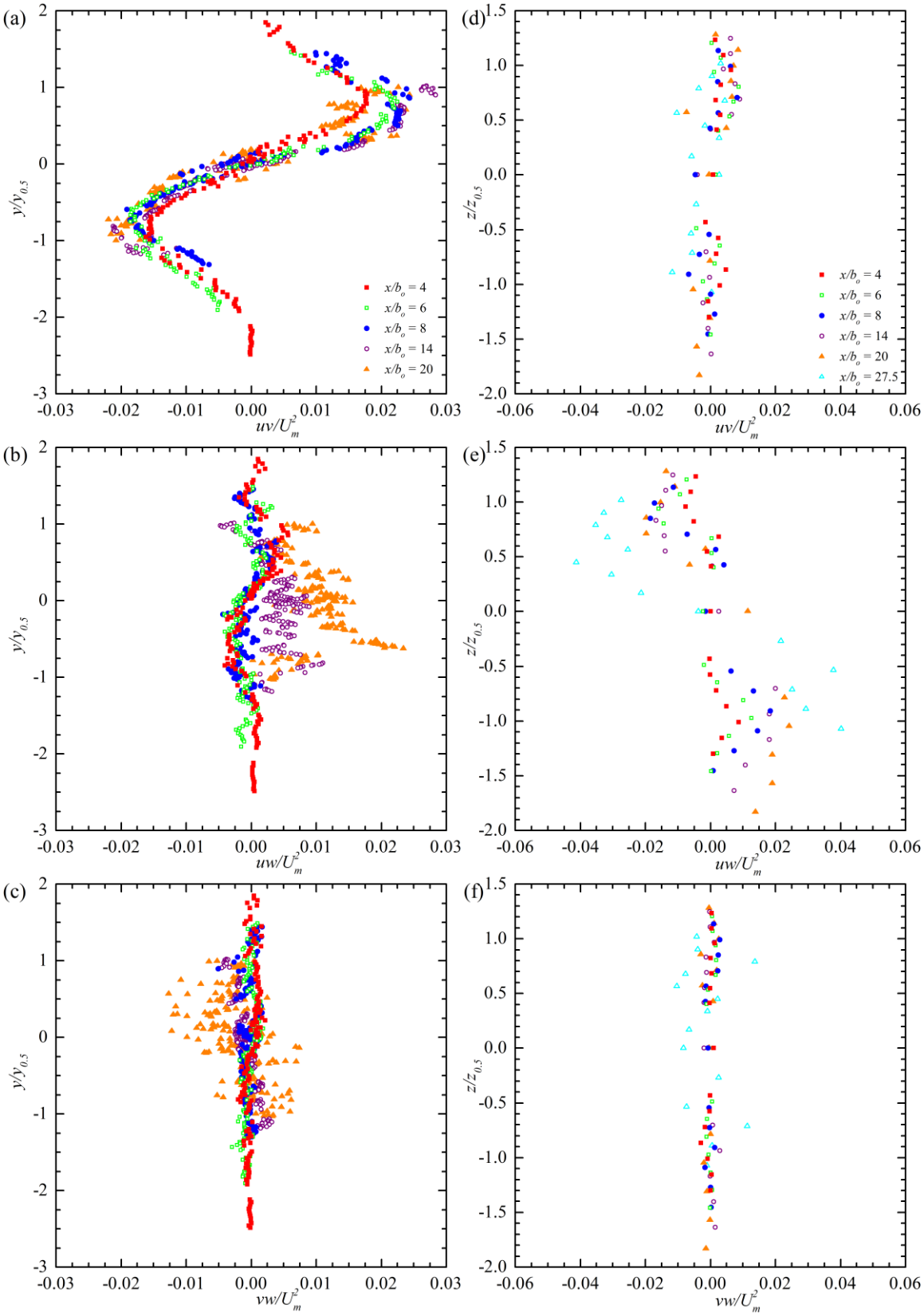

Figure 6-27 Profiles of Reynolds shear stresses for asymmetry ratio of 0.40

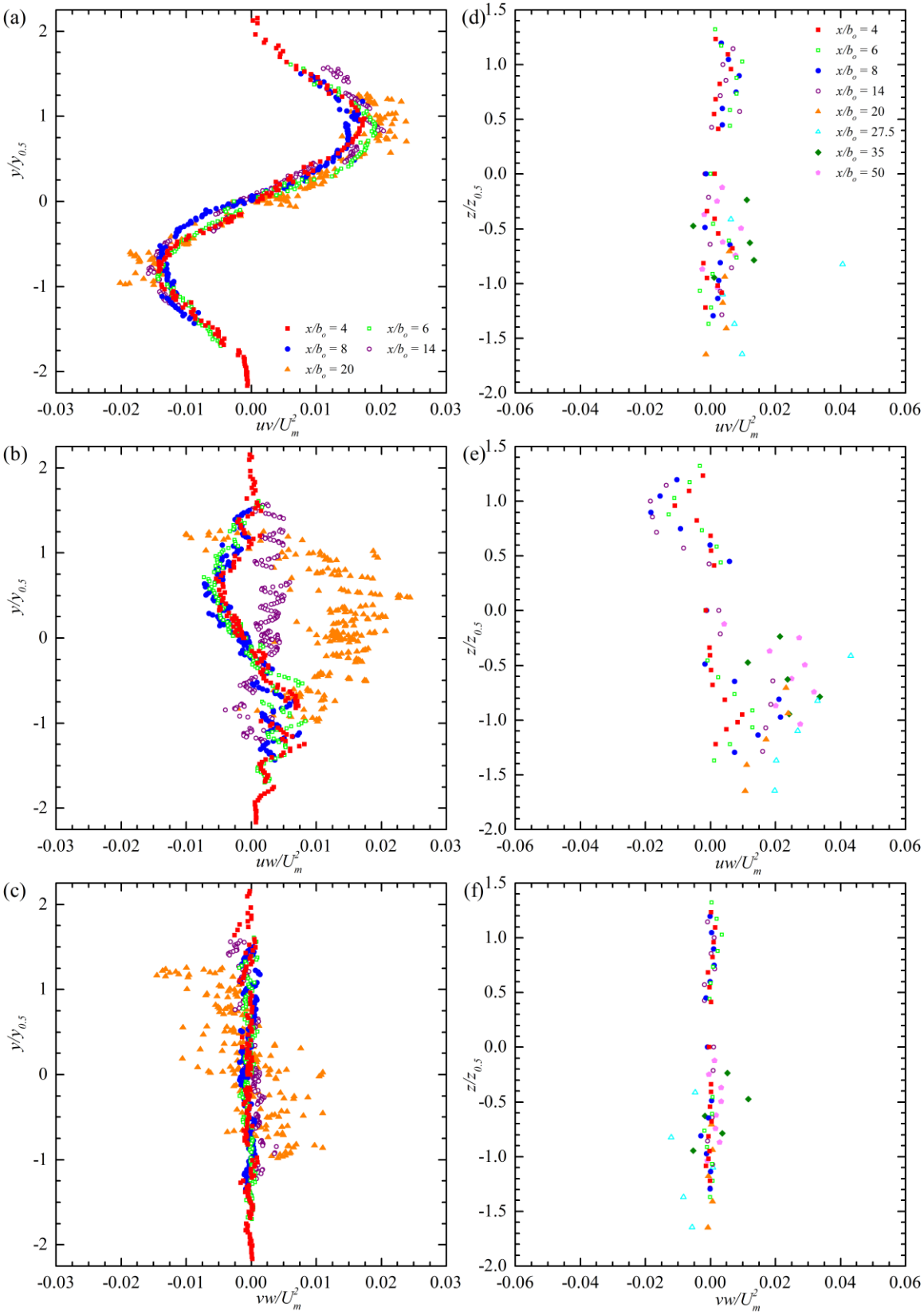

Figure 6-28 Profiles of Reynolds shear stresses for asymmetry ratio of 0.60

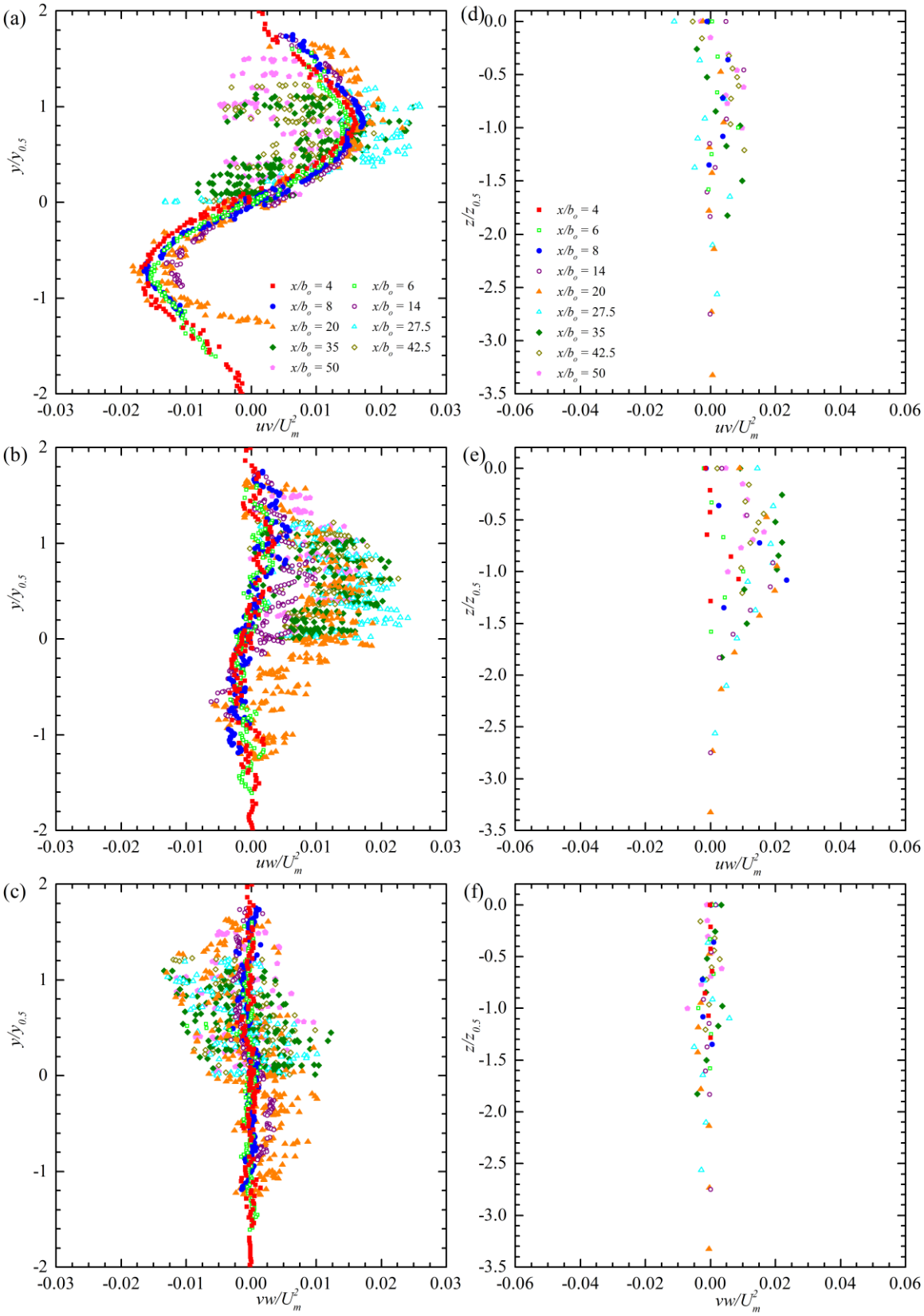

Figure 6-29 Profiles of Reynolds shear stresses for asymmetry ratio of 0.76

6.7 *Triple Velocity Correlations*

The triple velocity correlation terms can provide insight into how turbulence is diffused throughout the jet. Very few studies have reported triple velocity correlation terms and none has reported the triple velocity correlation term *uvw* because of limitations from the employed measurement technique. The spatial gradients of triple velocity correlation terms make up the turbulent diffusion terms in the transport equations for turbulent kinetic energy and Reynolds stresses which require modelling. The distribution of triple

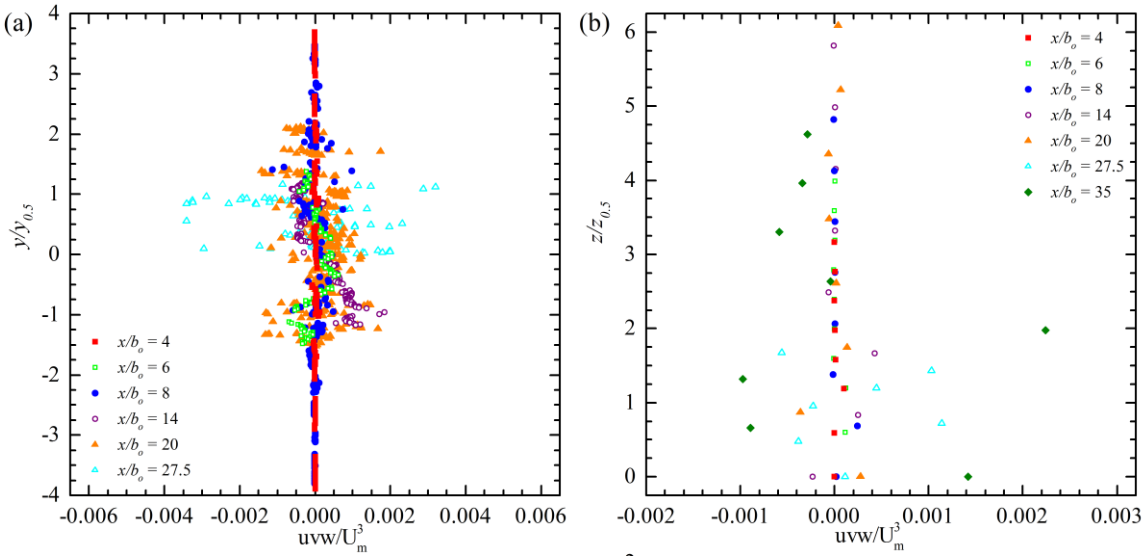

Figure 6-30 Triple velocity correlation for asymmetry ratio of 0.00 (a) vertical profile (b) lateral profile

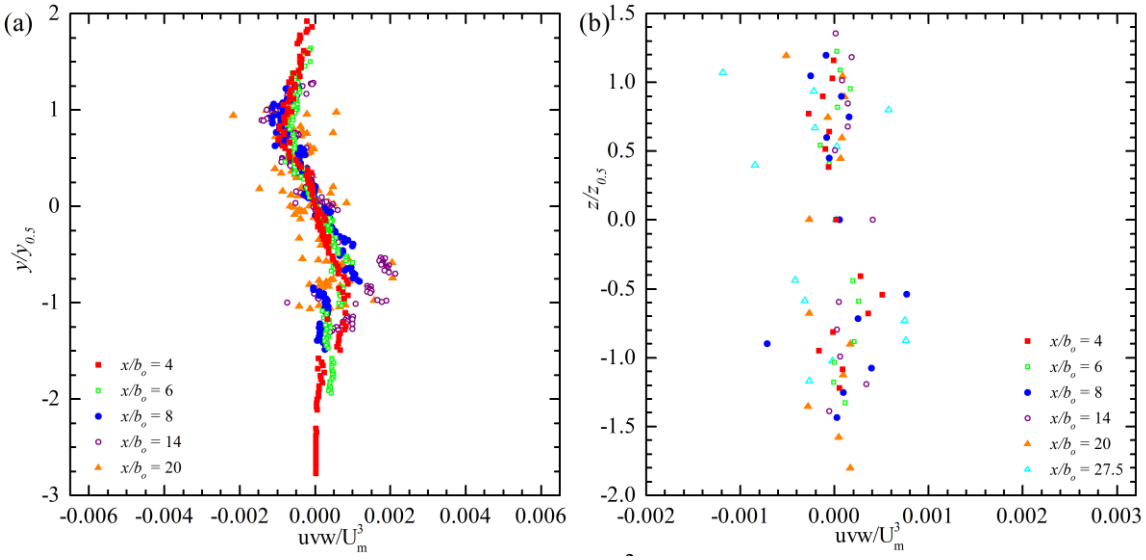

Figure 6-31 Triple velocity correlation for asymmetry ratio of 0.20 (a) vertical profile (b) lateral profile

velocity correlation will help in developing reliable turbulence models. Figure 6-30 to Figure 6-34 show the vertical and lateral profiles of the triple velocity correlation *uvw* at all five asymmetry ratios. At asymmetry ratio of 0.00 the triple velocity correlation in the vertical profile is zero. At asymmetry ratio of 0.20 to 0.76 the profiles take an antisymmetric shape and increase in magnitude for asymmetry ratio of 0.20 to 0.60, at asymmetry ratio of 0.76 the magnitude is reduced. The magnitude does not increase significantly with streamwise distance.

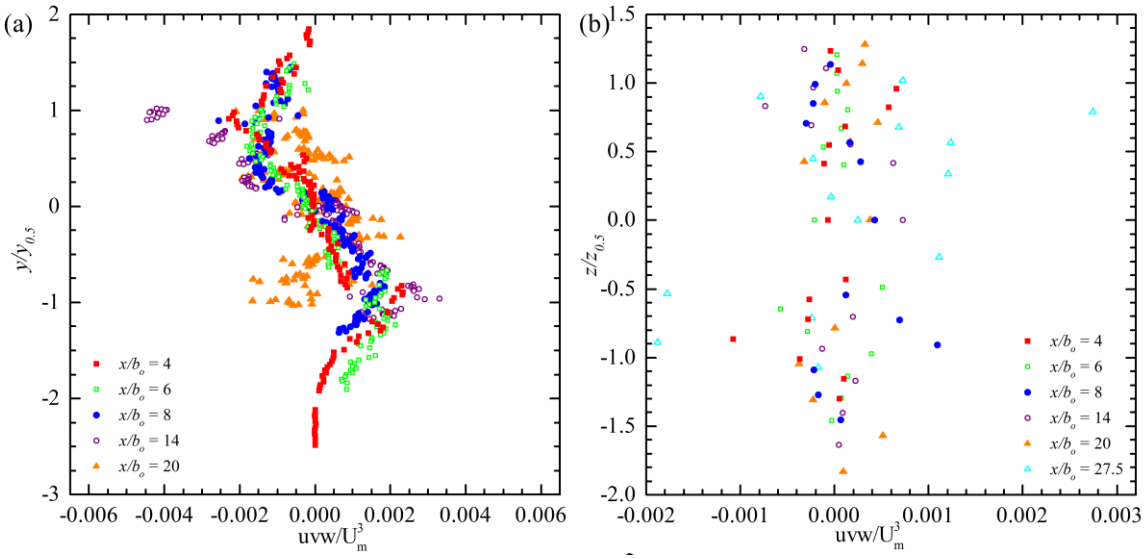

Figure 6-32Triple velocity correlation for asymmetry ratio of 0.40 (a) vertical profile (b) lateral profile

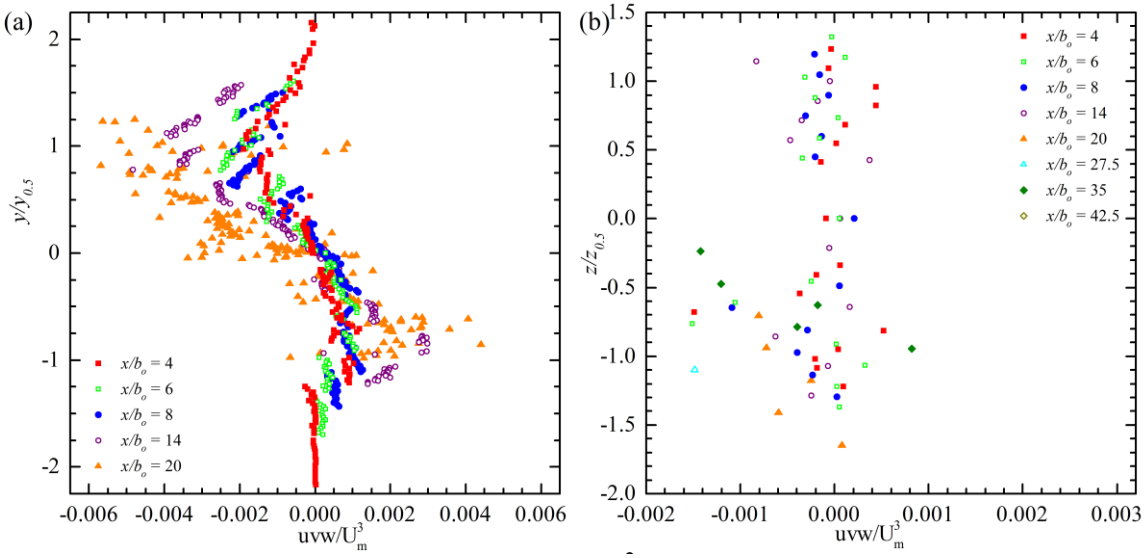

Figure 6-33 Triple velocity correlation for asymmetry ratio of 0.60 (a) vertical profile (b) lateral profile

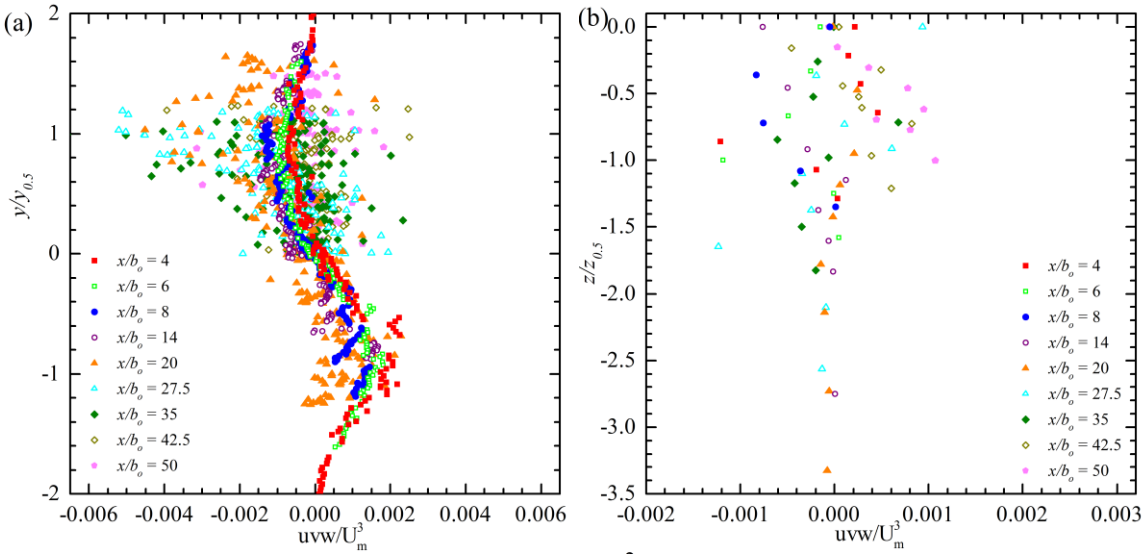

Figure 6-34 Triple velocity correlation for asymmetry ratio of 0.76 (a) vertical profile (b) lateral profile

6.8 *Summary*

The effects of asymmetry ratio on three-dimensional offset jets have been investigated with the aid of a physical model experiment. An analysis of the effects of asymmetry ratio on streamwise flow development and profiles of mean velocities and turbulence statistics has been completed.

As the jet issues from an orifice the Coanda effect forces the jet to curve towards solid boundaries. The jet curves towards the channel bottom and, with increasing asymmetry ratio, towards the channel wall. With increasing asymmetry ratio both of these curves become more pronounced. The decay of maximum streamwise mean velocity is significantly reduced at high asymmetry ratios after the jet reattaches to the channel wall. The linearly decay rate, n_l, of a jet increases with increasing asymmetry ratio, however, it decreases when the orifice is directly adjacent to the wall. At high asymmetry ratios, after the jet has reattached to the wall, its decay rate, n_p, in the wall jet region is similar to that of a two-dimensional offset jet. The streamwise mean velocity achieves self-similarity near the orifice and show recirculation zones beyond a half width of $y/y_{0.5} = \pm 2$. The lateral velocities increase with increasing asymmetry ratio as the Coanda effect forces the jet towards the channel wall.

Profiles of turbulence intensities, u_{rms}, v_{rms}, and w_{rms}, and turbulent kinetic energy, k, showed higher turbulence levels near the jet half widths, $y_{0.5}$ and $z_{0.5}$, and decrease with increasing streamwise distance. The turbulence levels at the location of maximum streamwise mean velocity, y_m, stayed constant throughout the channel and did not decay significantly. The turbulence intensity w_{rms} and turbulent kinetic energy, k, increase with

asymmetry ratio. The level of turbulence intensity w_{rms} is higher in the positive shear layer.

The Reynolds shear stresses, *uv*, *uw*, and *vw*, and triple velocity correlation terms are important in turbulence models to simulate the production and diffusion of turbulence, respectively. The data collected during this study will help to calibrate and validate turbulence models for flow conditions similar to that of offset jets. Antisymmetric profiles are seen in Reynolds shear stresses with *uv* and *uw* being dominant in the *xy*-plane and *xz*-plane, respectively. The highest magnitude achieved by the peaks of Reynolds shear stress *uw* is decreased with increasing asymmetry ratio. Profiles of triple velocity correlation display an antisymmetric shape that increases in magnitude with asymmetry ratio except at the maximum asymmetry ratio where it is reduced slightly.

CHAPTER 7: CONCLUSIONS AND RECOMMENDATIONS

7.1 *Conclusions*

This experimental study evaluated the effects of tailwater level and asymmetry ratio on three-dimensional offset jets. The effects of Reynolds number were also evaluated during preliminary experiments of this study. The three sets of experiments quantified the effects on decay and spread rates of three-dimensional offset jets as well as their distribution of mean velocity and higher order turbulence statistics. The major contributions of this research are listed below, followed by practical relevance and recommendations.

7.1.1 *Effects of Reynolds Number*

The significant effects of Reynolds number on three-dimensional offset jets are as follows:

1. Effects of Reynolds number on decay rate, n_p, are insignificant at $\mathrm{Re} \geq 53{,}000$.
2. The vertical spread rate is independent of Reynolds number at $\mathrm{Re} \geq 53{,}000$ for streamwise extent of $0 \leq x/b_o \leq 20$.

3. Reynolds number had no significant effect on vertical profiles of mean velocities, *U*, *V*, and *W*, turbulence intensities, u_{rms}, v_{rms}, and w_{rms}, and turbulent kinetic energy, *k*.
4. Reynolds shear stresses in the *xy*-plane, *uv*, is independent of Reynolds number. Reynolds shear stress in the *xz*-plane, *uw*, decreases but maintains the same order of magnitude with increasing Reynolds number.

7.1.2 *Effects of Tailwater Level*

Tailwater level had the following significant effects on three-dimensional offset jets:

1. An offset jet will curve towards the channel bottom in high tailwater. At low tailwater levels the jet will move towards the water surface instead.
2. The decay rate of reattaching offset jets will increase with decreasing tailwater in both the recirculation region and the wall jet region.
3. The vertical spreading of a three-dimensional offset jet is not significantly affected by the tailwater level while the coefficients of lateral spreading, l_1 and l_2, increase with decreasing tailwater level. The streamwise location of the inflection point, x_{vc}, and minimum lateral jet half width decrease with decreasing tailwater level.
4. Profiles of turbulence intensities and turbulent kinetic energy feature a double peak that disappears with increasing streamwise distance. The level of turbulence in a jet increases with decreasing tailwater level.
5. Reynolds shear stress *uv* was not significantly affected by changes in tailwater level. Triple velocity correlation *uvw* increased with decreasing tailwater which hints at an increase of turbulence diffusion.

7.1.3 *Effects of Asymmetry Ratio*

The significant effects of asymmetry ratio on three-dimensional offset jets are listed below:

1. An increasing asymmetry ratio will cause an offset jet to curve faster towards the channel bottom and closest wall.
2. At high asymmetry ratios, when the jet reattaches to the channel wall, the maximum streamwise mean velocity will decay to 35-45% of the bulk velocity, U_b, while it will decay to 5-15% of the bulk velocity, U_b, at small asymmetry ratios.
3. The lateral velocities increase with asymmetry ratio as the Coanda effect forces the jet to curve faster towards the wall.
4. Turbulence levels are highest near the jet half width, $y_{0.5}$ and $z_{0.5}$. Turbulence intensity w_{rms} and turbulent kinetic energy, k, increase with asymmetry ratio while levels of turbulence intensities u_{rms} and v_{rms} do not significantly change.
5. The Reynolds shear stresses uv and uw are dominant in the xy-plane and xz-plane respectively. Triple velocity correlation uvw increases with asymmetry ratio except at the maximum asymmetry ratio where it is reduced.

7.2 *Practical Relevance*

The results from this experimental study will be useful to a hydraulic engineer designing a new, or rehabilitating an old hydraulic structure. When designing these structures, an engineer will look to minimize the anthropogenic effects caused by the structure.

The Reynolds number should not be a major factor in the design of these structures. Industrial applications will typically operate at a high range of Reynolds number which has been observed to have no significant effect on three-dimensional offset jets.

The tailwater level can have a significant effect on the jet. In applications with changing tailwater the engineer must keep in mind that the jet may move to the water surface or the channel bottom depending on the tailwater level.

In order to reduce the streamwise velocity downstream, a hydraulic engineer should keep the discharge from a hydraulic structure away from the channel edge. This will prevent the jet from curving and reattaching to the wall which reduces its streamwise velocity decay.

7.3 *Recommendations*

The ADV has been around for two decades, however only a limited number of studies on jets have used this technique. The use of an ADV in this study allowed data collection at a high spatial and temporal resolution with good accuracy. The novel feature of the ADV to study jets is its ability to simultaneously collect all three components of velocity. The greater use of an ADV in future studies of jets would increase our knowledge on the correlation between all three velocities, the six components of Reynolds stresses, and the ten triple velocity correlation terms. These values are extremely useful in the calibration and validation of turbulence models however complete data sets are lacking in open literature.

Decay rates in this study varied from previous studies of three-dimensional offset jets. This was explained by various turbulence levels and orifice geometry between this and

previous studies. A study examining the effects of turbulence level and orifice geometry would help decisively explain the observed differences.

The reattachment length is a feature of an offset jet that was not measured in this study. It would be of interest to perform experiments on the effect of tailwater level and asymmetry on the reattachment length of three-dimensional offset jets. It would be interesting to compare the reattachment length of three-dimensional offset jets to that of two-dimensional offset jets. Using an ADV and the forward-flow fraction technique it would be possible to estimate the reattachment length. Although several points would need to be collected, only the streamwise velocity would be of importance to estimate the reattachment length. Since the streamwise velocity converges more quickly than the turbulence statistics it should be possible to collect these points with a reduced sampling time.

References

Abrahamsson, H., B. Johansson, and L. Lofdahl. *The turbulence field of a fully developed three-dimensional wall jet.* Internal Report, Goteberg: Chalmers University of Technology, 1997.

Agelin-Chaab, M., and M. F. Tachie. "Characteristics of Turbulent Three-Dimensional Offset Jets." *Journal of Fluids Engineering*, 2011b: 1-9.

Agelin-Chaab, M., and M. F. Tachie. "Characteristics of Turbulent Three-Dimensional Wall Jets." *Journal of Fluids Engineering*, 2011a: 1-12.

Ahlman, D., G. Brethouwer, and A. V. Johansson. "Direct numerical simulation of a plane turbulent wall-jet including scalar mixing." *Physics of Fluids*, 2007: 1-13.

Ashforth-Frost, S., and K Jambunathan. "Effect of Nozzle Geometry and Semi-Confinement on the Potential Core of a Turbulent Axisymmetric Free Jet." *International Communications in Heat and Mass Transfer*, 1996: 155-162.

Bhuiyan, F., A. Habibzadeh, N. Rajaratnam, and D. Z. Zhu. "Reattached Turbulent Submerged Offset Jets on Rough Beds with Shallow Tailwater." *Journal of Hydraulic Engineering* 137, no. 12 (2011): 1636-1648.

Blanckaert, K., and U. Lemmin. "Means of noise reduction in acoustic turbulence measurements." *Journal of Hydraulic Research* 44, no. 1 (2006): 3-17.

Bourque, C., and B. G. Newman. "Reattachment of a Two-Dimensional, Incompressible Jet to an Adjacent Flat Plate." *The Aeronautical Quarterly*, 1960: 201-232.

Craig, R. G.A., C. Loadman, B. Clement, P. J. Rusello, and E. Siegel. "Characterization and Testing of a new Bistatic Profiling Acoustic Doppler Velocimeter: The Vectrino-II." Monterat: Current, Waves and Turbulence Measurement Commitee of the IEEE/Oceanic Engineering Society, 2010.

Davis, M. R., and H. Winarto. "Jet diffusion from a circular nozzle above a solid plane." *Journal of Fluid Mechanics*, 1980: 201-221.

Dey, S., T. K. Nath, and S. K. Bose. "Fully rough submerged plane wall-jets." *Journal of Hydro-environment Research*, 2010: 301-316.

Dombroski, D. E., and J. P. Crimaldi. "The accuracy of acoustic Doppler velocimetry measurements in turbulent boundary layer flows over a smooth bed." *Limnology and Oceanigraphy: Methods* 5, no. 1 (2007): 23-33.

Durand, Z. M. J., S. P. Clark, M. F. Tachie, J. Malenchak, and G. Muluye. "Experimental Study of Reynolds Number Effects on Three-Dimensional Offset Jets." *4th Joint*

US-European Fluids Engineering Division Summer Meeting. Chicago: ASME, 2014. 1-12.

Ead, S. A., and N. Rajaratnam. "Plane Turbulent Surface Jets in Shallow Tailwater." *Journal of Fluids Engineering*, 2001: 121-127.

Ead, S. A., and N. Rajaratnam. "Plane Turbulent Wall Jets ion Rough Boundaries with Limited Tailwater." *Journal of Engineering Mechanics*, 2004: 1245-1250.

Eriksson, J. G., R. I. Karlsson, and J. Persson. "An experimental study of a two-dimensional plane turbulent wall jet." *Experiments in Fluids*, 1998: 50-60.

Gao, N., and D. Ewing. "Experimental investigation of planar offset attaching jets with small offset distances." *Experiments in Fluids*, 2007: 941-954.

Gao, N., and D. Ewing. "On the phase velocities of the motions in an offset attaching planar jet." *Journal of Turbulence*, 2008: 1-21.

Garcia, C. M., P. R. Jackson, and M. H. Garcia. "Confidence intervals in the determination of turbulence parameters." *Experiments in Fluids* 40, no. 4 (2006): 514-522.

Goring, D. G., and V. I. Nikora. "Despiking Acoustic Doppler Velocimeter Data." *Journal of Hydraulic Engineering*, 2002: 117-126.

Hall, J. W., and D. Ewing. "Three-Dimensional Turbulent Wall Jets Issuing from Moderate-Aspect-Ratio Rectangular Channels." *AIAA journal*, 2007: 1-10.

Hoch, J., and L. M. Jiji. "Two-Dimensional Turbulent Offset Jet-Boundary Interaction." *Journal of Fluids Engineering*, 1981: 154-161.

Hurther, D., and U. Lemmin. "A Correction Method for Turbulence Measurements with a 3D Acoustic Doppler Velocity Profiler." *Journal of Atmospheric and Oceanic Technology* 18 (2001): 446--458.

Islam, M. R., and D. Z. Zhu. "Kernel Density-Based Algorithm for Despiking ADV Data." *Journal of Hydraulic Engineering* 139, no. 7 (2013): 785-793.

Launder, B. E., and W. Rodi. "The Turbulent Wall Jet - Measurements and Modeling." *Annual Review of Fluid Mechanics*, 1983: 429-459.

Launder, B. E., and W. Rodi. "The Turbulent Wall Jet." *Progress in Aerospace Sciences*, 1981: 81-128.

Law, A., and Herlina. "An Experimental Study on Turbulent Circular Wall Jets." *Journal of Hydraulic Engineering*, 2002: 161-174.

Lohrmann, A. *Seeding in a wave/towing tank for a Vectrino - Nortek International.* 2009. http://www.nortekusa.com/en/knowledge-center/forum/velocimeters/38918768?b_start=0#375925759 (accessed 12 11, 2013).

—. *Seeding Material - Nortek International.* 2003. http://www.nortekusa.com/en/knowledge-center/forum/velocimeters/30181026?b_start=0#382730426 (accessed 12 11, 2013).

Lohrmann, A., R. Cabrera, N. C. Kraus, and M.ASCE. "Acoustic-Coppler Velocimeter (ADV) for Laboratory Use." *Fundamentals and Advancements in Hydraulic Measurements and Experimentation.* Buffalo, 1994. 351-365.

Nasr, A., and J. C. S. Lai. "A turbulent plane offset jet with small offset ratio." *Experiments in Fluids*, 1998: 47-57.

Nasr, A., and J. C. S. Lai. "Comparison of flow characteristics in the near field of two parallel plane jets and an offset plane jet." *Physics of Fluids*, 1997: 2919-2931.

Nortek AS. "Vectrino Profiler 3D Profiling Velocimeter." Norway, 2013.

Nortek. *Midas Data Acquisition Software.* Boston: Nortek, 2013.

Nortek. *Vectrino Profiler Profiling Velocimeter User Guide.* Boston: Nortek, 2012.

Nozaki, T., K. Hatta, M. Makashima, and H. Matsumura. "Reattachment Flow Issuing from a Finite Width Nozzle." *Bulleting of the Japan Society of Mechanical Engineers*, 1979: 340-347.

Nyantekyi-Kwakye, B., S. Clark, M. F. Tachie, J. Malenchak, and G. Muluye. "Flow Characteristics within the Recirculation Region of Three-dimensional Turbulent Offset Jet." *Journal of Hydraulic Research*, 2014 In Press.

Padmanabham, G., and L. B. H. Gowda. "Mean and Turbulence Characteristics of a Class of Three-Dimensional Wall Jets - Part 2: Turbulence Characteristics." *Journal of Fluids Engineering*, 1991b: 629-634.

Padmanabham, G., and L. B. H. Gowda. "Mean and Turbulence Characteristics of a Class of Three-Dimensional Wall Jets - Part1: Mean Flow Characteritics." *Journal of Fluids Engineering*, 1991a: 629-628.

Pelfrey, J. R. R., and J. A. Liburdy. "Effect of curvature on the turbulence of a two-dimensional jet." *Experiments in Fluids*, 1986b: 143-149.

Pelfrey, J. R. R., and J. A. Liburdy. "Mean Flow Characteristics of a Turbulent Offset Jet." *Journal of Fluids Engineering*, 1986a: 82-88.

Raffel, M., C. E. Willert, S. T. Wereley, and J. Kompenhans. *Particle Image Velocimetry A Practical Guide.* 2nd. Berlin: Springer, 1998.

Rajaratnam, N., and B. S. Pani. "Three-Dimensional Turbulent Wall Jets." *Journal of the Hydraulics Division*, 1974: 69-83.

Rajaratnam, N., and K. Subramanya. "Plane Turbulent Reattached Wall Jets." *Journal of the Hydraulics Divisions*, 1968: 95-112.

Rostamy, N., D. J. Bergstrom, D. Sumner, and J. D. Bugg. "An Experimental Study of a Turbulent Wall Jet on Smooth and Transitionally Rough Surfaces." *Journal of Fluids Engineering*, 2011: 1-8.

Rusello, P. J. *A Practical Primer for Pulse Coherent Instruments.* Nortek, 2009.

—. *Identifying weak spots in Vectrino Profiler data - Nortek International.* 2013. http://www.nortekusa.com/en/knowledge-center/forum/vectrinoii/500874976?b_start=0#774928256 (accessed 12 13, 2013).

Rusello, P. J., A. Lohrmann, E. Siegel, and T. Maddux. "Improvements in Acoustic Doppler Velocimetery." *the 7th international conference on Hydroscience and Engineering.* Philadelphia, 2006. 1-16.

SonTek. *Acoustic Doppler Velocimeter Principles of Operation.* San Diego: SonTek, 2001.

SonTek. *SonTek/YSI ADVField/Hydra Operation Manual.* San Diego: SonTek, 2001.

Sun, H., and D. Ewing. "Effect of Initial and Boundary Conditions on Development of Three-Dimensional Wall Jets." *American Institute of Aeronautics and Astronautics*, 2002: 1-11.

Swamy, N. V. C., and P. Bandyopadhyay. "Mean and turbulence characteristics of three-dimensional wall jets." *Journal of Fluid Mechanics*, 1975: 541-562.

Swamy, N. V. C., and P. Bandyopadhyay. "Structure of Three Dimensional Wall Jets." *Indian Journal of Technology*, 1981: 390-394.

Tachie, M. F., R. Balachandar, and D. J. Bergstrom. "Roughness effects on turbulent plane wall jets in an open channel." *Experiments in Fluids*, 2004: 281-292.

Venas, B., H. Abrahamsson, P.-A. Krogstad, and L. Lofdahl. "Pulsed hot-wire measurements in two- and three-dimensional wall jets." *Experiments in Fluids*, 1999: 210-218.

Voulgaris, G., and J. H. Trowbridge. "Evaluation of Acoustic Doppler Velocimeter (ADV) for Turbulence Measurements." *Journal of Atmospheric and Oceanic Technology* 15, no. 1 (1998): 272-289.

Wahl, T. L. "Analyzing ADV Data Using WinADV." *Joint Conference on Water Resources Engineering and Water Resources Planning and Management.* Minneapolis, 2000. 1-10.

Wang, X. K., and S. K. Tan. "Experimental investigation of the interaction between a plane wall jet and a parallel offset jet." *Exp Fluids*, 2007: 551-562.

Yoon, S. H., K. C. Kim, D. S. Kim, and M. K. Chung. "Comparative Study of a Turbulent Wall-Attaching Offset Jet and a Plane Wall Jet." *Korean Society of Mechanical Engineers Journal*, 1993: 101-112.

Zedel, L., and A. Hay. "Turbulence measurements in a jet: Comparing the Vectrino and VectrinoII." *IEEE?OES?CWTM Tenth Working Conference on Current Measurement Technology.* 2010.

APPENDIX A: Acoustic Doppler Velocimeter

A.1 Principles of Operation

The acoustic Doppler velocimeter (ADV) was developed to provide accurate three-dimensional flow measurements at a sub-centimeter spatial resolution and at a minimum time resolution of 25 Hz. The system was designed to be easily set up both in the laboratory and in the field and to require little maintenance (Lohrmann et al. 1994). Since its introduction in the 1990s several iterations of ADVs have been developed and show significant improvements.

The ADV used in this study is a Nortek Vectrino Profiler. Its probe, as seen in Figure A-1, is comprised of one central transmitter surrounded by four receivers equally spaced at 90° from each other. The four receivers are angled at 30° from the transmitter. To measure velocity, the ADV sends out sound pulses from the transmitter at a high frequency, f_p. The pulses reflect off particles within the sampling volume, referred to as the cell, and the reflection is recorded by the four receivers. The velocity of the particle is assumed to be identical to the water velocity. Using a technique called pulse-coherent

Figure A-1 ADV probe

processing the Doppler shift is converted into a velocity component of the particle in each of the four beam directions. The beam velocity is angled at the bi-static angle between the transmitter and receiver as represented by the arrow in Figure A-2. The pulse-coherent processing technique measures the phase difference between two consecutive pulses separated by a known change in time to calculate the Doppler shift. The ADV outputs a beam velocity time series for each receiver at a user selected sampling frequency, f_s. Each point in the time series is an average of several pulses sent at the high frequency, f_p. A matrix transform is then applied to the beam velocities to convert them into coordinate velocities in the *x*, *y*, and *z* direction. The four receiving transducers of the ADV are arranged in two perpendicular planes, one in the longitudinal and the second in the transverse direction. The two receivers in each plane measure a horizontal and vertical

Figure A-2 Beam velocity

component of velocity. The longitudinal plane measures the longitudinal and vertical velocities U and V_1, while the transverse plane measures the transverse velocity W and a redundant vertical velocity V_2. The redundant vertical velocity V_2 is important for noise removal in post-processing, which will be discussed in the noise removal section. The ADV is able to simultaneously undertake this process for up to 31 cells, thereby giving it the ability to measure profiles of up to 31 mm in height (Craig et al. 2010, Nortek 2012, Voulgaris and Trowbridge 1998).

The ADV has a selectable sampling frequency between 1 and 100 Hz giving a temporal resolution between 1 and 0.01 seconds. The cell height is also selectable and gives a spatial resolution between 1 to 4 mm (Nortek AS 2013). The smallest time scale the ADV can resolve is 0.01 seconds and the smallest length scale is 1 mm.

A.2 Data Quality

ADV manufacturers have implemented data quality indicators such as the correlation value, amplitude value, and signal to noise ratio value (SNR) that can be used to assess the quality of the recorded data (Wahl 2000, SonTek 2001). High quality data will ensure the characteristics of the flow are well represented. Nortek maintains an online forum that provides guidance on how to assess data quality and identify problems such as phase wrapping. This section describes the correlation, amplitude, and SNR values and explains how they are used to obtain reliable data. Phase wrapping is explained and the method used to identify it is described.

A.2.1 Correlation

The correlation value is a data quality indicator reported by the ADV. It is a normalized value between 0% and 100%. The correlation value indicates how well successive return echoes correlate with each other and the original pulse that was sent out. A high correlation value indicates that the ADV is recording the echo of the original sent pulse (P. J. Rusello 2009). A low correlation means the return echo does not correlate well with the sent pulse and contains additional noise, lowering the confidence level in the data (SonTek 2001). A correlation value is reported for each point within the time series of all four beams.

When ADVs were still a relatively new technology, a point with a correlation value of 70% or above was determined to measure good quality data and this value has remained as a rule of thumb (Rusello et al. 2006, Rusello 2009). With the advancement of ADV technology it is now typical of users to aim for a mean correlation value of the time series of 90% to ensure the majority of the data is relevant to the measured flow (Rusello et al. 2006). Points within a time series with a correlation value less than 70% can however still provide accurate data if the other quality indicators exceed their own requirement. These requirements will be explained in the following sections. The correlation value has been shown to reduce as turbulence increases. (Wahl 2000).

Wahl (2000) suggests removing without replacement all points within a time series that have a correlation below 70%, however, he notes this could be removing data of good quality. Islam and Zhu (2013) show that points below 70% correlation can still provide good data. Peter J. Rusello (personal communication, November 22, 2013), a Nortek employee, advises to remove points from a time series that are below a correlation of

40%. He also advises to remove whole time series and consequently a cell from further analysis if so many points are removed that the time series' statistics become unrepresentative of the flow. In order to calculate turbulence characteristics, a data series must be continuous and the removal without replacement of individual points within a time series is undesirable.

The following screening method was used based on the recommendations outlined above. For each beam of a cell, the data screening process evaluated the percentage of points within a time series that had a correlation below 40%. If any of the four beams had more than 10% of the points below 40% correlation, the cell was eliminated from further analysis. Individual points within a time series were not removed nor replaced from time series based on data quality indicators in this study.

A.2.2 SNR

The ADV reports the Signal to Noise Ratio (SNR) as a data quality indicator. The SNR value is reported in units of decibels as:

$$SNR = 20\log_{10}\left(\frac{Amplitude_{signal}}{Amplitude_{noise}}\right) \qquad \textbf{Equation A-1}$$

(Nortek 2012)

The $Amplitude_{signal}$ is a measure of the strength of the return echo for each point within a time series. The $Amplitude_{noise}$ is the noise strength, it is measured once at the beginning of every sample. The noise strength is close to the electronic noise level of the ADV (Lohrmann et al. 1994). An amplitude and SNR value are recorded for each point within the time series of all four beams.

A low SNR value indicates that the strength of the return signal is weak compared to the noise level. When the return signal is highly contaminated by noise the ADV is unable to accurately resolve the phase shift of the return pulse which leads to an unreliable velocity measurement. At a high SNR the return pulse is clear and not contaminated by noise. The ADV can then resolve the phase shift and provide an accurate velocity measurement.

The minimum SNR value to ensure data quality proposed by ADV manufacturers has varied from 5 dB to 15 dB and is dependent on the flow, sampling frequency, and objectives of the experiment (SonTek 2001, Rusello et al. 2006). Peter J. Rusello (personal communication, November 21, 2013) suggests a minimum SNR value in the range of 15 to 20 dB for measuring turbulence with the ADV used in this study because of its small sampling volume.

A similar screening method to correlation was used for SNR. Based on the recommendations outlined above, if an SNR time series had more than 10% of its points below 15 dB, the cell was eliminated from further analysis.

A.2.2.1 Seeding Material

The SNR is directly related to the amplitude of the return signal. A low amplitude return signal will typically be caused by a low amount of scattering particles in the water to reflect the sound pulses back to the receivers. ADV manufacturers suggest adding seeding material to the water to increase the amplitude of the return signal and the SNR (SonTek 2001, Lohrmann 2003) which will result in improved data quality. The suggested seeding particles from most ADV manufacturers are neutrally buoyant spherical glass beads of 10 μm diameter (SonTek 2001, Lohrmann 2003). The water in

this study was seeded with 10 μm glass beads to a concentration of 20 to 30 mg/L as recommended by the ADV manufacturer (A. Lohrmann 2009).

When adding seeding material as scattering particles it is important to verify that the particles will properly follow the flow without adding a significant bias to the measurements. Raffel et al. (1998) outline a procedure using the settling velocity and relaxation time to verify that the particles will follow the flow adequately.

The settling velocity, $V_{settling}$ [m/s], and relaxation time, τ_S [s], of the particle can be calculated from Equation A-2 and Equation A-3 shown below. In these equations, d_P [m] and ρ_P [kg/m^3] are the diameter and density of the particle, respectively, μ [Ns/m^2] and ρ [kg/m^3] are the dynamic viscosity and density of water, respectively, and g [m/s^2] is the acceleration due to gravity. If the settling velocity and relaxation time are small compared to typical velocity and time scale of the flow, the particles can be assumed to follow the flow adequately.

$$V_{settling} = d_P^2 \frac{(\rho_P - \rho)}{18\mu} g \qquad \textbf{Equation A-2}$$

$$\tau_S = d_P^2 \frac{\rho_P}{18\mu} \qquad \textbf{Equation A-3}$$

The glass beads used in this study have a settling velocity of 5.4×10^{-6} m/s and a relaxation time of 6.1×10^{-6} second. These values are significantly smaller than the smallest velocity and time scales of the flow, and will follow the flow adequately. The glass beads used in this study are an ideal seeding material.

The SNR can also be increased by enlarging the size of the sampling volume. This method will also increase the correlation. By increasing the size of the sampling volume

the reflected signal has higher amplitude as more particles are reflecting sound. This reduces the noise, which increases the SNR and correlation. This method will however decrease the spatial resolution. This method of increasing the SNR was not implemented in the current study because a high special resolution was desired. The high spatial resolution was maintained by using a cell size of 1 mm.

A.2.3 Weak Spots and Amplitude

A weak spot occurs in the velocity signal when a pulse passes through the sampling volume reflects off a boundary and passes through the sampling volume again at the same time as the next pulse. The ADV will measure the return signal of the initial pulse that is reflected from the boundary and the second pulse. Weak spots are a function of boundary distance and the speed of sound. Since these remain constant during sampling, weak spots will affect the entire time series (Nortek 2013). Cells affected by weak spots will not accurately represent the real flow velocity and should not be used.

The amplitude time series of a cell affected by a weak spot will be higher and relatively constant when compared to the amplitude time series of a cell that is not affected by a weak spot. This can be seen in Figure A-3. By comparing the distribution of the amplitude time series of the four beams within a cell it is possible to evaluate if the cell is affected by a weak spot. The amplitude distribution of the four beams within a cell should overlap, whereas a cell affected by a weak spot will not have overlapping distributions (Rusello 2013). This can be seen in Figure A-4. In this study cells were identified as being affected by a weak spot if they failed the criteria in Equation A-4. The constant C in Equation A-4 was manually calibrated. For $C = 1.5$ the criteria correctly identified all but one of 672 cells used in calibration for a success rate of 99.9%.

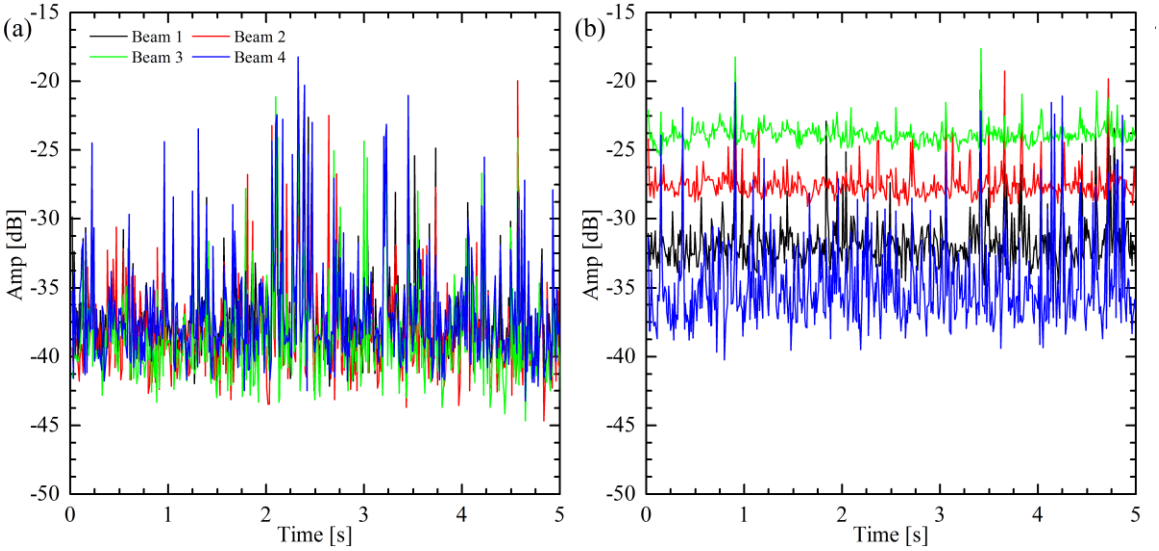

Figure A-3 Amplitude time series (a) not a weak spot (b) weak spot

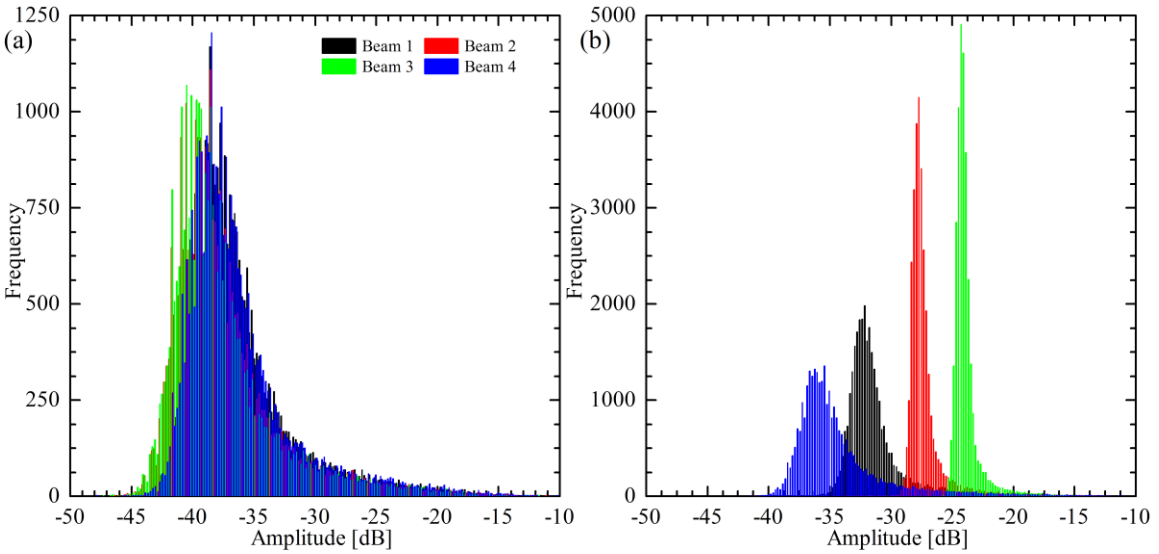

Figure A-4 Amplitude histogram (a) not a weak spot (b) weak spot

A.2.4 Velocity Range and Phase Wrapping

The velocity range is the most important parameter to set when operating the ADV. The velocity range directly impacts the frequency, f_p, at which sound pulses are emitted. The ADV measures the phase difference between two consecutive pulses separated by the known time interval to calculate the Doppler shift and convert it to a beam velocity. A smaller velocity range will have a larger time interval, while a larger velocity range will

have a smaller time interval. At the higher velocity range the reflected pulse is more likely to be contaminated by noise (Rusello et al. 2006). It is therefore desirable to set the velocity range at the lowest possible setting in order to minimize the noise.

The ADV will always measure a phase difference within ±180° regardless of the velocity range and time interval. If the velocity range is set too low and the phase difference exceeds the limit of 180°, the perceived difference will be in the range of -180° to 0°. For example, a phase shift of 185° will be calculated as -175°. Consequently, negative phase differences that are below -180° will be seen as a positive between 0° and 180°. This is referred to as phase wrapping or aliasing. Phase wrapping will cause a time series to jump from an extreme velocity near the velocity limit to an extreme value near the opposite velocity limit as seen in Figure A-5. This will skew the mean of the velocity time series towards the opposite limit, while also increasing the turbulence intensities as the jumps from opposite extremes will be large. For this reason phase wrapping is undesirable and should be avoided.

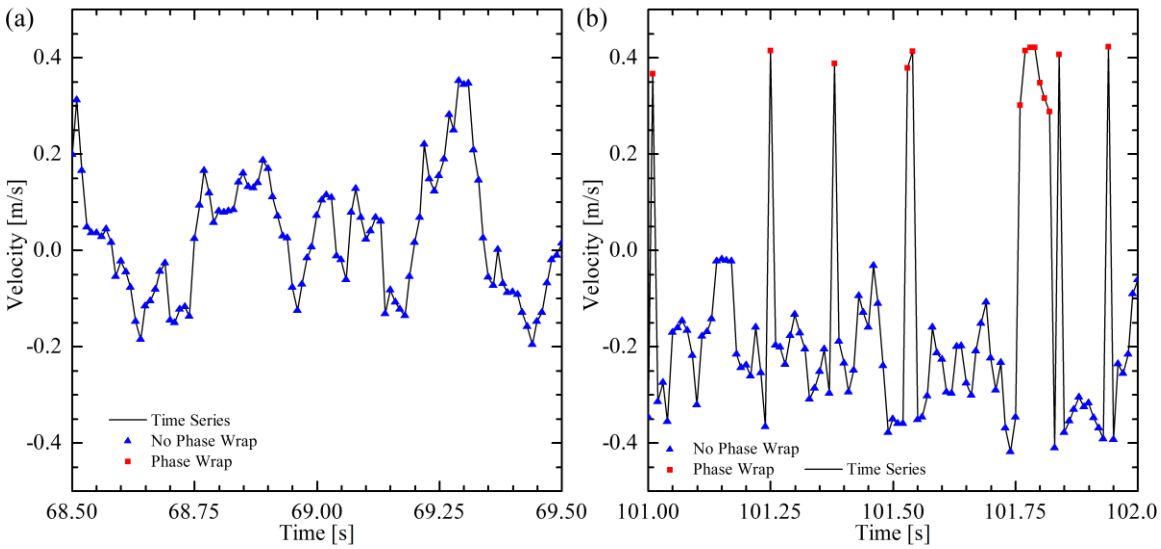

Figure A-5 Beam velocity time series (a) without phase wrapping and (b) with phase wrapping

A simple method to identify phase wrapping is by visual inspection of the histogram of the beam velocity time series. The histogram without phase wrapping follows a Gaussian distribution while that of a time series with phase wrapping will be cut near a velocity limit and the tail will continue from the other velocity limit. This can be seen in Figure A-6.

In this study the velocity range was set to the lowest possible velocity range in order to minimize the noise. The histograms of velocity time series were visually inspected to ensure no phase wrapping had occurred during measurements.

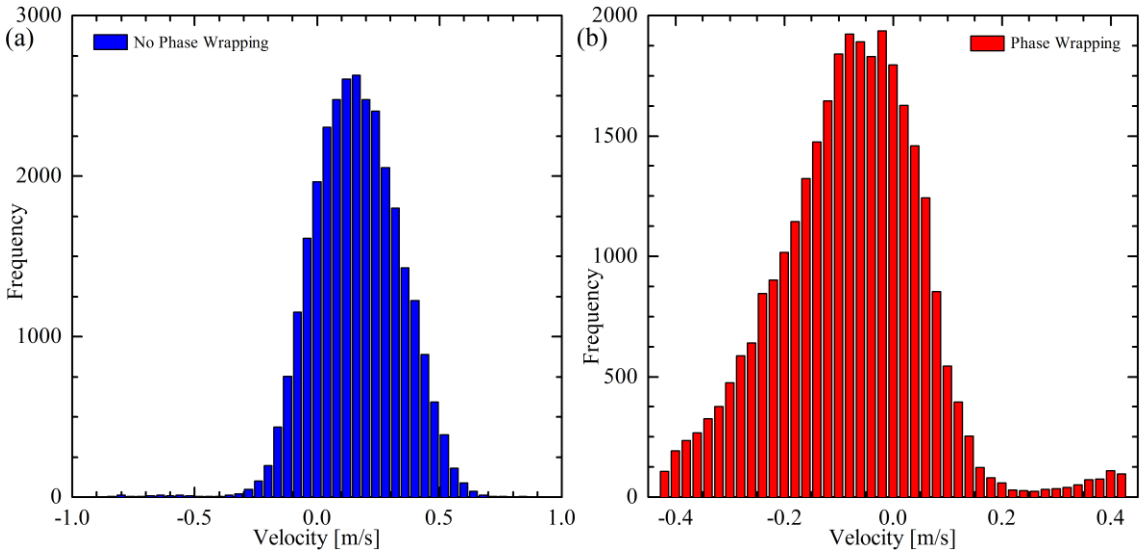

Figure A-6 Beam velocity histogram (a) without phase wrapping and (b) with phase wrapping

A.3 Despiking

Phase wrapping, random motion of seeding particle, air bubbles, and boundary interference can all introduce spikes in velocity time series. Velocity time series affected by spikes, or outlier points, have been shown to not follow the Kolmogorov universal -5/3 slope. For this reason despiking has become necessary in post-processing ADV data (Islam and Zhu 2013). Several despiking algorithms have been developed to

remove outliers from velocity time series. The acceleration threshold method and phase-space threshold method were proposed by Goring and Nikora (2002). Wahl modified the phase-space algorithm and implemented it into the software called WinADV (Islam and Zhu 2013). A kernel density-based algorithm to despike ADV data in turbulent jet flow was recently developed by Islam and Zhu (2013). The kernel-density based algorithm was developed as an iteration free method to despike time series with large amounts of spikes such as turbulent jets. This method uses a varying cutoff threshold that is dependent on the morphology of the data to identify spikes, instead of a constant cutoff threshold that led to inefficiencies in previous algorithms. In the kernel-density based algorithm the points that are identified as spikes are replaced by linear interpolation of the surrounding points. The kernel-density based algorithm developed performs well on time series highly contaminated by spikes compared to the previously listed algorithms (Islam and Zhu 2013). The kernel-density based algorithm was used in this study as it is a good algorithm to use in flows of high turbulence such as jets. The results from the kernel-density based algorithm can be seen in Figure A-7.

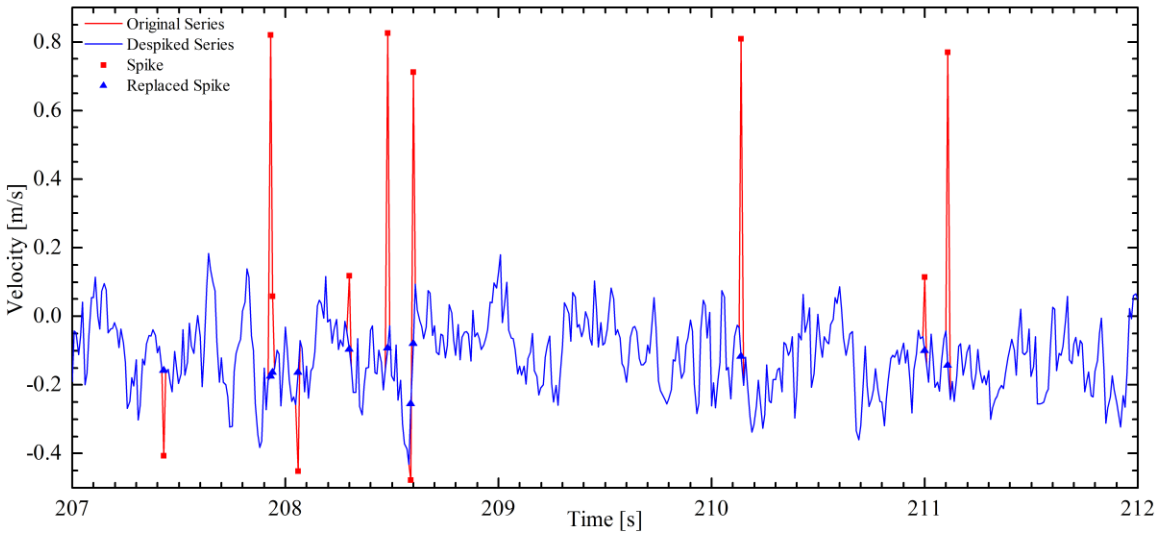

Figure A-7 Original and despiked time series

A.4 Noise Removal

ADV instruments are known to suffer from noise inherent to the measurement technique. The different sources of noise have been identified by several authors and are summarized by Hurther and Lemmin (2001). The noise has the following characteristics: It is white, is independent of the true Doppler frequency, is unbiased, has no effect on the mean velocity, and is statistically independent between the four beams (Blanckaert and Lemmin 2006). The mean velocity is not affected by the noise, neither are the Reynolds shear stresses and third moment turbulence statistics. The turbulence intensities and turbulent kinetic energy are affected by the noise (Hurther and Lemmin 2001). Hurther and Lemmin (2001) have outlined a method that takes advantage of the redundant vertical velocity to reduce the noise in the turbulence intensities and kinetic turbulent energy. It was later refined and simplified by Blanckaert and Lemmin (2006). The Reynolds normal stress from a single vertical velocity contains noise while the Reynolds normal stress calculated from the two redundant vertical velocity, V_1 and V_2, is noise free. The difference between these two Reynolds normal stresses is the vertical noise level (Blanckaert and Lemmin 2006). The horizontal noise is more than the vertical noise because of the geometrical configuration of the ADV. The horizontal noise is calculated by multiplying the vertical noise by a ratio based on the distance of the cell to the transmitter and the bistatic angle (Hurther and Lemmin 2001). This method was used to remove the noise from turbulence intensities, and turbulent kinetic energy.

A.5 Sampling Duration

The sample time, or length of the measured time series, must be of a duration that covers all significant fluctuations of the flow. This will ensure the flow and turbulence statistics

are independent of time, provide repeatable results and minimize error. The following convergence test has been conducted to select the duration of each sampled time series. A long time series of 30 minutes, for a sample size of 180,000 points, was collected in the flow conditions present during the study. Over the 30 minute time series, the statistics of the flow and turbulence such as mean velocity and turbulence intensities were assumed to have converged to their true value and be free of error. From the 30 minute time series, mean flow and turbulence statistics were calculated for series ranging from 15 seconds to 30 minutes in length at increments of 15 seconds. Subsequently, for each increment, percent errors based on the true values were computed. Figure A-8 shows the results of the convergence test. From the convergence test, a sample time of 5 minutes, for a sample size of 30,000, was required to reduce the impacts of fluctuations in the flow.

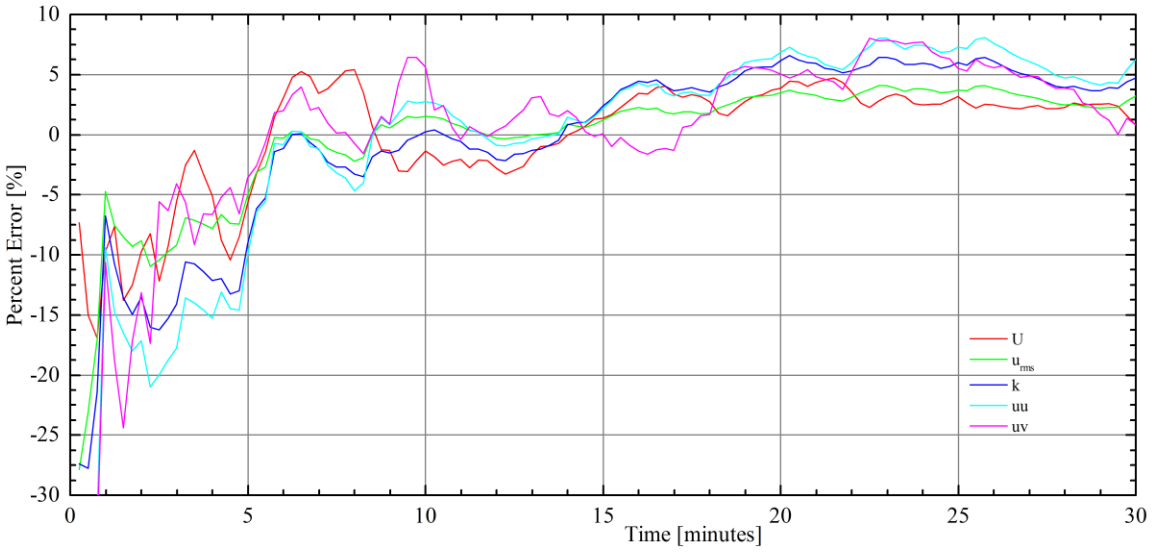

Figure A-8 Convergence test

A.6 Measurement Uncertainty

Identification of systematic and short term uncertainties must be identified to perform a complete uncertainty analysis of the ADV. Systematic uncertainties introduce a constant bias throughout all experiments. Physical constraints of the measurement device such as

sampling frequency and size of sampling volume are part of the systematic uncertainty. Positioning and alignment of the ADV also contribute to the systematic error (Garcia, Jackson and Garcia 2006). A misalignment of the ADV on the symmetry plane can affect the lateral velocity and symmetry results. The lateral mean velocity can be increased by 2% of the mean streamwise velocity if the ADV receivers are misaligned with the coordinate system by 1.2°.

Voulgaris and Trowbridge (1998), Dombroski and Crimaldi (2007), and Zedel and Hay (2010) compared the accuracy of laser Doppler velocimeters, hot-wire anemometers, and direct numerical simulations (DNS) to the accuracy of ADVs. In all studies, good agreement was found for mean flow measurement and Reynolds stresses between the ADV and the compared instruments and DNS. Higher noise was found in the horizontal velocities compared to the vertical velocity due to the geometry of the ADV.

The evaluation of short term uncertainty of turbulence parameters with traditional methods requires data to be uncorrelated or requires a large sample size to estimate the standard deviation of the population (Garcia, Jackson and Garcia 2006). The time series acquired in this study are correlated and only give one sample of each turbulence statistic. The moving block bootstrap technique commonly used in econometrics was validated by Garcia et al. (2006) to evaluate the confidence intervals of turbulence parameters of correlated time series. This method was used to evaluate the short term uncertainty of turbulence parameters.

A total uncertainty of ±3% of the local maximum streamwise velocity was evaluated for the streamwise and wall-normal velocities. The systematic uncertainty due to the position of the ADV increased the total uncertainty of the lateral velocity to ±5% of the local

maximum streamwise velocity. A total uncertainty of ±6%, ±5%, and ±15% of their respective local maximum was evaluated for turbulence intensities, turbulent kinetic energy, and Reynolds shear stresses, respectively.